Investigation on synthetic oxygenate fuels in future SI-engines using 0D/1D-simulation

Von der Fakultät Konstruktions-, Produktions- und Fahrzeugtechnik der Universität Stuttgart zur Erlangung der Würde eines Doktor-Ingenieurs (Dr.-Ing.) genehmigte Abhandlung

Vorgelegt von

Martin Cornelius Wagner
aus Unterschneidheim

Hauptberichter:	Prof. Dr.-Ing. M. Bargende
1. Mitberichter:	Prof. Dr. techn. C. Beidl
2. Mitberichter:	Prof. Dr. -Ing. A. Casal Kulzer
Tag der mündlichen Prüfung:	31.10.23

Institut für Fahrzeugtechnik der Universität Stuttgart
2023

„Always Know... (Monk)“
Thelonious Monk

Preface

This thesis was realized during my time as a research associate at the Institute of Automotive Engineering (IFS) at the University of Stuttgart under the supervision of Prof. Dr.-Ing. M. Bargende.

My deep gratitude goes to Prof. Dr.-Ing. M. Bargende for his guidance and support. I want to thank Prof. Dr. techn. C. Beidl and Prof. Dr. -Ing. A. Casal Kulzer for joining the doctoral committee and their interest in this work.

I would like to express my appreciation to my colleagues for their invaluable support and encouragement throughout this research project. My special thank goes to Dr.-Ing. Michael Grill for his professional support and guidance.

In addition, special thanks goes to the NAMOSYN project team for the always supportive cooperation and the good discussions.

Last but not least I would like to express my gratitude to my companion Sandra and my family for their unwavering support and encouragement during the completion of this thesis. Their assistance and belief in me have been invaluable throughout this challenging journey.

Dinkelscherben, den 19. November 2023 Martin Cornelius Wagner

Contents

Figures

Tables

Abbreviations

1D1D3D	0 dimensional, 1 dimensional, 3 dimensional
4CE	Series 4-cylinder engine
AFR	Air-fuel ratio
BDC	Bottom dead center
BEVs	Battery electric vehicles
BMBF	Federal ministry of education and research
BMEP	Brake mean effective pressure
BSFC	Brake specific fuel consumption
C65F35	Dimethyl carbonate 65 vol.% / Methyl formate 35 vol.%
CAD	Crank angle degree
CCV	Cycle to cylce variation
CFD	Computational fluid dynamics
CI	Compression-ignition
DAC	Direct air capture
DI	Direct injection

DMC	Dimethyl carbonate
DOC	Diesel oxidation catalyst
DPF	Diesel particulate filters
EGR	Exhaust gas recirculation
EO	Exhaust valve opens
FCell	Fuel cell
FKFS	Forschungsinstitut für Kraftfahrzeuge und Fahrzeugmotoren Stuttgart
FTDC	Firing top dead center
FVV	Research association for combustion engines eV
G100	Gasoline RON95 E5
G85F15	Gasoline RON95 E5 85 vol.% / Methyl formate 15 vol.%
HD	Heavy-duty
IC	Inlet valve closes
ICE	Internal combustion engine
IMEP	Indicated mean effective pressure
KSG	Bundes-Klimaschutzgesetz

LCA	Life-cycle assessment
LHV	Lower heating value
MeFo	Methyl formate
MFB	Mass fraction burned
MON	Motor octane number
NEVs	New energy verhicles
NHV	noise, vibration and harshness
OME	Polyoxymethylene dimethyl ethers
PC	Passenger car
PTA	Pressure trace analysis
PtL	Power to liquid
PtX	Power-to-X
RANS	Reynolds-averaged Navier-Stokes equations
RDE	Real drive emissions
REDII	Revised renewable energy directive II
RES	Renewable energy source
RFNBOs	renewable fuels of non-biological origin
RON	Research octane number
SCE	Single-cylinder research engine

SCR	Selective catalytic reduction
SI	Spark-Ignition
SOI	Start of injection
TKE	Turbulence kinetic energy
VGT	Variable geometry turbine
WLTP	Worldwide harmonized light vehicle test procedure
WPC	Working process calculation

Symbols

	Greek Letters	
α	Arrhenius exponent	k-
δ_L	Laminar flame thickness	m
ε	Compression ratio, Turbulence dissipation rate	-, $m^2 \cdot s^{-3}$
η	Engine efficiency	-
η_e	Engine brake efficiency	-
η_i	Indicated engine efficiency	-
γ	Heat capacity ratio	-
λ	Air-fuel equivalence ratio	-
ν	Kinematic viscosity	$m^2 \cdot s^{-1}$
ω	Angular speed of crankshaft	$rad \cdot s^{-1}$
ϕ	Fuel-air equivalence ratio, Crank angle	-
Π	Pi-criterion	-
ρ	Density	$kg \cdot m^{-3}$
τ_{ig}	Ignition delay time	s
τ_l	Characteristic burn-up time	s

	Indices	
b	backward	

b	burned
c	cylinder
F	Flame front
f	Fuel, forward
fl	Flame
ig	ignition
int	Integral
kn	knock model
ub	unburned
w	wall

Latin Letters

a	Frequency factor Arrhenius equation	-
A	Surface area	m^2
Ax	Axis	-
B	Bore	m
b	Temperature exponent	-
c_p	Specific heat capacity (isobar)	$J \cdot kg^{-1} \cdot K^{-1}$
c_v	Specific heat capacity (isochoric)	$J \cdot kg^{-1} \cdot K^{-1}$
Hu	Lower heating value	$J \cdot kg^{-1}$
P_i	Indicated Power	bar
U	Internal energy	J
V	Volume	m^3
$dQ_b/d\phi$	Heat release rate	$J \cdot deg^{-1}$
p_i	Indicated mean effective pressure	bar

p_c	Cylinder pressure	bar
E_A	Activation energy	$\mathrm{J \cdot mol^{-1}}$
I_{ig}	Livengood-Wu integral	kg m_2
I	Mass moment of inertia	$\mathrm{kg \cdot m^2}$
k	Reaction rate constant	-
L	Angular momentum	$\mathrm{kg \cdot m^2 \cdot s^{-1}}$
l_{int}	Integral length scale	m
m	Mass	kg
$\dot{m}$	Mass flow rate	$\mathrm{kg \cdot s^{-1}}$
n	Revolutions per minute	$\mathrm{min^{-1}}$
R	Universal gas constant	$\mathrm{J \cdot K^{-1} \cdot mol^{-1}}$
s_L	Laminar flame speed	$\mathrm{m \cdot s^{-1}}$
Tu	Tumble	-
T	Temperatur	K
u_E	Entrainment velocity	$\mathrm{m \cdot s^{-1}}$
$\overline{u}$	Turbulent mean velocity	$\mathrm{m \cdot s^{-1}}$
u'	Turbulent fluctuation velocity	$\mathrm{m \cdot s^{-1}}$

Kurzfassung

Die globalen Auswirkungen des Klimawandels stellen die Gesellschaft und Wirtschaft vor enorme Herausforderungen. Es ist seit langem erwiesen, dass der Mensch einen großen Beitrag zum Temperaturanstieg leistet [20]. Folgerichtig sind es die Menschen, die versuchen, diesen Trend zu stoppen. Wissenschaftler:innen und Ingenieur:innen suchen nach Lösungen für nachhaltige Technologien mit geringem Kohlenstoffdioxid-Fußabdruck. Insbesondere der Mobilitätssektor hat einen erheblichen Anteil an der vom Menschen verursachten CO_2Produktion. In Deutschland beispielsweise entfallen auf den Mobilitätssektor rund 20 % der gesamten CO_2Emissionen [21]. Daher ist es sinnvoll, Antriebskonzepte zu entwickeln, die zur Reduzierung von Kohlendioxid beitragen können. In [22] wird davon ausgegangen, dass im Jahr 2050 der vorherrschende Kraftstoffmix für PKWs weltweit durch Kohlenwasserstoffe angetrieben wird. Es ist somit zwingend notwendig, den konventionellen Antriebsstrang weiterzuentwickeln und effizienter zu gestalten.

Auf dem Weg zur emissionsfreien Mobilität müssen Kraftstoffe der Zukunft CO_2neutral sein. Um dies zu erreichen, werden synthetische Kraftstoffe auf Basis von erneuerabren Energien produziert. Um die Auswirkungen der neuen Kraftstoffe auf den Motorprozess besser beurteilen zu können, werden Simulationsmodelle entwickelt, die chemische und physikalische Eigenschaften dieser Kraftstoffe nachbilden können.

In dieser Arbeit werden der Kraftstoff C65F35 und ein Benzin-Mischkraftstoff G85F15 untersucht. C65F35 (ein Gemisch aus 65 % Dimethylcarbonat und 35 % Methylformiat, das sich hauptsächlich durch das Fehlen von C-C-Bindungen und einen hohen Sauerstoffgehalt auszeichnet) bietet Vorteile hinsichtlich hoher Verdampfungsenthalpie und damit einhergehendem Kühleffekt, geringerem Sauerstoffbedarf und hoher Klopffestigkeit. Außerdem ist die Verbrennung nahezu partikelfrei. G85F15 (ein Gemisch aus 85 % Benzin und 15 % MeFo) bietet aufgrund seines MeFo-Gehalts Vorteile beim Klopfverhalten.

Mit Hilfe moderner 0D/1D-Simulationsmethoden kann eine Bewertung des Potenzials der Kraftstoffe im Motorprozess vorgenommen werden.

Für die Kraftstoffe wurden Modelle angepasst (Ladungsbewegungs-, Turbulenz-, Zyklenschwankungs- , Brennverlaufs-, Klopf- und Emissionsmodell) und vorhandenen Prüfstandsmessungen gegenübergestellt.

Für das Ladungsbewegungs- und das Turbulenzmodell ist es wichtig, aufgrund des unterschiedlichen Heizwerts der Kraftstoffe, den Einfluss der Einspritzmasse zu berücksichtigen. Bei Motoren mit seitlicher Injektorlage konnte gezeigt werden, dass das Tumbleverhalten durch die Einspritzung geändert wird. Da der Tumble im Laufe der Kolbenbewegung in Turbulenz umgewandelt wird, spielt die Einspritzstrategie für den späteren Verbrennungsprozess eine entscheidende Rolle. Dies wird in den implementierten Modellen berücksichtigt und kann nach Kalibrierung mit CFD-Simulationen nachgebildet werden und somit eine belastbare Aussage über das Turbulenzniveau bei Verbrennung geben.
Die reaktionskinetischen Einflüsse der Kraftstoffe ist für die verwendete Brennverlaufsmodellierung zu berücksichtigen. Dieses Verhalten wurde mit der Kalibrierung anhand von Reaktionskinetiksimulationen in die Modelle integriert. Damit kann der Einfluss des Kraftstoffs auf die Verbrennung abgeleitet werden. In Kombination mit dem Einfluss auf die Ladungsbewegung können somit die gemessenen Brennverläufe der Prüfstände mit den Simulationsmethoden abgebildet werden. Dies schließt das Verhalten bei Last-, Drehzahl- und Lambdaänderungen ein.

Für die Auslegung virtueller Motorkonzepte wird eine zuverlässige Prognose des Klopfverhaltens benötigt. Simulativ kann dieses Verhalten über die Modellierung des Selbstzündverhaltens und weiter mit Hilfe von Klopfvorhersagen abgebildet werden. Da es sich bei C65F35 um einen extrem klopffesten Kraftstoff handelt steht keine breite Datenbasis an Klopfmessungen zur Verfügung. Am Prüfstand konnte gezeigt werden, dass mit Erhöhung der Ansaugtemperatur der Motor an die Klopfgrenze gebracht werden kann. Diese Messungen konnten für die Kalibrierung und Validierung des Selbstzündmodells verwendet werden. Außerdem kann damit das Klopfmodell dahingehen abgestimmt werden, dass eine weitere Erhöhung der Ansaugtemperatur oder des Ansaugdrucks durch die Klopfregelung zu einer Verlagerung des Verbrennungsschwerpunkts Richtung spät führt.

Das hohe Potenzial hinsichtlich geringer NOx Emissionsbildung der synthetischen Kraftstoffe wurde am Prüfstand beobachtet. Für die spätere Beurteilung der NOx Emissionen konnten die Modelle zur Vorhersage dieses Verhaltens an Reaktionskinetiksimulationen kalibriert und anhand von Prüfstandsdaten validiert werden. Dies stellt einen weiteren wichtigen Schritt zur Motorkonzeptauslegung dar.

Die Kalibrierung und Validierung aller erwähnten Modelle ist detaillierter in der Abhandlung beschrieben. Die Modelle reproduzieren dabei das Prüfstandsverhalten mit hoher Qualität.

Bei der Untersuchung der Motorkonzepte mit dem synthetischen Kraftstoff C65F35 können drei wesentliche Erkenntnisse festgestellt werden.

1. Die Klopfeigenschaften des Kraftstoffs führen nicht mehr zwingend zur Limitierung der Motorkonzepte

2. Bei steigendem Verdichtungsverhältnis kommt der Brennraumgeometrie entscheidende Bedeutung für den Brennverlauf zu. Dies ist auf den Einfluss auf die Ladungsbewegung und Flammenausbreitung zurückzuführen

3. Durch die im Vergleich zu Benzin langsamere laminare Flammengeschwindigkeit und geringere Prozesstemperaturen ist vor allem im Bereichen geringerer Lasten die Brenndauer länger

Der Benzin-Blend Kraftsoff wird trotz geringem MeFo Anteil (15 %) deutlich klopffester. Reaktionskinetiksimulationen zeigen, dass sich die Zündverzugszeiten nicht deutlich von konventionellem Benzinkraftstoff unterscheiden. Durch die höhere Einspritzmasse des Blendkraftstoffs ergibt sich jedoch ein Kühleffekt der zu diesem Verhalten führt.

Die Motorkonzepte werden mittels 0D/1D Simulation hinsichtlich Effizienz und Emissionen im Kennfeld sowie im RDE (Real Drive Emissions) bewertet. Dadurch kann eine Einschätzung des Verhaltens der synthetischen Kraftstoffe gegeben werden. Für PKW-Anwendungen wurden drei unterschiedliche Motorkonzepte untersucht: Eine Basisvariante, in der ein Wechsel des Kraftstoffs durchgeführt wird, eine kosteneffiziente Variante sowie Hocheffizienzvarianten, die die spezifischen Vorteile der untersuchten Kraftstoffe ausnutzen. Für

schwere Nutzfahrzeuge wurden Motorkonzepte für den Kraftstoff C65F35 entwickelt und mit konventionellen Konzepten verglichen. Des Weiteren wird ein Ausblick über ein mögliches Wasserstoffmotorenkonzept gegeben.

Anhand eines State of the Art Motors können die unterschiedlichen Kraftstoffe im Motorkennfeld beurteilt werden. Hierbei zeigt sich, dass sich im oberen Lastbereich deutliche Vorteile von C65F35 und G85F15 im Vergleich zu G100 (100 % Benzin) für den Wirkungsgrad ergeben. Dies liegt an der höheren Klopffestigkeit. Im unteren Teillastbereich ist dieser Vorteil nicht relevant. Hier zeigt G100 einen höheren Wirkungsgrad. Auf der einen Seite aufgrund der höheren laminaren Flammengeschwindigkeit, auf der anderen Seite muss aufgrund des höheren Gemischheizwerts des Blendkraftstoff und noch höheren Gemischheizwerts für C65F35 der Motor deutlich strärker angedrosselt werden. Dies lässt bereits auf ein hohes Potenzial für Downsizing schließen. Die Beurteilung im virtuellen RDE (Real Drive Emissions) fällt für G100 deshalb am günstigsten für den Basismotor aus.

Für die Auslegung von kosteneffizienten Motorkonzepten führt das Downsizingpotenzial bereits zu großen Vorteilen für C65F35 gegenüber G100. Durch eine Hubraumverkleinerung kann gezeigt werden, dass der Wirkungsgrad für das Konzept bei geringerer Komplexität der VKM um 1 Punkt im Realfahrzyklus ansteigen kann. Die Komplexität bezieht sich auf Bauteile, die zur Wirkungsgradsteigerung der Basisvariante verwendet werden (Variabler Ventiltrieb, Zylinderabschaltung). Der Blendkraftstoff kann bei geringerer Komplexität und Größe das Wirkungsgradniveau des Ausgangsmotors halten.

Für den reinen synthetischen Kraftstoff C65F35 sind für Hocheffizienzkonzepte Steigerungen von bis zu 10 % verglichen mit konventionellem State of the Art Benzinmotor im RDE möglich. Hier handelt es sich um ein Magermotorkonzept, dass mit Hilfe gängiger Abgasnachbehandlungssysteme (SCR und LNT) in der Abgasnorm gehalten werden kann. Dies ist mit deutlich geringer ausfallender Abmagerung des Gemischs im Vergleich zu G100 möglich, was sich auch am Prüfstand zeigt. Vorteilhaft ist dies für die Turboaufladung, wodurch deutlich geringere Massenströme bewältigt werden müssen.

Mit Maßnahmen zur Steigerung der Turbulenz bei Verbrennung (Aktive Vorkammerzündung, Hochturbulenzkonzepten) kann die Wirkungsgradsteigerung sogar bis zu 16 % betragen. Auch der Benzinblendmotor kann im Fahrzyklus

eine Wirkungsgradsteigerung von 4 % vorweisen, allerding bei deutlich höheren NO Emissionen.

Des weiteren wird Bewertung des synthetischen Ottokraftstoffs für schwere Nutzfahrzeuge durchgeführt. Auf Basis eines abgestimmten CNG-Motors kann das Brennverfahren auf C65F35 umgestellt werden. Bei gleichbleibendem Turbulenzniveau können bereits Wirkungsgradvorteile im Vergleich zu CNG erreicht werden. Dieser beträgt beim C65F35 Downsizingkonzept einen Vorteil von 6 % im virtuellen Realfahrzyklus. Dies ist zum einen auf das bessere Klopfverhalten und zum anderen auf das nachteilige gemischansaugende Brennverfahren bei CNG zurückzuführen. Im Quervergleich mit konventionellem Dieselkraftstoff wird das große Potenzial für die Ottokraftstoffe deutlich. C65F35 zeigt ähnliche Wirkungsgrade wie ein konventioneller Diesel-Antrieb. Da es sich hierbei um ein stöchiometrisches Konzept handelt ist darüber hinaus weiteres hohes Potenzial im Brennverfahren zu sehen. Der große Vorteil für das C65F35 Konzept ist die deutlich einfachere Abgasnachbehandlung, da ein konventioneller 3-Wege Katalysator verwendet werden kann. Zudem wird aufgrund des stöchiometrischen Betriebs der Turbolader deutlich weniger beansprucht, wodurch von zweifacher Aufladung auf ein einfaches Aufladesystem umgestellt werden kann. Hierdurch können zusätzliche Komponenten eingespart werden.

Außerhalb des Verbrennungsprozesses gibt es jedoch noch Probleme mit den in Frage kommenden Kraftstoffen, die technisch gelöst werden müssen. MeFo z.B. neigt dazu, sich in Gegenwart von Wasser zu Ameisensäure zu zersetzen. Dies kann verhindert werden, wenn der Brennstoff entsprechend additiviert wird. In diesem Bereich ist jedoch weitere Forschungsarbeit erforderlich. Es hat sich ebenfalls gezeigt, dass einige der im Verbrennungsmotor verwendeten Kunststoffe mit DMC und MeFo unverträglich sind. Diese Bauteile müssen gezielt ersetzt werden.

Die gewonnenen Erkenntnisse ermöglichen eine fundierte Bewertung von synthetischen Kraftstoffen im Motorbetrieb. Dies kann eine Orientierungshilfe für politische Entscheidungen sein, die auf systemischen Analysen der Umweltauswirkungen und der Energiebilanz über den gesamten Lebenszyklus von Antriebskonzepten basieren.

Abschließend sei auf das Potenzial hingewiesen, das weiterhin im Verbrennungsmotor steckt, insbesondere im Hinblick auf alternative Kraftstoffe. Wird die Entwicklung in diesem Bereich stark zurückgefahren, sind dies schlechte Voraussetzungen für eine zukünftige CO_2 neutrale Gesellschaft. Die Ergebnisse ermutigen dazu, die Forschungs- und Entwicklungsarbeiten zu synthetischen Kraftstoffen weiter zu verfolgen, die zu einem schnellen und kostengünstigen Weg in eine zukünftig nachhaltige Mobilität führen können.

Abstract

On the way to emission-free mobility, future fuels must be CO_2 neutral. To achieve this, synthetic fuels based on renewable energies are being developed. In order to better assess the effects of the new fuels on the engine process, simulation models are being developed that reproduce the chemical and physical properties of these fuels.

In this thesis, the fuel C65F35 and a gasoline blend fuel G85F15 are examined. C65F35 (a mixture of 65 % Dimethylcarbonat and 35 % Methylformate mainly, characterized by the lack of C-C Bonds and high oxygen content) offers advantages with regard to large evaporation heat and simultaneous cooling effect, less demand of oxygen and high knock resistance. Furthermore, its combustion is almost particle free. G85F15 (a mixture of 85 % Gasoline and 15 % MeFo) offers advantages in knock behaviour due to its MeFo content. With the aid of modern 0D/1D-Simulation methods, an assessment of the potential of these fuels can be made.

In the first step, a series of models for charge motion, turbulence, combustion, knock and emission are validated against measurement data. Secondly, the evaluation of the fuels are carried out based on the engines characteristic map and in the virtual real driving cycle for cost efficient and high efficiency concepts. The concepts are compared with a state of the art gasoline engine. This allows the full potential of the assessed fuels . It is shown that the simulative conversion of a state-of-the-art gasoline engine to C65F35 fuel offers advantages in terms of efficiency in a lot of operating points even if the engine design is not altered. This is mainly due to the higher knock resistance and the lower temperatures in the intake stroke resulting from the higher amount of evaporated fuel. It is also found that benefits up to 16 % of efficiency in the RDE (Real Drive Emissions) can be shown due to the use of synthetic fuels.

In a further step, the suitability of C65F35 in heavy duty applications is demonstrated. It can be shown that the fuel is also suitable for this field and

comes close to the efficiency of CI-Engine concepts with significantly less complexity of the engine, making C65F35 a highly promising prospective for future SI engines.

1 Introduction

The global effects of climate change are creating enormous challenges for both society and economy. It has long been proven that humans contribute highly to rising temperatures [20]. Naturally, it is the people who are trying to stop this trend. Scientists and engineers search for solutions for sustainable technologies with low carbon footprints. Especially the mobility sector has a significant share of human-made CO_2 production. In Germany, for example, the mobility sector accounts for around 20 % of total CO_2 emissions [21]. It therefore makes sense to develop propulsion concepts that can contribute to the reduction of carbon dioxide. In [22], it is assumed that, in 2050, the dominant fuel mix for passenger cars worldwide will be powered by hydrocarbons. Therefore, it is imperative to further develop the conventional powertrain and make it more efficient.

A solution approach of the aforementioned problem lies in the defossilization of the mobility sector. The use of so-called e-fuels can help operate the internal combustion engine in an almost CO_2 neutral manner, provided that the fuel is produced with renewable energy. Due to the technical progress, it is possible to synthesize different types of fuels. The properties of these fuels have a strong influence on the Internal combustion engine (ICE), which raises the question of the optimum fuel. Due to the ICEs complexity and its interaction with the fuel being used, this answer is not a simply one. Instead, extensive studies on different fuels need to be conducted in order to develop an overall understanding of this interaction.

Much of today's research on e-fuels focuses on replacing fossil fuels with synthetic fuels with similar properties. Life-cycle assessment (LCA) - which can be used to evaluate the energy efficiency of propulsion systems - focuses on the energy efficiency of the fuel production process with no benefits for the engine. However, if tailor-made fuels are developed for the ICE, this can result in clear operational advantages over conventional fuels.
As conventional fuel has some disadvantages regarding Spark-Ignition (SI) En-

gines, there is a vast efficiency potential in creating dedicated fuels for the propulsion system.

1.1 Objectives

The present work focuses on the fuel C65F35, a mixture of 65 % Dimethyl carbonate (DMC) and 35 % Methyl formate (MeFo). It is dedicated to investigating the behavior of C65F35 in an SI-Engine. The target is not only to focus on engine concepts but also to elaborate on the performance in the virtual real driving cycle. The possibility to quantify the influence of the fuel used on a tank-to-wheel based efficiency analysis is offered.

Simulation models are to be verified and extended concerning fuel properties to make statements regarding the suitability of these fuels in the combustion engine. With the aid of so-called phenomenological models, the interaction of fuels and engines is reproduced in a simulative environment. These models are based on physical approaches and can thus provide conclusions about specific fuel properties. It is expected that by choosing an appropriate fuel, the efficiency and emission reduction potential of the engine can be significantly increased without having to involve complex technologies. This also raises the question of which combustion process is the most suitable for efficiency-sensitive applications. Reliable analyses for e-fuels are only made possible after answering these questions.

In a further step, a gasoline blend fuel G85F15 (85 % Gasoline and 15 % MeFo) will be investigated for the use in passenger cars, and this work will also analyze its efficiency potential. Furthermore, an engine concept comparison for the fuels C65F35, methane, diesel and hydrogen will be carried out for a heavy duty application.
The potential of using suitable e-fuels will be quantified in this work, thus closing a gap in terms of LCA. A direct comparison with other synthetic fuels is therefore possible. In the context of this work, the oxygenate fuel methanol is not considered, as several studies have already been carried out on this subject (see [3, 4, 51]).

1.2 Procedure

A valuable method to perform this comprehensive analysis is the 0D/1D simulation. The models and their development provide a better understanding of the phenomena taking place in the combustion chamber. In consideration of synthetic fuels, the overall combustion engine system with conventional fuels is expanded and more profoundly understandable. In addition, these models can be used in operating ranges that would be extremely difficult to realize with the aid of a test bench or other measurement methods. Virtual test carriers can be adapted quickly and are ideal for evaluating the overall system of combustion engines and vehicles even at early stages of development. With model-based engine concept design, it is possible to assess which concepts are promising in the early development process. In this way, costs and development capacities can be used as needed.

The thesis is subdivided into the following parts: **Chapter 2** provides an overview of technologies for increasing the efficiency of the ICE. Furthermore, the required tools and data sources for the examination are discussed. In **Chapter 3** an overview of the models used is given. This work will discuss the fuel-induced adaptation of the models. With the help of the adjusted models (charge motion, turbulence, combustion process, knock, and emission model), the calculations are compared with test bench measurements and 3D-CFD data. Thereafter, the first investigations caused by the model's adjustment are presented. **Chapter 4** discusses the virtual test carriers for passenger cars. The thesis will offer a state-of-the-art engine with gasoline, adapted to the fuels C65F35 and G85F15. This is followed by engine concepts that correspond to a cost-optimized concept and, afterwards, are designed for maximum efficiency. The concepts are then examined in the virtual Real drive emissions (RDE), where, subsequently, the validity of the results is discussed. **Chapter 5** is addressed to engine concepts in the heavy-duty sector. Engine concepts using methane, diesel, hydrogen, and C65F35 are investigated. Again, the concepts are examined in the virtual real drive, followed by a discussion of the results.

1.3 E-Fuels

The base of all e-fuels is electric energy. As a first step, hydrogen must be produced. Carbon in the form of CO or CO_2 is added to the hydrogen molecules.

The fuels produced in this step form the basis e-fuels for further development stages. This process can be repeated until the desired product is obtained. If these fuels are produced with renewable energies and the CO_2 is captured from the air, their use in the ICE is climate-neutral. The energy required is mainly for hydrolysis, carbon-containing molecule production (unless present as a waste product), and the chemical process costs. It becomes clear that the presence of CO_2 is explicitly needed for e-fuels, turning the molecule into a valuable resource. To ensure climate neutrality, the idea is to create a closed carbon cycle which means that only as much CO_2 is produced during utilization as was previously bound for fuel production. The decarbonization often mentioned in public discourse does not apply to e-fuels since carbon is an important component in the aforementioned process. Defossilization applies better for the production with renewable energies. It should be mentioned that ammonia, for example, also counts as an e-fuel, which is in fact free of carbon.

Figure 1.1 shows different products of the Power-to-X (PtX) process and its application [1]. With each refining step, production costs increase while production efficiency decreases. Due to this disadvantage, good reasons are needed to use specific products that are higher ranked in the pyramid. This work deals with the e-fuels named Dimethyl carbonate (DMC) and Methyl formate (MeFo) which can be assigned to the functional e-fuels group and are oxygenates.

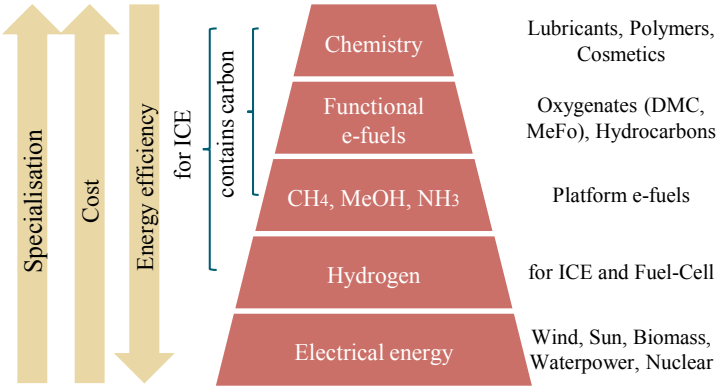

Abbildung 1.1: E-Fuel Pyramid [1]

The public discourse on e-fuels is often based on the poor efficiency of their production and their efficiency in relation to electromobility (fuel cell or battery based). Figure 1.2 shows a comparison between three propulsion technologies which include Battery electric vehicles (BEVs), fuel cells, and ICE vehicles. The starting point is the electrical energy provided. Different types of losses occur for the individual systems, which leads to a system efficiency of 69 % for the BEV. The fuel cell performs significantly worse with 26 %, followed by the ICE with 13 % overall efficiency. Despite these advantages of BEVs, which seem enormous at first glance, there is no geopolitical shift towards individual technologies. This work will discuss the reasons for this.

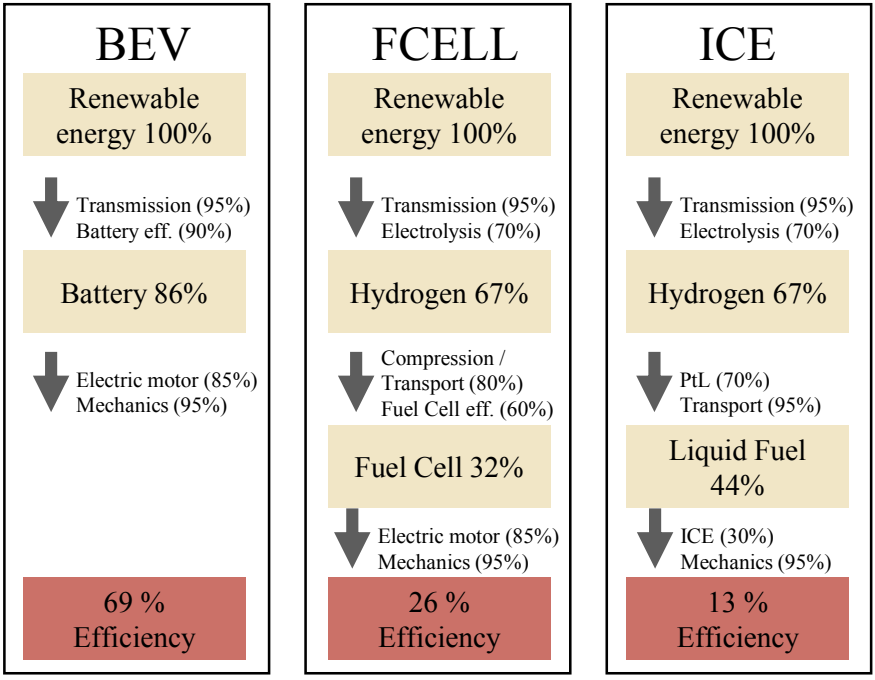

Abbildung 1.2: Efficiency of different propulsion systems [2]

Current status in Germany and the European Union

In 2019, Germany enacted a legislation called Bundes-Klimaschutzgesetz (KSG) to reduce CO_2 emissions by 65 % until the year 2030 compared to 1990. The seriousness of the so-called climate crisis was confirmed by the Bundesverfassungsgericht, which called for a redefinition of the CO_2 minimization strategy after 2030. Until the Corona crisis, the trend of imported primary energy in Germany steadily increased up to 67.9 % in 2019 [23], which leads to a conflict of objectives. Hence, the efficient use of this energy is of utmost importance.

In figure 1.3 the CO_2 equivalent for a synthetic fuel compared to the fossil one is shown. The efficiency of the synthesis process is stated to be approx. 44 % according to [2]. With 500 grams of CO_2 equivalent for the production of one kWh of electricity, synthetic fuels would emit four times as much CO_2 as fossil gasoline (dashed line), whereas renewable energies such as wind power can significantly reduce the CO_2 emissions of e-fuel production. The current electricity mix in Germany would produce about 2.6 times the CO_2 equivalent when used for e-fuels production. The german governments' ambitious targets results in a value of approx. 154 g CO_2 eg./kWh [24] based on similar energy consumption. Therfore can be concluded that the production of e-fuels in germany will play a minor role. Nevertheless, the storage of surplus renewable energy in form of e-fuels is an application that makes the production interesting in Germany, too.

The situation in France, for example, is different, where CO_2 emissions are lower due to the high amount of nuclear power, which means that 60 % less CO_2 would be produced during production of e-fuels compared to fossile gasoline. However, this means that the electricity used would no longer be available for other applications, which would lead to the need to build new nuclear power plants. The decisive influence of the energy mix on the perspectives of these fuels becomes obvious through this.

The European Green Deal aims to reduce CO_2 emissions by 50-55 % by 2030 and entirely by 2050 compared to 1990 [25]. In the transport sector, in 2018, the Revised renewable energy directive II (REDII) entered into force. This directive requires fuel suppliers to contribute at least 14 % of the energy consumed in transportation in 2030 to be renewable. In addition, to qualify for regulatory credit, renewable fuels of non-biological origin (RFNBOs), collo-

quially known as e-fuels, must save greenhouse gas by at least 70 %. This limit is also marked in the diagram.

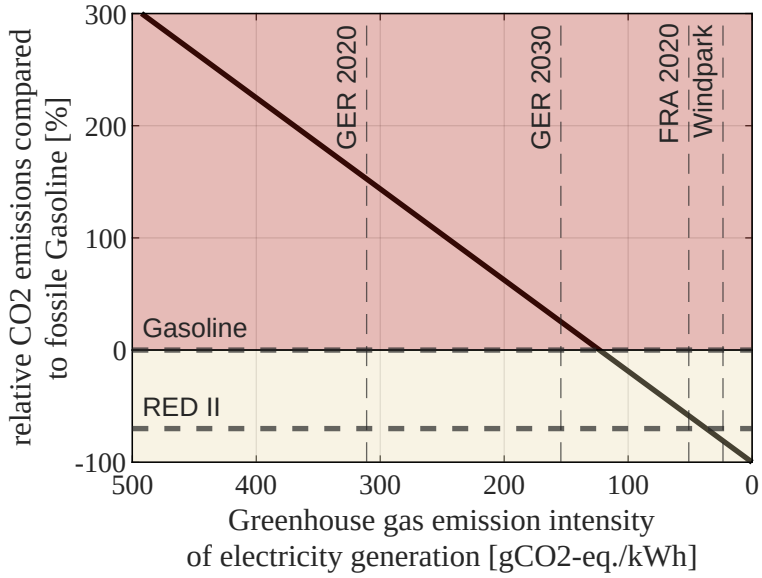

Abbildung 1.3: CO_2 eq. costs of synthetic fuel production. Sources: [2, 5, 6, 7] with the assumption that the combustion of one kilogram of gasoline produces 3.2 kg CO_2 eq.

Current status worldwide

The question that arises is: Where to produce these e-fuels efficiently. Figure 1.3 shows the potential of wind power for the CO_2 eq. generated by e-fuel production. An overview of the countries with the most potential for Renewable energy source (RES) is provided in figure 1.4. The focus is on solar energy, wind energy and their combination. It can be seen that there is little potential for renewable energy in large parts of europe, while other continents have significantly greater potential. Since there is insufficient energy available in many human agglomerations, this energy must be transported in a global strat-

egy against climate change. Liquid fuels have the advantage that they are much easier to handle and can be transported over long distances without significant storage losses.

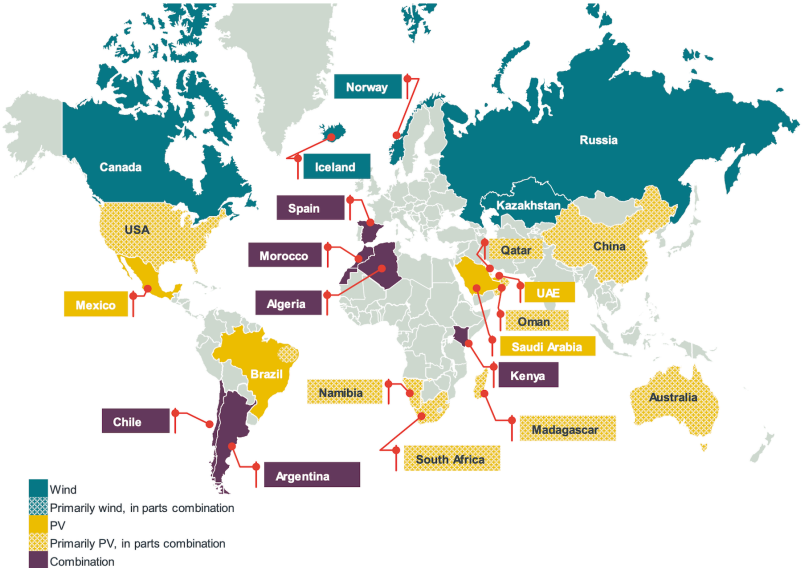

Abbildung 1.4: Worldmap with high potential of renewable energy sources [8]

To better assess the situation worldwide, it is worth looking at the world's largest passenger car market, China. Of the total registered passenger cars, 15 % are so-called New energy verhicles (NEVs) [26]. In reverse, 85 % operate with conventional fuels. Replacing the vehicle fleet with NEVs takes decades, which is why e-fuels can contribute to saving CO_2 much faster as they are also capable of being used in the existing fleet in many cases.

Dimethyl carbonate and Methyl formiate

A continuing major problem of ICEs is the emission of pollutants. The main challenge is to reduce NO_x and particulate emissions. With the upcoming EURO7 regulations [27], this is reaffirmed once again. Also RDE legislation aggravates the challenges of ICE development.

In the field of SI-Engines, engineers and developers face challanges with conventional gasoline fuel. The knock tendency and pollutant formation of the fuels continue to pose significant development effort. This means that e-fuels inhibit a vast potential for SI-Engines concepts. Novel fuels should account for those problems. At the same time, they should be compatible with the stock fleet.
Organic fuels containing oxygen are known to reduce soot emissions compared to hydrocarbon fuels. This is especially true for molecules with no C-C bonds [14]. The substances Dimethyl carbonate (DMC) and Methyl formate (MeFo) are examined in more detail for the present thesis.
DMC is often discussed as an anti-knock agent for conventional fuel. MeFo has also similar properties in terms of knock resistance as shown in table 1.1. Both molecules have an equal gravimetric heating value and stoichiometric air/fuel ratio. While MeFo is more volatile under ambient conditions, DMC is more persistent. Both substances can be produced synthetically by carbonylation of methanol. They have no global warming potential plus no ozone depletion.

Tabelle 1.1: Key properties of DMC and MeFo [14]

Name	Unit	DMC	MeFo
LHV	MJ/kg	15.8	15.8
Density@15°C	kg/m3	1079	957
RON/MON	-/-	109/>102	115/ >115
Enthalpy of vaporization	kJ/kg	418	464
A/F ratio stoich.	kg/kg	4.64	4.64
Vapour pressure (at 38 °C)	kPa	10.8	> 100
Molecule	-	$C_3H_6O_3$	$C_2H_4O_2$

The fuel mainly investigated in this work is based on a mixture of Dimethyl carbonate 65 vol.% and Methyl formate 35 vol.%. With its evaporation properties, MeFo contributes to a good mixture formation and - even in cold conditions - to good compatibility in the ICE. DMC inhibits the evaporation of the mixture,

which is advantageous in warm conditions. The specific fuel properties of the mixture are stated in chapter 2.1.

Market introduction

Currently, the incentives to introduce e-fuels into the market are insignificant. However, it makes sense to introduce this technology quickly as it can contribute to meet the Paris climate protection targets. Two different paths are of great importance:

- Drop-In with conventional Fuels
- Tailor-made e-fuels for ICEs with high efficiency

Drop-In solutions within the existing fuel standard DIN EN 228 [29] are promising due to their backward compatibility, as they incorporate the global inventory of vehicles for CO_2 reduction. In [30], it is shown that savings of CO_2 are possible by adding DMC to conventional gasoline while being compliant with fuel standards. Porsche AG has launched a project in Chile where gasoline substitute fuel is produced since 2022 and is suitable as a CO_2 neutral fuel for engines [31]. The produced fuel also complies with the fuel standard, which has the disadvantage that fundamential fuel properties remain mostly the same. This is where the strength of tailor-made e-fuels lies. They can provide optimum conditions for the ICE. The disadvantage here is that new engine concepts have to be developed to utilize the fuel's full potential. In addition, political framework conditions must be created that make it attractive to use these fuels in the first place, which is why, to the author's knowledge, there are currently no efforts outside the research sector to use these fuels. This thesis relates to these tailor-made fuels and is intended to bring conclusions about the efficiency potential into the discourse.

Economic evaluation

As there are currently no large-scale plants for the production of e-fuels, the cost per liter of fuel varies depending on the scenario considered. Uncertainties are the prices for provided CO_2 and hydrogen. CO_2 can theoretically be extracted from the environment via Direct air capture (DAC) or obtained from direct sources. However, this presupposes that the plants are located near CO_2-intensive industries. There are also significant differences in the production

method of H_2 concerning production costs. In [32] a comprehensive study on the production costs of Polyoxymethylene dimethyl ethers (OME) is presented, estimating costs of about 4 € for one liter diesel equivalent. However, due to the above factors, costs under 2 € (Assumption: H_2 costs of < 2000 € per ton and freely available CO_2 from a source) until 6.7 € (Assumption: H_2 costs of 7000 € per ton and DAC CO_2 costs of 720 € per ton) are possible. No significant cost differences compared to OME are expected for the production costs of DMC and MeFo. Due to the high cost of the fuel, there is even more focus on the efficiency of modern ICEs.

2 Fundamentals

2.1 Fluid properties of fuel mixtures

A gasoline oxygenate blend fuel Gasoline RON95 E5 85 vol.% / Methyl formate 15 vol.% (G85F15) and a pure oxygenate fuel Dimethyl carbonate 65 vol.% / Methyl formate 35 vol.% (C65F35) are investigated for the virtual engine concept designs. Table 2.1 shows the characteristic fuel properties of these fuels in comparison with Gasoline RON95 E5 (G100).

Tabelle 2.1: Key properties of the considered fuels

Name	Unit	G100	G85F15	C65F35
LHV	MJ/kg	42.2	38.0	15.8
Density@15°C	kg/m3	750.8	781.2	1041.1
RON/MON	-/-	96.8/86.3	-	117/ >120
Enthalpy of vaporization	kJ/kg	420	426	433
A/F ratio stoich.	kg/kg	14.3	13.1	4.64

Due to the Lower heating value (LHV) of C65F35, a more significant amount of fuel mass must be supplied to the system to obtain similar engine performance. As a result, a large quantity of fuel is available for evaporation. This has a direct effect on the intake air, which cools down considerably. The enthalpy of vaporization is ca. 3 % higher for C65F35 compared to G100, which further enhances the effect described above. However, the volumetric energy consumption is relatively lower due to the density, which is 39 % higher. The significantly better knock resistance is expressed by the Research octane number (RON), which is increased by more than 15 units. Due to the lower oxygenate

content of G85F15, the material properties are similar to those of G100 with a slightly lower LHV. In addition, there is no data on the RON/MON number because the fuel was not subject to chemical analysis. However, a significantly increased knock resistance was determined on the test bench, which will be discussed later.

In addition, the mixture heating value H_m is of importance. According to [15] it can be calculated using the density of the intake air ρ_L, the Air/Fuel ratio λ and the stoichiometric Air/Fuel ratio L_{st}:

$$H_m = \frac{LHV \cdot \rho_L}{\lambda \cdot L_{st}} \tag{2.1}$$

With values of table 2.1 the theoretical air needed for the same power output is approx. 14 % lower for C65F35 than with G100, which means that the engine displacement volume can be smaller for the same amount of energy provided to the combustion chamber at stoichiometric conditions.

2.1.1 Ignition delay

The ignition delay times and laminar flame speed are two further important parameters for the engine process. With the help of reaction kinetics simulation described later, the material properties of the fuels can be compared.
Figure 2.1 shows the ignition delay times for G100, G85F15, and C65F35 at a stoichiometric Air/Fuel ratio. The quantity of the abscissa is 1000/K, which means that the temperature decreases as the value increases. C65F35, unlike G100, does not show a two-stage ignition (TSI) / negative temperature coefficient (NTC) behavior. This has an extreme effect on the area of temperatures higher than 1.0 1000/K. The ignition delay times increase by over an order of magnitude for C65F35 above this value. Since the relevant part of the engine operation is between approx. 0.8 and 1.2 1000/K at pressures higher than 20 bar, the significantly lower knocking tendency can be seen directly. The small amount of MeFo within G85F15 does not lead to notable different ignition delay times compared to G100 in the reaction kinetic simulation.

2.1.2 Laminar flame speed

Figure 2.2 shows the laminar flame speed for three different boundary conditions for the fuels under consideration in dependence of the Fuel/Air equivalence

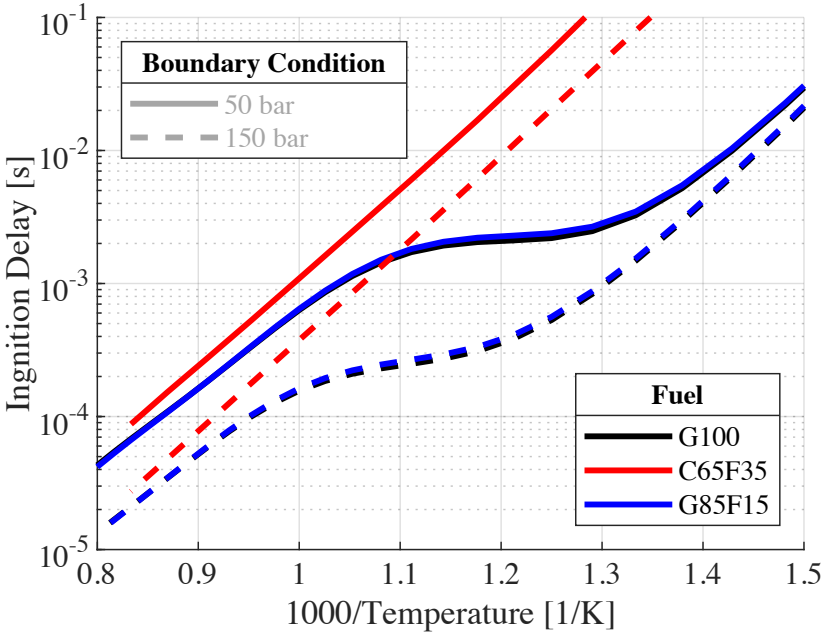

Abbildung 2.1: Ignition delay times calculated for different fuels (Reaction mechanism G100 and G85F15: [9], C65F15 [10])

ratio. For the different fuels, it can be seen that C65F35 has lower laminar flame speeds compared to G100 and G85F15. The admixed MeFo portion of the gasoline blended fuel has only a minor effect on the laminar flame speed. Furthermore, it can be seen that the decline of the C65F35 graph is less in the direction of lean mixture ($\phi < 0.8$), which is of interest for lean-burn engine concepts. With increasing charge dilution, combustion misfires can occur due to the inhibited flame propagation.

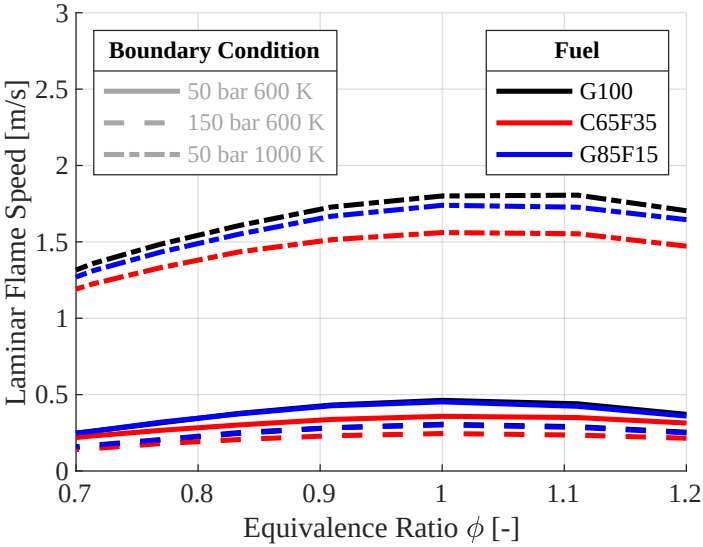

Abbildung 2.2: Laminar flame speed calculated for a different Fuel/Air mixture (Reaction mechanism: G100 and G85F15 [9], C65F15 [10])

2.2 Efficiency and technology overview of the ICE

2.2.1 Efficiency of the ICE

The efficiency η of homogeneous SI-Engines can be expressed by the thermodynamic simplification of an isochoric process. In this case it depends only on the compression ratio ε and the heat capacity ratio γ:

$$\eta = 1 - \frac{1}{\varepsilon^{\gamma-1}} \tag{2.2}$$

The efficiency can be raised by increasing both values. ε is limited due to the geometrical framework of the engine and the knocking behavior of the fuel in high load areas. γ is determined by the gas composition in the combustion chamber.

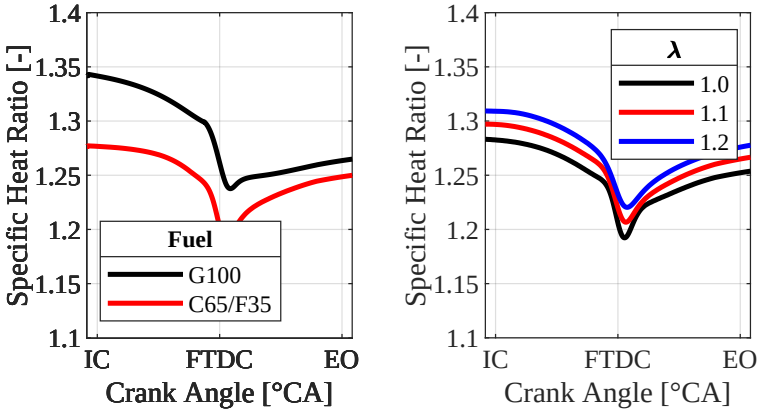

(a) Exemplary curve of specific heat ratio γ for different fuels

(b) Influence of λ on the specific heat ratio

Abbildung 2.3: Effect of the fuel and the Air/Fuel ratio on the specific heat ratio γ for load points with the same IMEP

Figure 2.3 (a) shows exemplarily the progress of γ over the engine process from intake valve closes (IC) to exhaust valve opens (EO) for an engine load point with a similar indicated mean effective pressure (IMEP) at stoichiometric conditions operated with different fuels. C65F35 has a 6 % lower specific heat ratio at IC, leading to a slightly lower efficiency potential. Towards EO, the values converge to some extent. Figure 2.3 (b) shows the influences of charge dilution. With leaner gas mixture, γ increases.
Figure 2.4 shows the calculated theoretical efficiency stated in (2.2) with the mean values of the specific heat ratio over the high pressure engine cycle for C65F35 (1.27) and G100 (1.30). Exemplarily, with a compression ratio of 12, this leads to a theoretical efficiency of 49 % resp. 53 %.
The examinations above are based on an ideal process without losses that reduce the efficiency. These losses can be quantified in the form of energy flows which lead to a decrease in efficiency. These losses are listed in table 2.2:

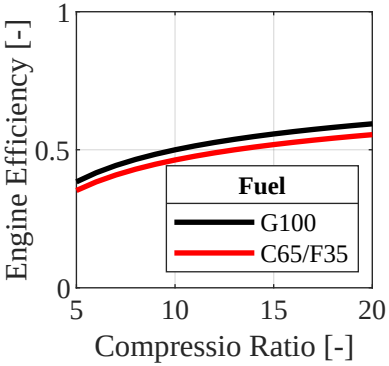

Abbildung 2.4: Effect of compression ratio on engine efficiency for different fuels

Tabelle 2.2: Engine process losses [15]

wall heat	Loss due to heat transfer to the combustion chamber walls
combustion	The energy is supplied via the time-depended heat release rate. Energy added before Firing top dead center (FTDC) counteracts the compression, while energy added after FTDC no longer acts during the entire expansion stroke.
mechanical	Losses due to engine friction (connecting-rod bearings, between piston and cylinder wall) and auxiliary units. (oil pump, cooling water pump, fuel pump)
gas exchange	Expansion and compression losses resulting from the pressure difference between inlet/outlet and combustion chamber, as well as the air resistance.
exhaust gas	Due to incomplete and imperfect combustion, unburned molecules are discharged. In addition, due to the time-dependent process of heat transfer, thermal energy is contained in the exhaust gas, which is lost.

With regard to efficiency, it is essential to know the limitations that occur due to uncontrolled autoignition. This so-called knock phenomenon limits the efficiency of the engine. It mainly occurs at high engine loads and low engine speeds. The premixed charge ignites in the unburned area outside the flame front. Pressure waves are caused, which can lead to high mechanical and thermal stresses on the engine. If this is the case over a longer period of time, it can lead to the complete destruction of the engine. To protect the engine components, the ignition angle is shifted late in order to avoid high peak pressures and temperatures. This reduces efficiency but makes the mixture less prone to uncontrolled autoignition.

2.2.2 State of the art in ICE technologies

Downsizing

Downsizing is applied to reduce the fuel consumption of the engine. Several approaches are combined to achieve the desired effect. In general, the engine displacement volume is reduced whereby the engine operating points are shifted towards higher indicated pressures to gain a similar power output. The air mass supplied to the engine must be of the same magnitude. This can be done by using a turbocharger or by increasing the turbocharger's boost pressure.

Four advantageous effects result from downsizing. Smaller engines usually have smaller bearing surfaces, which reduces friction losses, while turbochargers can reduce gas exchange losses. Due to the higher load in the engine, the ratio of the work process to friction losses is also significantly higher, resulting in additional efficiency advantages. The smaller combustion chamber surfaces reduce wall heat losses. With fuels that tend to knock behavior, this measure can lead to disadvantages, since the ignition angle has to be adjusted late and thus the center of combustion deviates from the optimum position and further, the combustion duration is extended [33, 34]. In [35], a simulation study of a extreme downsizing concept is shown. A 2.0 liter SI-downsizing engine was compared with a highly downsized engine concept of 1.2 liters resulting in a fuel consumption reduction of up to 15 %.

To fully utilize the potential of the turbocharger in downsizing concepts, direct injection is also usually used here. The cooling effect in the combustion

chamber due to the evaporation enthalpy reduces the knock sensitivity, allowing higher compression ratios to be achieved. In addition, the advantages according to [33] are the possibility of realizing higher valve timing overlaps, resulting in better purging of residual gas and a higher volumetric efficiency. The study mentioned above [35] also investigated the injector position, where the challenges of a central injector for downsizing concepts are addressed. It is shown that the valve diameters can be increased with a lateral injector position, and thus, an effort is necessary concerning charge filling with a central injector position.

Valve actuation strategies

For high-efficiency powertrains, the design of the valve lift curves and valve timing is essential for the engine's efficiency. The miller cycle is a process in which the inlet valve closes before BDC. This can be achieved in two ways: Opening the intake valve earlier with the same valve lift curve or reducing the valve lift. In both cases, there is a phase in which the combustion chamber expands the charge air before it is compressed. For a similar intake temperature and cylinder mass, this leads - from a thermodynamic point of view - to lower pressures and temperatures at BTC compared to conventional valve control. This means that the process pressures and temperatures are lower with the same charge, which improves the knocking behavior and wall heat losses. Another advantage is de-throttling in part-load operation, which keeps gas exchange losses low. These advantages come at the price of a less efficient charge motion since lower valve lifts inhibit tumble build-up. In addition, the considerable valve overlap leads to more residual gas remaining in the cylinder. Higher boost pressure is also required to achieve similar charge levels as conventional valve trains at high loads. A comprehensive simulation study of fully variable valve timing is presented in [36]. The focus is specifically on optimizing the timing concerning engine efficiency and emissions. The results predict efficiency gains of 2 % at full load and 4 % at part load with optimized valve timing.

Another study on the variable valve train is shown in [37]. The highest efficiency gains (5 %) are achieved by de-throttling the engine at partial load with a suitable miller strategy. Therefore, it makes perfect sense for highly efficient engine concepts to implement variable valve timings in combination with a miller cycle.

Variable compression ratio

The knock behavior of SI-Engines limits the compression ratio. The compression ratio must be specified so that it ensures reliable operation over the entire engine map. This leads to the fact that this value may be theoretically significantly higher at low loads but must be lower in the full load range to avoid knocking. The variable compression ratio offers a solution to this problem. Thus, it is possible to operate the engine with optimum efficiency over a wide engine map range without retarding the ignition angle. Two different approaches are presented in the following: A system is shown in [38] in which the compression rate can be adjusted between values of 9 and 14 full variables, which theoretically allows the optimum setting for each load point. This involves adjusting an excentric shaft on the crankshaft to change the connecting rods' penetration behavior. In cooperation with PSA, a demo vehicle was developed that achieves CO_2 savings of 8 % in the Worldwide harmonized light vehicle test procedure (WLTP). The drawback is the complexity of the system and the resulting costs.

Another approach is presented in [39]. In this case, the system can adjust the compression rate in two stages. The compression ratio adjustment takes place directly at the piston boss of the connecting rod. A compression ratio of 8 in the lower stage and 13 in the upper stage leads to consumption advantages of 5 % in WLTP.

Cylinder deactivation

The cylinder deactivation technology helps to keep the engine in the most optimal operation mode for the performance requirements. This is used for multi-cylinder engines. In areas with low load requirements, the valves of individual cylinders are kept closed, and the injection is deactivated. Due to the closed valves, the enclosed air acts like a gas spring, and, apart from minimal friction losses, these cylinders do not affect the engine process. The active cylinders must compensate for the deactivated ones, so they run at a higher load, resulting in lower gas exchange losses.

For a WLTP cycle, [40] shows a fuel consumption advantage of 6.4 % for a 4-cylinder 1.8 liter engine using cylinder deactivation. This technology has excellent advantages at low loads. Higher loads can have a negative effect on effi-

ciency, for example, if the cylinders reach the knock limit. Since de-throttling can also occur with charge dilution or Exhaust gas recirculation (EGR), the advantage depends on the resp. load point.

High Turbulence / Advanced Ignition concepts

High turbulence or advanced ignition concepts address the burn duration in the engine. A high-turbulence concept aims to generate a strong charge motion in the combustion chamber. In the top dead center region, the charge motion in the shape of a tumble flow decays into turbulent energy. This is responsible for the rapid flame propagation in the combustion chamber. Tumble flaps, an adapted combustion chamber geometry, or the intake port design can lead to a high tumble motion. The reader can find measures to increase the charge motion and its impact on the efficiency in [41] and [42].

Another way to reduce the burn duration are pre-chamber spark plugs. The idea here is not to limit the ignition source to a small area in the combustion chamber, like with conventional spark plugs. Flame jets are directed into the combustion chamber through the pre-chamber, igniting the mixture at various points. This technology can reduce burn duration by up to 1.5 times as shown in [43].

These technologies are also very suitable in combination with other applications. Faster combustion can, for example, reduce the tendency to knock as the mixture converts more quickly. This allows the usage of higher compression ratios. It also stabilizes the combustion and can increase the degree of charge dilution for lean engine concepts with reduced cycle-to-cycle fluctuations.

A disadvantage of high-turbulence concepts is the gas exchange. The increased charge movement results from higher pressure losses in the intake stroke. Pre-chamber systems do not have this drawback, but the system integration is more complex. For both technologies, the faster combustion increases the peak pressures, which leads to higher mechanical and thermal stresses. This also harms the noise, vibration and harshness (NHV) behavior.

Lean operation / EGR

The idea with lean operation or EGR is to de-throttle the engine (lower gas exchange losses) and also make it more resistant to knocking. Additional mass in the combustion chamber can capture heat energy as its heat capacity leads to lower process temperatures. This has a positive effect on wall heat losses and knocking behavior.

Two fundamental things are different about these technologies. In lean operation, the 3-way catalytic converter is no longer effective, making NOx emissions a challenge for exhaust gas after-treatment. This is not the case for stoichiometric operation with EGR. For lean operation, the process temperature must be lowered until the NOx emissions are in a range where exhaust gas after-treatment can convert them to a level that complies with the emission legislation. However, combustion misfire occurs if the charge dilutes too much, making an efficient operation impossible. On the other hand, knock resistance is more likely with EGR since it is an inert gas that is not participating in reactions, as opposed to excess air in lean-burn operation. A virtual lean engine concept is presented in [44] . In part-load operation, the virtual gasoline engine operates with λ of 1.9. In combination with a fully variable valve train, a high-turbulence concept using tumble flaps, and a powerful spark plug, an efficiency increase of 15 % relative is achieved compared to a stoichiometric approach resulting in an indicated efficiency of 46 %.

The effect of the EGR on the engine at high loads is investigated in [45]. It is shown that the EGR significantly improves the fuel's tendency to knock. Also the cooling provided by the EGR eliminates the need for full-load mixture enrichment, enabling efficiency gains of up to 15 % in this area. In [46], the effect of EGR at part load is shown. De-throttling and a lower wall heat loss can result in efficiency gains of up to 6 % at 28 % EGR.

Turbocharger

In a turbocharged engine, the charge air is compressed by a turbocharger before entering the engine. The turbocharged engine, which has the same displacement as the naturally aspirated engine, provides the same air volume, but the higher pressure of the working medium results in higher air mass entering the combustion chamber. From the point of view of engine development, this

gives additional degrees of freedom. More fuel can be added to the combustion chamber so that the engine's power output increases at the same speed and with the same displacement volume. Another possibility is to increase the proportion of charge air so that the engine delivers the same power but combustion takes place at different Air/Fuel ratios, which offers an opportunity for lowering emissions and increasing efficiency [33].

The great advantage of the turbocharger is that it can recover parts of the energy contained in the exhaust gas and return it to the system. The most important representatives for controlling turbocharger performance are the waste gate turbocharger and the variable geometry turbine (VGT). For the first variant, the exhaust gas mass flow is bypassed by the turbocharger via a waste gate valve, which reduces the exhaust gas enthalpy used in the turbocharger. The VGT uses adjustable vanes on the exhaust side to regulate the direction of flow to the turbine blades.

A proper turbocharger design plays an essential role for the ICE, as it is directly responsible for the exhaust backpressure and the boost pressure build-up. It therefore becomes evident that efficient turbochargers can achieve a significant performance gain for the entire system. For both variants of the exhaust gas turbocharger, research is constantly being conducted into new measures to increase efficiency. Big levers are the bearings of the turbocharger (4 % turbocharger efficiency gain [47]), clearance between turbine/compressor and the housing [48] and a continuously improving manufacturing process, which allows the realization of more complex geometries [49].

A new generation of turbochargers is introduced by Gerret Motion Inc [50]. The conventional turbo is combined with an e-machine. The advantage is that the turbocharger size no longer has to be optimized for low mass flows. In this area, the e-motor supports the turbocharger so that it directly powers the turbocharger shaft. This means that the turbocharger can be designed straight for rated power. In addition, this hybrid technology also offers the possibility of recuperating electrical energy via the turbocharger. Premium segment vehicles will initially use this technology, but as a result of increasingly stringent emission standards, it could soon be available in the mainstream segment as well.

SI-Engine fuel

All of the technologies mentioned above have been developed to get maximum efficiency out of conventional fuels. However, since not all properties of gasoline are entirely satisfactory, the fuel used is a significant lever in terms of efficiency and emissions. Desirable properties of the fuel are complete knock-free behavior, high flame speeds, and low air pollution tendency. In [51] a blended fuel consisting of gasoline and methanol was investigated. It has been shown that brake efficiency improvements of up to 8 % already occur at 20 % methanol blending with lower HC and CO emissions. The efficiency gain results from a better center of combustion due to the better knock behavior. A simulation study by [42] shows the enormous potential of a pure methanol engine. A virtual concept was designed that achieves more than 45 % brake efficiency in broad engine map ranges for a passenger car.

The advantages of the individual technologies described above do not always add up. A comprehensive study on the combination of technologies and their mutual influence was conducted in [42]. This thesis attempts to achieve the highest possible efficiency through a broad usage of technologies.

2.3 0D/1D Simulation

Now that the opportunities, challenges, and properties of e-fuels have been discussed, it is essential to quantify their potential precisely. Developing new engine concepts based on test bench experiments with different fuels would involve an almost unmanageable amount of work. Therefore, sophisticated simulation techniques are used to support the development process. For this to work, the combustion process in the ICE with its fuel influence must be reproduced as accurately as possible. The engine simulation tools are presented below for the central task of engine concept design in this work.
The results are generated using 0D/1D simulation methods. The 1D simulation with the commercial tool GT-Power [53] is used to model engines, vehicles, and their driving cycles. Geometries are discretized only in the direction of flow. This approach allows very extensive systems to be modeled, which would be almost impossible with multidimensional calculation methods due to computational resources. The engine simulations' centerpiece is the FKFS

UserCylinder [54] representing the combustion chamber in the 1D models. The functionality of this 0D simulation method is described in the following.

2.3.1 Pressure trace analysis and working process calculation

Engine measurement data can be analyzed using a Pressure trace analysis (PTA). The aim is to obtain information about the burn rate of the engine process. The following axioms are used for the calculation:

- First law of thermodynamics
- Equation of state
- Mass balance

The **first law of thermodynamics** can be stated between intake port closes, and exhaust port opens with equation (2.3) (blow-by is neglected):

$$\frac{dQ_b}{d\varphi} = \frac{dU}{d\varphi} - \frac{dQ_w}{d\varphi} + p_c \cdot \frac{dV}{d\varphi} \tag{2.3}$$

$dQ_b/d\phi$ is the burn rate to be calculated. This value can be interpreted as the conversion of the chemically bound energy per time step. The burn rate can be expressed by the mass converted during combustion $dm_b/d\phi$ and a constant of proportionality - the lower heating value H_u (Eq. (2.4)). The cylinder pressure p_c and $dV/d\phi$ (Eq. (2.3)) are available from test bench measurement. Furthermore, models for the wall heat energy dQ_w and calorific values for calculating the internal energy dU are necessary.

$$\frac{dQ_b}{d\varphi} = H_u \cdot \frac{dm_b}{d\varphi} \tag{2.4}$$

The change of internal energy can be calculated by using the Equation **Equation of state** (Simplification: constant cylinder mass m_c, constant calorific value R and c_v is independent in pressure and species composition):

$$\frac{dU}{d\varphi} = m_c \cdot c_v \frac{dT}{d\varphi} + p\frac{dV}{d\varphi} = \frac{c_v}{R}\left(p\frac{dV}{d\varphi} + V\frac{dp}{d\varphi}\right) + p\frac{dV}{d\varphi} \tag{2.5}$$

with:

$$p\frac{dV}{d\varphi} + V\frac{dp}{d\varphi} = m_c \cdot R \cdot \frac{dT}{d\varphi} + R \cdot T \cdot \frac{dm_c}{d\varphi} + m_c \cdot T \cdot \frac{dR}{d\varphi} \tag{2.6}$$

In this work, a two-zone approach to the combustion chamber is used. This means that the combustion chamber is separated into two different thermodynamic zones during the combustion process. The unburned zone and the burned zone have the same pressure with different temperatures and, therefore, different densities, leading to a non-proportional ratio of mass to volume distribution. The heat of combustion is only released in the burnt zone, resulting in more realistic temperatures due to better consideration of the chemical dissociation. Also, the wall heat energy can be subdivided into energy flows from the unburned and burned zone. Accurate prediction of emissions is only possible using a two-zone approach [55].

It is important that the **mass balance** is maintained in the two-zone approach (cylinder mass m_c, mass in the unburned zone m_{ub} and mass in the burned zone m_b):

$$m_c = m_b + m_{ub} \tag{2.7}$$

$$\frac{dm_c}{d\varphi} = \frac{dm_b}{d\varphi} + \frac{dm_{ub}}{d\varphi} \tag{2.8}$$

To generate reliable results for the development of virtual engine concepts, the challenge is to reproduce the burn rate calculated from the PTA with predictive models. In the **working process calulation** the burn rate is modeled and the cylinder pressure curve can be calculated using equation (2.3) whereby all relevant engine parameters can be derived (Indicated work W_i, indicated mean effective pressure p_{mi}, indicated power P_i, indicated engine efficiency η_i, indicated specific fuel consumption b_i).

Since the phenomenological modeling of the burn rate is subject to further influences, the following models are also required for a valid forecast:

- Charge motion
- Turbulence model
- Auto-ignition
- Knock model

The models are precisely described in chapter 3.

2.3.2 Thermodynamics of the burned gas and vapor fuel

The calorific material properties of the burned gas are obtained from the chemical equilibrium calculation. The reactants' concentration can be determined with equilibrium constants, which are determined by their thermodynamic properties. Reaction equations are set up for 11 species (see figure 2.5), assuming establishing the equilibrium is fast compared to the working process calculations time step. Since the number of atoms of the fuel-air mixture does not change during combustion, the ratio of atoms and the reaction equations can be used to set up a non-linear system of equations. The specific enthalpy and the specific gas constant can then be summed up for the individual species. The exact procedure with many further details is described in [56].

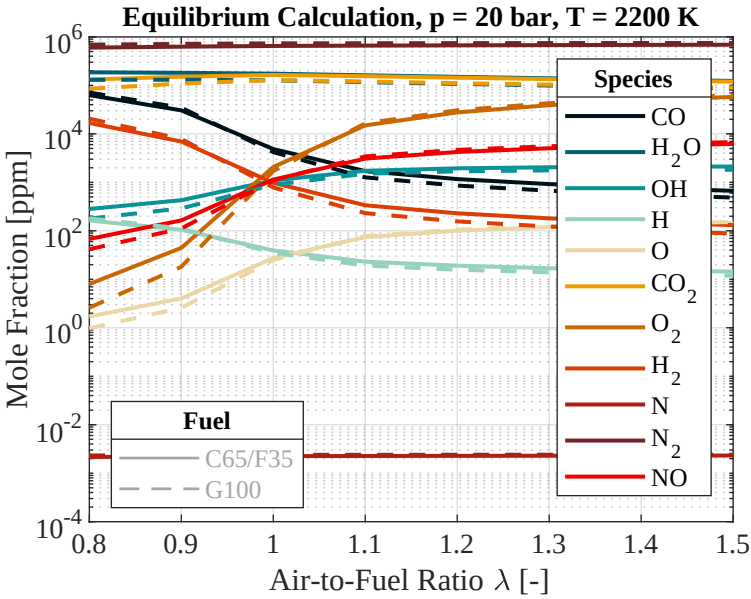

Abbildung 2.5: Overview of the single species in the burned zone for different fuels

Figure 2.5 shows the species calculation for G100 and C65F35 with different Air/Fuel ratios. Due to the different atomic ratios of the fuels, the chemical equilibrium changes, which impacts the calorific values of the working process calculation. It is clearly seen that the oxygen atoms already carried in

C65F35 reduces the amount of molecular nitrogen in the engine at constant Air/Fuel ratio.

It should be mentioned that this approach does not lead to desired results for pollutant calulation. The NO concentration is a particular case where the reverse reaction freezes at a certain temperature level. The equilibrium calculation cannot be applied in this case for a pollutant forecast. Therefore, a different modeling method is described later.

The calculation of the caloric material property of the vapor fuel is done analogously to [56] by the atomic ratio of C, H, and O. A reference curve was defined for standard fuels. This curve is multiplied by a C/H/O dependent constant to account for different fuels. The validity of this approach for different fuels is shown there.

2.4 Reaction kinetics simulation

Determining laminar flame speeds and ignition delay times of C65F35 are essential for simulating phenomena in the combustion chamber with predictive models. These values depend on the investigated substances' pressure, temperature, and composition. The measurement of these values is very complex in engine operating conditions. Therefore a simulation approach is used. The investigations are carried out with the open-source tool Cantera [57]. This tool solves the conservation equation of mass, energy, and species by taking molecular transport processes and reaction kinetics into account. Reaction rates k are calculated using (2.9) with empiric defined values for the Frequency factor a, Temperature exponent b and Activation energy E_A.

$$k = a \cdot T^{\mathrm{b}} \cdot exp\left(\frac{-E_\mathrm{A}}{R \cdot T}\right) \tag{2.9}$$

The choice of a suitable reaction mechanism is required to calculate the laminar flame speed and ignition delay times. For C65F35, the mechanism described in [9] is used. Since this mechanism is not designed for high chain gasoline molecules, a modified mechanism [10] is applied for G85F35.

In Cantera, one-dimensional, premixed stationary flames are simulated. Along with the flow direction, pressure, density, species concentration, temperature,

and laminar flame thickness are calculated. The equations that are solved are described precisely in [58]. The laminar flame speed is defined as the flame propagation in a quiescent gas mixture of fuel and oxidizer. In the case of a stationary flat flame front, the laminar flame speed equals the flow velocity of the fuel and oxidizer.

The solving approach for ignition delay times is based on an ideal gas simplification of a zero-dimensional method. The heat release of reactions taking place is calculated in a constant pressure reactor. To calculate the ignition delay times, a criterion must be defined at which auto-ignition occurs. This work's criterion is based on a defined temperature increase of 400 K to the initial state in the reacting mixture. This ensures that pre-reaction states have already been expired.

Tabelle 2.3: Reaction mechanism overview

Name	Mechanism 1	Mechanism 2
Surrogate	C65F36	G85F15
Species	185	522
Reactions	1174	2299
Reference	[9]	[10]

The measurement based validation of the mechanisms was carried out for temperatures between 700 and 1250 K and 20 to 40 bar pressure with good agreement [10]. Important to take into account is that elementary reactions follow well-examined principles. It is reasonable to use a reaction mechanism beyond its range of validation. Results from the reaction kinetic simulations are discussed in detail in chapter 3.

2.5 3D CFD simulation

The burn rate, thermodynamic variables, fuel consumption, etc., can be calculated accurately with methods of the 0D/1D simulation. However, due to the

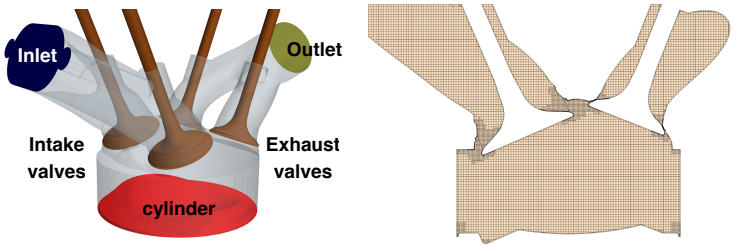

(a) Engine Geometry **(b)** Schematic mesh

Abbildung 2.6: Pre-Processing of the CFD engine geometry

reduced dimensions, a real geometry's effects on these variables are not considered. For the correct prediction of the charge motion and the turbulence level in the combustion chamber, which are modeled in the 0D/1D simulation, it is essential to make statements about those geometric effects. Therefore, 3D Computational fluid dynamics (CFD) simulation methods can be used to account for actual geometries. The 0D/1D models are adjusted using the results of the 3D simulation. This proceeds as follows: A PTA with measured data is performed to have suitable boundary conditions for the 3D CFD. The time-dependent variables, i.e., inlet/exhaust pressure and temperatures, valve timing, and combustion chamber wall temperatures from the 0D/1D simulation are set as boundary conditions. The engine geometry is built and meshed, and appropriate solver settings are applied. Subsequently, the calculation with the commercial tool STAR-CCM+ [59] is performed.

Geometry, mesh and solver settings

Figure 2.6 (a) shows the geometry of the Single-cylinder research engine (SCE) with the boundary conditions' position at the inlet- and outlet-port. It is mandatory to provide a closed geometry with fixed part names for the In-Cylinder tool of STAR-CCM+, which helps simplify the pre-processing process. Figure 2.6 (b) shows the mesh of the imported geometry. At BDC it contains over one million cells.
Table 2.4 shows mesh setting parameters the user needs to predefine. The normalized valve curtain interface position separates the combustion chamber from the port volumes. Adjusting this parameter helps improve the mesh qual-

ity and convergence. The mesh itself is a dynamic mesh, which means that if the cell quality falls below a certain level, remeshing is initiated. Criteria for remeshing are predefined, and the program itself carries out this process automatically.

Tabelle 2.4: CFD mesh and solver settings

Parameter	Unit	Value
Base size	mm	0.8
Normalized valve curtain interface position	-	15
Minimum size	mm	0.4
Prism layer thickness	mm	0.2
Number of layers	-	1
Simulation duration	°CA	720
Turbulence model	-	Realizable $k-\varepsilon$
Injection	-	Reitz Diwakar Breakup
Combustion model	-	ECFM-CLEH
Ignition model	-	ISSIM

The adjustment parameters of the combustion model are given in the appendix. The evaluation variables needed to assess the charge motion and the turbulence level in the combustion chamber are presented below.

Evaluation variables

Tumble is defined as the fluid rotation about the plane that contains the origin and that is orthogonal to the cylinder axis. The tumble motion Tu_{CFD} concerning a specific cylinder axis is calculated as follows [59]:

$$Tu_{CFD} = \frac{1}{2}\left(\left(-Ax_z\frac{L_y}{\omega_c \cdot I_y}\right)^2 + \left(Ax_z\frac{L_x}{\omega_c \cdot I_x}\right)^2\right) \tag{2.10}$$

In this example the tumble is calulated about the z-axis Ax_z with the angular momentum L about the x- and y-axis, the angular speed of crankshaft ω_c and the moment of inertia I about the x- and y-axis. This dimensionless index reflects the progression of tumble intensity throughout the engine process. Figure 2.7 shows the developed tumble flow with the help of streamlines in the compression stroke. The conversion of this kinetic energy into turbulence is essential in the combustion process development. The higher the turbulence level during combustion, the faster the fuel is converted. This is only valid to a certain degree of turbulence since an excessively high degree of turbulence can lead to flame quenching [60].

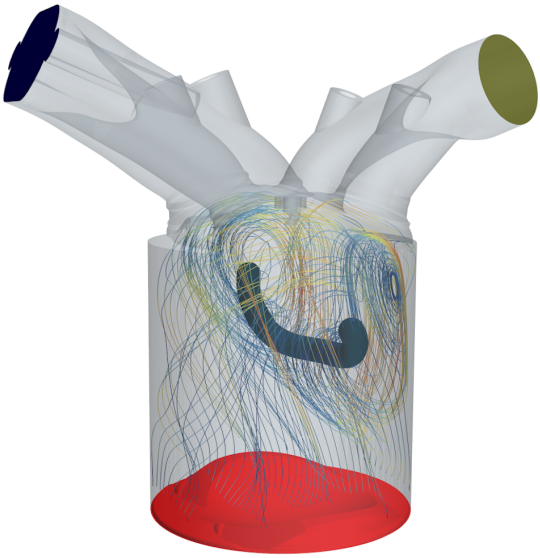

Abbildung 2.7: Schematic visualization of the charge motion in the simulation. The tumble center is depicted as a vortex core

The following is a more detailed description of turbulence: Turbulent flow is a fluid motion characterized by a chaotic change in velocity. The schematic progression of a turbulent velocity over time is shown in figure 2.8. This turbulent velocity can be expressed with a mean velocity $\bar{u}$ and a fluctuation velocity u'

(2.11).

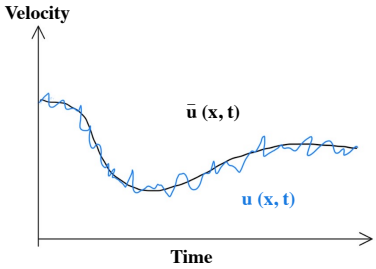

Abbildung 2.8: Schematic visualization of the turbulent and mean velocity

$$u(x,t) = \overline{u}(x,t) + u'(x,t) \tag{2.11}$$

With knowledge of the fluctuating velocity in each direction of space, the Turbulence kinetic energy (TKE) can be calculated with eq. (2.12).

$$k = \frac{1}{2} \cdot \left({u'_x}^2 + {u'_y}^2 + {u'_z}^2 \right) \tag{2.12}$$

Since the Reynolds-averaged Navier-Stokes equations (RANS) have a homogeneous isentropic turbulence, it can be expressed as follows:

$$k = \frac{3}{2} \cdot u'^2 \tag{2.13}$$

The evaluation of the TKE is carried out via mass averaging of every cell in the combustion chamber. The calibration of the 0D simulation models is then performed directly using the tumble and the TKE progression of the 3D CFD simulation.

The aforementioned allows a better interpretation of the following results of an exemplary CFD calculation. Figure 2.9 shows the progression of the tumble and the TKE for an engine cycle of 720 $°CA$ for G100 and C65F35. The figure's upper area schematically depicts the injection, valve opening, and closing event. Both fuels have the same valve timing but different injection durations. The tumble propagation in figure 2.9 (a) can be subdivided into four main phases. The first one is the tumble generation due to the inflow (starting from TDC). The injection event follows thereafter. As the engine volume decreases, the tumble flow spins up before it decays at Firing top dead center (FTDC).

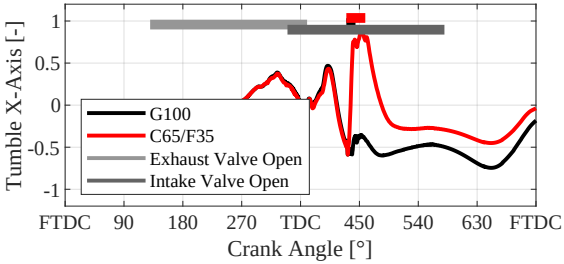

(a) Tumble progression

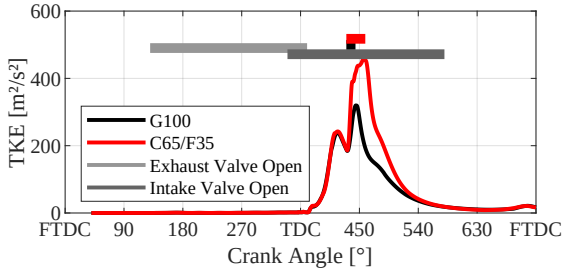

(b) TKE progression

Abbildung 2.9: Tumble and TKE progression over an engine cycle for the fuels G100 and C65F35

The injection counteracts the tumble build-up resulting from the inflow in the combustion chamber in this example. This effect comes from a laterally injector positioned injector. A higher injected mass for C65F35 leads to a lower tumble level, which is disadvantageous for generating a high TKE at combustion start. At the same time, this clarifies that the injector position and injection timing is of great importance, especially with C65F35. Other configurations of the injector could be supportive for a beneficial tumble progression.

A similar situation can also be observed with the TKE. The inflow and injection event produce a high amount of TKE. After the end of the injection, the TKE dissipates very quickly. The kinetic energy is stored in the macroscopic motion. As the tumble decays in the last phase, TKE is produced again.

This result shows that predictive models must be able to represent these complex phenomena and take the individual phases of charge motion into account correctly. For this assessment, many more CFD studies are needed, which are discussed in the following chapter. Also, the interaction between injection and charge motion is investigated in greater detail.

3 Modeling

3.1 Test bench data

All data used for the model adjustment in this thesis are based on measurements from a Single-cylinder research engine (SCE) and a Series 4-cylinder engine (4CE). The specifications according to [52] are as follows:

Tabelle 3.1: Specification of test carriers

Name	Unit	SCE	4CE
Cylinders	-	1	4
Displacement volume	cm^3	463	1984
Compression ratio	-	11 / 15	9.6 / 15
Max. IMEP	bar	17	24
Max. speed	1/min	3500	6800
Bore/Stroke ratio	-	0.95	0.89

The SCE test bench is operated with the reference fuel G100, G85F15, and C65F35. Measurement data with different boundary conditions are available. The investigation includes variations of engine load, engine speed, intake temperature, start of injection (SOI), and charge dilution. In the process of the inquiry, the compression ratio was adjusted due to the high knock resistance of C65F35. At the 4CE test bench, an application of a series engine was carried out. Therefore, a vast number of engine speed and torque variations are available for C65F35.

Both engines have a direct injection (DI) lateral injector. The SCE has a fixed valve timing, while the 4CE is equipped with a variable camshaft. The intake port of the 4CE includes a tumble flap which allows a modification of the charge motion. The Bore/Stroke ratio of the combustion chamber differs for both engines.

The indication system uses three piezo sensors for intake, exhaust, and in-cylinder pressure. A wideband λ probe is installed downstream of the exhaust manifold, and NO_x emissions are measured using a chemiluminescence detector. The engine load controller regulates the air mass flow using the intake throttle position, while the λ controller varies the fuel mass flow by injection duration. One main cycle includes all measured data averaged over 200 cycles, while each pressure trace of the single cycles is available, too [52].

A variation of the intake temperature was performed on the SCE to obtain data for the knock behavior of C65F35. The test bench was operated stoichiometric with a compression ratio of 15 at 1500 RPM and 17 bar IMEP. This variation is discussed in more detail in chapter 3.4.

3.2 Charge motion and turbulence model

The calculation of the charge motion and turbulence in the combustion chamber follows an approach presented in [61] which is a merge of models from [62], [63] and [64]. Equation (3.1) states the impact of individual source terms on the angular momentum L_T of the change flow. These source terms include the change of angular momentum due to inflow and outflow, shear forces of the main flow, shear forces due to wall interaction, spin-up through the piston movement towards TDC, and direct injection.

$$\begin{aligned}\frac{dL_T}{dt} = \left(\frac{dL_T}{dt}\right)_{in/out} + \left(\frac{dL_T}{dt}\right)_{shear(Internal)} + \\ \left(\frac{dL_T}{dt}\right)_{shear(Wall)} + \left(\frac{dL_T}{dt}\right)_{spin-up} + \left(\frac{dL_T}{dt}\right)_{DI}\end{aligned} \tag{3.1}$$

The single terms are described in great detail in the publications mentioned above. Two terms for the change of angular momentum are discussed in detail,

which are of great relevance for this work.

The tumble production based on in- and outflow is calculated with equation (3.2).

$$\left(\frac{dL_T}{dt}\right)_{in/out} = \begin{cases} \frac{2 \cdot T_{Tipp} \cdot \dot{m}^2}{\rho_c \cdot B}, \dot{m} \geq 0 \\ L_T \cdot \frac{\dot{m}}{m_c}, \dot{m} < 0 \end{cases} \tag{3.2}$$

The mass flow $\dot{m}$, fluid density ρ_c, the bore diameter B, and the angular momentum L_T derived from the tumble Tu_{CFD} in equation (2.10) are accessible from the 3D CFD simulation. Therefore, a Tippelmann number T_{Tipp} for the 0D/1D simulation can be calculated by rearranging the equation. This variable indicates the intensity of tumble production by the flow in and out of the combustion chamber. Fritsch et. al. [61] have shown via 3D CFD that the inflow jets of the stationary test bench differ from a dynamic engine operation. The reason is stated in the downward motion of the engines' piston, which influences the charge motion. The flow is pulled down towards the rotational center, leading to a more moderate tumble build-up compared to the tumble motion in a stationary test bench. By deriving the coefficient from 3D CFD data, better results can thus be obtained.

Figure 3.1 shows the derived dynamic tumble coefficients of two CFD simulations at an engine speed of 2000 and 4000 RPM depending on the intake valve lift. The black dashed line shows the implemented curve of this coefficient in the WPC of the SCE. Since the coefficient is similar for different engine speeds of a specific engine, one simulation is sufficient for its derivation. The initially strong fluctuations result from the large gradients in the flow when the inlet valve is opened. A stable tumble is formed with a larger valve lift.

The second source of charge motion to be discussed is the DI term, which cannot be neglected, especially with high injection rates with C65F35 and a high displacement of the injector position from the combustion chambers' center. Also, the trend in DI SI-Engines tends to increase injection pressure, leading to higher injection velocities. This has a strong effect on the charge motion. Figure 3.2 illustrates the implementation of the term schematically. The larger the lever arm Δs of the injection vector $\vec{d}_{inj}$ with regard to the center of the tumble $\vec{T}_0$, the stronger the effect on the tumbles rate of change during injec-

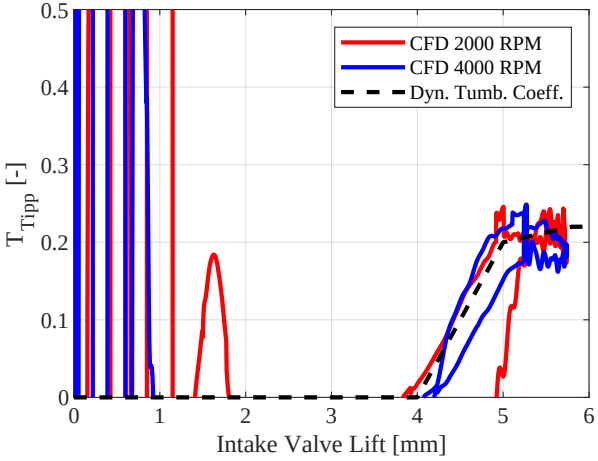

Abbildung 3.1: Calculation of the Tippelmann coefficient from 3D CFD simulations of the SCE and implementation in the 0D1D simulation

tion. As a consequence, the injection can have a strengthening or weakening effect on the tumble.

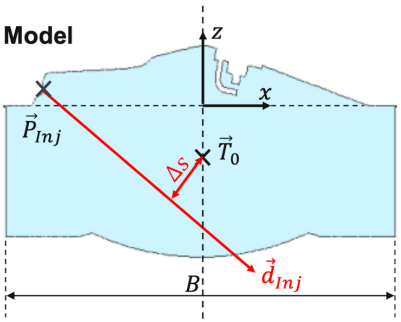

Abbildung 3.2: Schematic illustration of the injection lever arm Δs [61]

Equation (3.3) represents the approach of the injections impact mathematically. The lever arm and injection velocity can be determined with mandatory

injector data such as injector holes, nozzle diameter, injector position, injector direction, and discharge coefficient. In addition, a calibration coefficient $C_{T,DI}$ and the injector mass flow rate $\dot{m}_f$ are needed.

$$\left(\frac{dL_T}{dt}\right)_{DI} = C_{T,DI} \cdot u_{f,eff} \cdot \Delta s \cdot \dot{m}_f \tag{3.3}$$

With the help of these terms, the dimensionless tumble number (3.4) of the 0D/1D simulation in the combustion chamber can be determined and compared with the 3D CFD simulations.

$$Tu_{0D1D} = \frac{L_T}{n_{Engine} \cdot I_T} \tag{3.4}$$

The TKE in the 0D/1D simulation is calculated in a similar way as with the tumble. In addition, there are turbulence production terms due to axial piston movement, compression of the charge air, and squish. As usual with the k-ε model, a dissipation term ε exists and is extended by a direct-injection dissipation term ε_{DI} [61].

$$\begin{aligned}\frac{dk}{dt} = \left(\frac{dk}{dt}\right)_{in} + \left(\frac{dk}{dt}\right)_{Axial} + \left(\frac{dk}{dt}\right)_{Compress.} + \left(\frac{dk}{dt}\right)_{Tumble(Internal)} + \\ \left(\frac{dk}{dt}\right)_{Tumble(Wall)} + \left(\frac{dk}{dt}\right)_{Squish} + \left(\frac{dk}{dt}\right)_{DI} - \varepsilon - \varepsilon_{DI}\end{aligned} \tag{3.5}$$

With these basics, results of the calibrated model for charge motion and turbulence are shown for different scenarios.

Figure 3.3 shows the comparison of the 3D CFD simulation and the calibrated charge motion and turbulence 0D/1D models for an engine cycle. The first two rows are simulations of the SCE, while the last row is a simulation of the 4CE. The influences of engine load, engine speed, and SOI on tumble and TKE are pointed out in the diagrams. It can be observed that the injection (SOI 420 °CA) has a more pronounced role on the tumble at low loads and speeds. While the engine load does not strongly influence the turbulence in these cases, the level of turbulence completely varies for different engine speeds. The SOI sweep has a significant influence on the charge motion. Without the direct injection term in equation (3.1) and (3.5) those effects couldn't be represented. The effect of

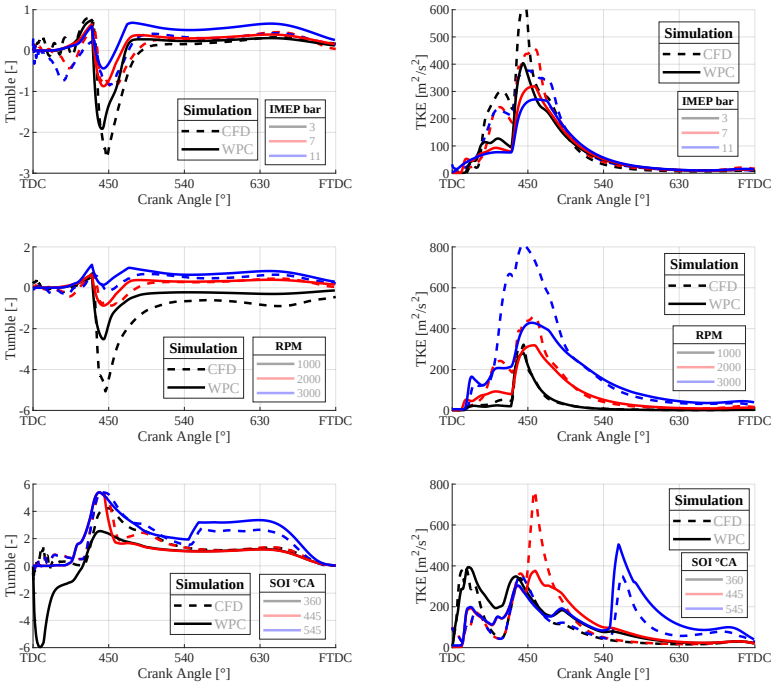

(a) Tumble **(b)** TKE

Abbildung 3.3: Comparison of the Tumbe (a) and TKE (b) for the WPC and CFD simulation. Variation of the engine load SCE (first row), engine speed SCE (second row), and injection timing 4CE (third row)

SOI on turbulence shows the same behavior as for the tumble. The 0D/1D model accurately reproduces the trends of the CFD simulation. The comparison of the TKEs' absolute values is deceptive since they strongly depend on the underlying turbulence model of the 3D CFD. The development of the WPCs' model was carried out with another software and thus with different implementations of the turbulence. This is particularly noticeable for the injection turbulence. Nevertheless, the influences of different engine operating points can be represented, and the charge motion and turbulence model serves as a good basis for the calibration of further models. The next chapter elaborates on the connection between combustion and the turbulence model.

3.3 Burn rate model

One of the most common approaches for modeling the burn rate of SI-Engines is the so-called entrainment model. The idea is to subdivide the combustion chamber into an unburned and a burned zone. Both zones are separated by the flame front, which doesn't count as an additional zone. Grill et. al. [65] present the model in detail. The main goal of the model is to calculate the change of burned mass dm_b stated in equation (2.4). Figure 3.4 shows the modeling approach schematically with the mass flows between the two zones. The entrainment mass m_E of the unburned zone enters the flame front, while converted mass from the flame front enters the burned zone.

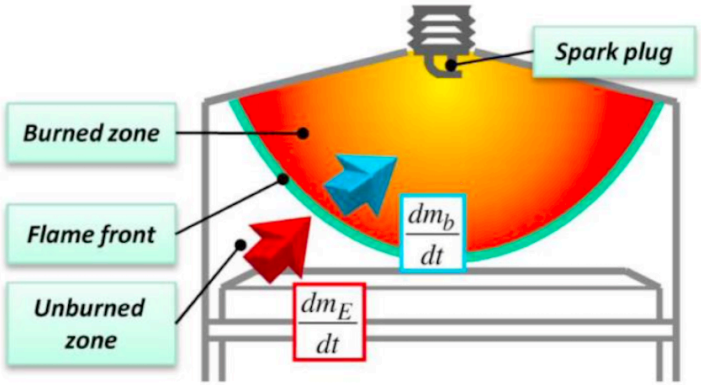

Abbildung 3.4: Schematic illustration of the entrainment model [11]

The mass conversion rate can be expressed with the mass entrained into the flame front m_{fl} and the burn-up time τ_l.

$$\frac{dm_b}{dt} = \frac{m_{fl}}{\tau_l} = \frac{m_E - m_b}{\tau_l} \tag{3.6}$$

In the following, an extended approach of the entrainment model based on [17], [18], and [19] is presented. The equations deviate slightly from the original model and serve to improve the prediction of the burn rate, especially with oxygenate fuels.

Equation (3.6) shows that the conversion of mass entering the flame front is dependent on the burn-up time. This time scale can be calculated as stated in eq. (3.7).

$$\tau_l = a_\tau \cdot \frac{l_{int}}{u_E} \tag{3.7}$$

u_E is the entraining velocity into the flame front area, l_{int} ist the integral length scale and a_τ is a model parameter. The integral length scale is calculated using eq. (3.8), with a_{lint} as model parameter and V_c as the engine cylinders volume.

$$l_{int} = a_{lint} \cdot \left(\frac{6}{\pi} \cdot V_c \right)^{\frac{1}{3}} \tag{3.8}$$

Further, the entrainment velocity can be expressed as:

$$u_E = a_u \cdot s_L \cdot \left(1 + 0.195 \cdot \frac{l_{int}}{\delta_L} \cdot \left(\sqrt{1 + \frac{20.5}{\frac{s_L}{u'} \cdot \frac{l_{int}}{\delta_L}}} - 1 \right) \right) \tag{3.9}$$

Here, the material properties of the fuel mixture are taken into account, which are namely the laminar flame speed s_L and the laminar flame thickness δ_L. A model for the laminar flame speed is discussed in 3.3.1 and compared to calculations based on methods from chapter 2.4. Furthermore, in this equation, the link to the turbulence model can be seen in the form of the turbulent fluctuation velocity u'. The laminar flame thickness in equation (3.10) is fuel dependent due to its kinematic viscosity ν and a parameter $a_{\delta L}$ matched to reaction kinetics simulations. Values of this parameter for the different fuels used in this work are given in the appendix.

$$\delta_L = a_{\delta L} \cdot \frac{\nu}{s_L} \tag{3.10}$$

Finally, with all these variables, the entrainment mass flow dm_E can be calculated using equation (3.11).

$$\frac{dm_E}{dt} = \rho_{ub} \cdot A_{fl} \cdot u_E \tag{3.11}$$

The flame front surface A_{fl} is based on the idea that it propagates ideally hemispherically from the spark plug. For a flat combustion chamber, tables specify the surface area as a function of the ratio of burned to unburned combustion

chamber volume and piston position. These tables can also be adapted to unique piston shapes, making them able to consider accurate combustion chamber geometries. The advantage of this approach is that it saves computational resources.

3.3.1 Laminar flame speed model

From the previous section, it is clear that the accurate prediction of s_L is essential for the prediction of the burn rate. The chemical properties of the fuel have a strong influence on the laminar flame speed in addition to the process conditions pressure, temperature, λ, and EGR rate.

$$s_L = f(fuel, p, T, \lambda, y_{EGR}) \tag{3.12}$$

For the modeling of the laminar flame speed, an approach developed by Müller et. al. [66] is used. In [67], this model was improved and further developed. Hann et. al. [19] have confirmed the quality of the model for different fuels.

$$s_L = A(T^0) \cdot Y_{react}^m \cdot \left(\frac{T_{ub}}{T^0}\right)^r \cdot \left(\frac{T_b - T^0}{T_b - T_{ub}}\right)^n \tag{3.13}$$

The laminar flame speed is calculated with eq. (3.13). The input parameters for the model are T_{ub}, p, λ and Y_{EGR}. $Z_{st}^*, E_i, B_i, m, r, n, F, G, n_{EGR}, n_a c, b_{yH20}$ and d_{yH20} are all model adjustment parameters and are defined depending on the fuel. S_{1-4} are splines that represent the dependency of s_L as a function of λ. The concrete values of the splines and parameters can be found in the appendix. With the help of reaction kinetic simulations, the model parameters are adjusted so that the model outputs s_L with as little error as possible.

$$A(T^0) = F \cdot e^{-\frac{G}{T^0}} \tag{3.14}$$

$$Y_{react}(Z^*, Y_{EGR}) = \left(\frac{Z^*}{1.1 \cdot Z^*}\right)^{n_a} \cdot \left(\frac{1 - Z^*}{1 - 1.1 \cdot Z^*}\right)^{\left(\frac{1}{1.1 \cdot Z_{st}^*} - 1\right) \cdot n_a} \cdot (1 - Y_{EGR})^{\frac{n_{EGR} \cdot d_{yH2O}}{d_{yH2O} + y_{H2O}}} \tag{3.15}$$

$$Z^* = \frac{m_{fuel}}{m_{fuel} + m_{air}} = \frac{1}{1 + \lambda \cdot L_{min}} \tag{3.16}$$

$$T^0 = T_{ub} \cdot S_1(Z^*) + \frac{E_i \cdot S_2(Z^*)}{\ln\left(\frac{B_i}{p}\right)} \tag{3.17}$$

$$T_\mathrm{b} = T_{ub} \cdot (S_4(Z^*) \cdot (1 - Y_{EGR}) + Y_{EGR}) + (1 - Y_{EGR})^c \cdot S_3(Z^*) \tag{3.18}$$

A very detailed explanation of the model is given in [68].

On top of figure 3.5 an overview of the s_L model error compared to reaction kinetics simulation for different pressures and temperatures at λ = 1 is provided. The pressure traces and temperature of two exemplary load points are added to illustrate the engine boundary conditions' ranges. The models' capability at a λ and EGR variation are shown in the bottom area.
It can be clearly seen that the error is well below 10 % for relevant engine boundary conditions in the upper area. Also, the model reproduces an increase of λ and the EGR rate very well. The error increases on the outer edges (10 % EGR / λ = 1.8). Nevertheless, this region is subordinate to the engine application.
With the fuel data available for the equations shown above the burn rate model can be calibrated. This is done with the help of a PTA.

3.3.2 Burn rate model calibration

For the calibration of the burn rate model, it is recommended to adjust parameters a_u and a_τ from equation (3.9). According to [68], a_u compensates for uncertainties in the quantity of u', laminar flame thickness δ_L and the model itself and is in the order of magnitude 3. a_τ is used to adjust the delay of the burn-up time to smooth the burn rate. The calibration of the models is performed at a single load point of the SCE. Thereafter, the calibrated model parameters are kept constant, and no more adjustment to the burn rate model is necessary.

The following validation shows an engine load (load point 1-5) and speed variation (load point 6-9) of the SCE at stoichiometric conditions in figure 3.6. The burn rate of the PTA is compared to the burn rate of the WPC in dependence on the engine crank angle. The model reproduces the PTA derived from the measured data for the load points 1-4 very well. The end phase of the combustion is slightly overestimated at 2000 RPM and 11.3 bar IMEP. A good agreement is given for the engine speed variation (load point 6-9).

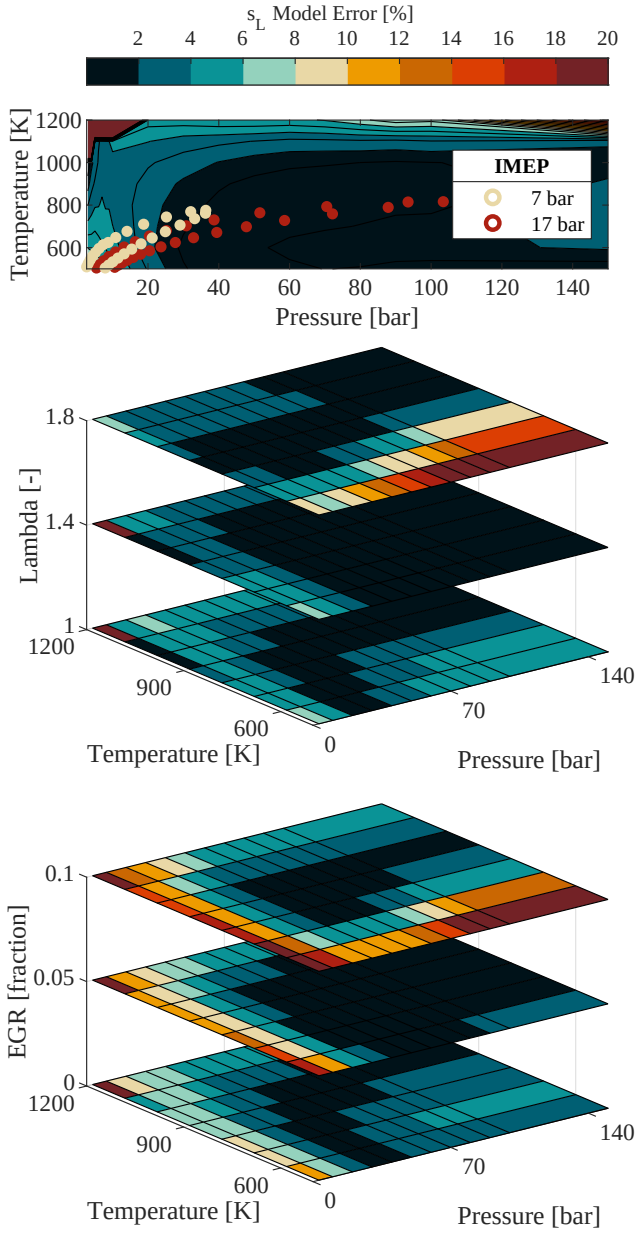

Abbildung 3.5: s_L model error of C65F35 compared to reaction kinetics simulation for different boundary conditions

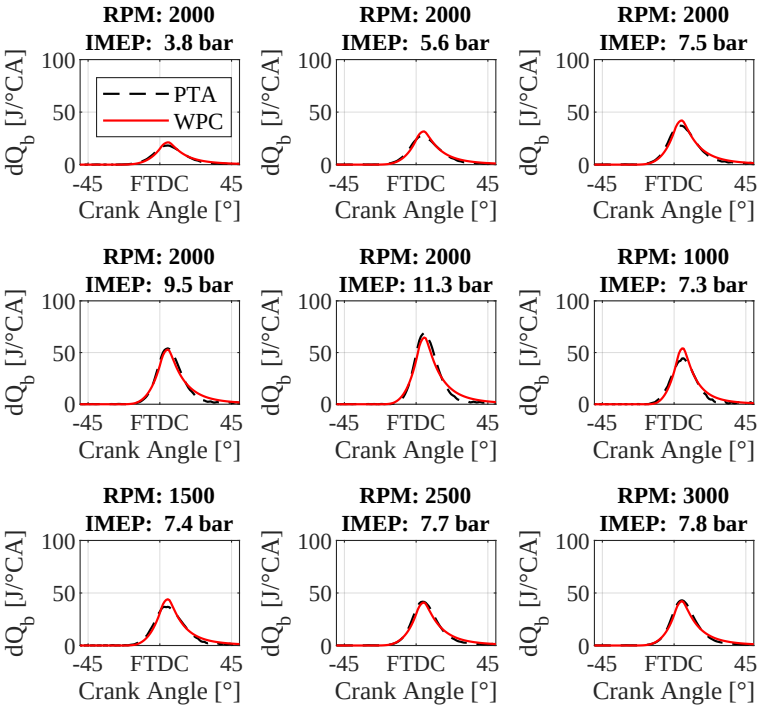

Abbildung 3.6: Comparison of the PTA and WPC burn rate for an engine load and speed variation at $\lambda = 1$ of the SCE for C65F35

This suggests a good interaction with the charge motion model since the turbulence level changes fundamentally.

Figure 3.7 shows a variation of the air-fuel ratio at an IMEP of 7 bar. The range of λ reaches from 0.9 - 1.4. With an increase of λ beyond 1.4, large cycle-to-cycle variations occur in the SCE, which means that the engine can no longer be operated reasonably. Here, too, the trends are well represented. A slight deviation with a higher air-fuel ratio can be observed. As can be seen in figure 3.9, this does not have a major effect on the calculated IMEP. Therefore, the model can also be used for high values of λ.

In the case of the 4CE, load points are examined that are of particular interest

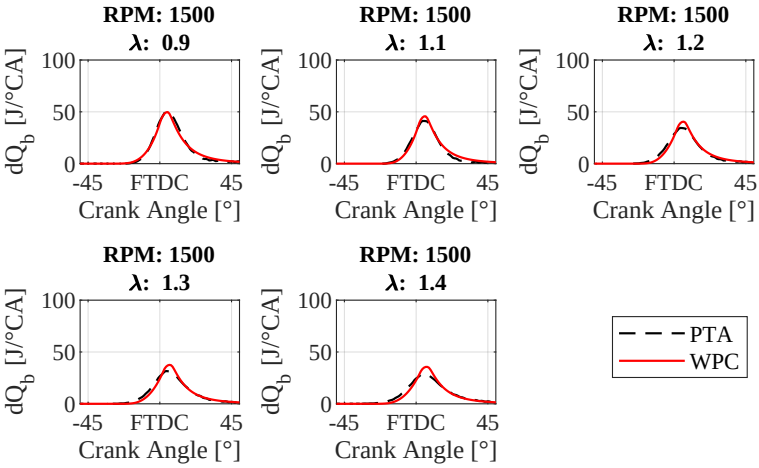

Abbildung 3.7: Comparison of the PTA and WPC burn rate for a λ variation at constant load IMEP = 7 bar for C65F35

for the RDE, including rated power and a low-end torque load point. Figure 3.8 shows the burn rates ordered by increasing load.
Again, the engine load and speed variations match very well. There are minor deviations for the rated power load point due to insufficient indication data (the burn rate increases again in the end phase of combustion). The presented load points above 15 bar IMEP are operated with an open tumble flap, while for the other load points the tumble flap is closed, which also indicates the excellent quality of the charge motion model.
Finally, for the models' validation, the deviation of the WPC IMEP from the measurement data (PTA) is shown. The deviation of the individual load points is less than 5 % for the different variations. Since the validation is based on C65F35, the appendix contains burn rate curves for G85F15 which the model is able to reproduce with similar quality.

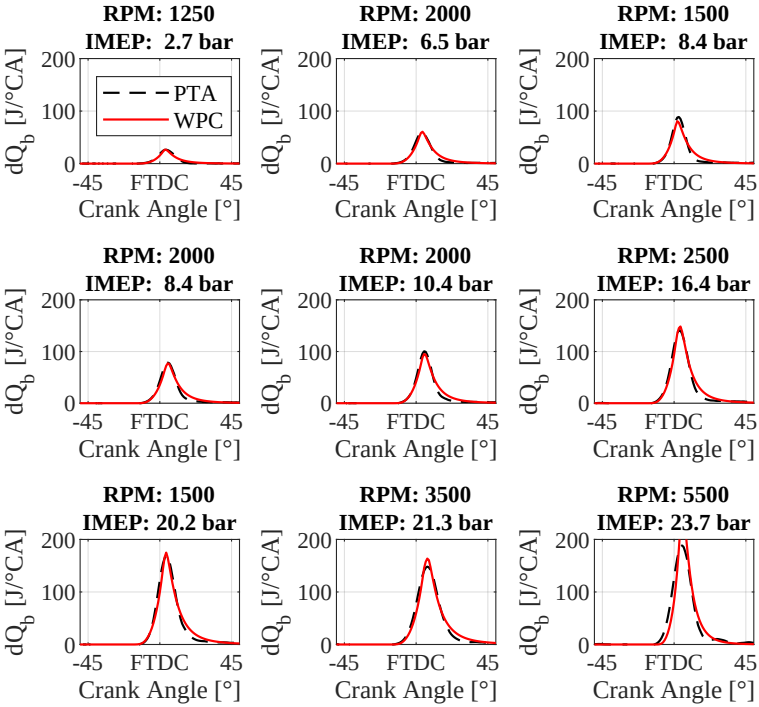

Abbildung 3.8: Comparison of the PTA and WPC burn rate for an engine load and speed variation at $\lambda = 1$ of the 4CE for C65F35

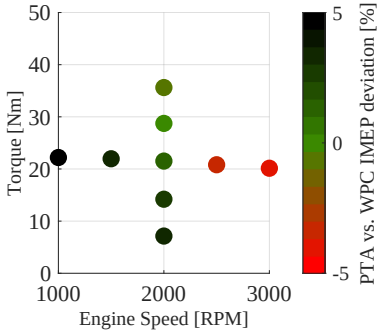

(a) Engine load and RPM variation SCE

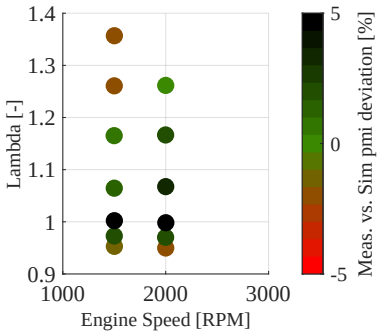

(b) λ variation SCE

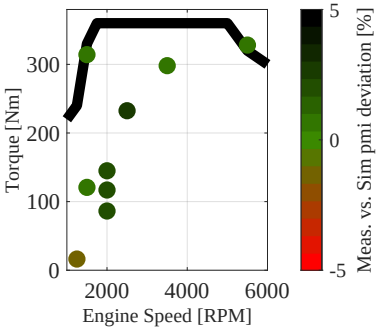

(c) Engine load and RPM variation 4CE

Abbildung 3.9: IMEP deviation of PTA and WPC for C65F35 for different engine parameter variations

3.4 Knock model

The modeling of engine knock takes place in two steps. In the first step, it is determined whether and when auto ignition occurs in the combustion chamber. This is done using the auto ignition model. After that, the knock prediction model is utilized to assess whether this auto ignition can lead to knocking behavior.

3.4.1 Auto ignition model

As discussed in chapter 2.1, C65F35 has no NTC behavior. Therefore, only the modeling of a single-stage ignition will be discussed in the following. Details on the two-stage ignition model can be taken from [69, 70].

The basis of the auto-ignition model is the so-called Livengood-Wu integral I_{ig} stated in [71].

$$I_{ig} = \int_{t_{ig}} \frac{1}{\tau_{ig}} dt \tag{3.19}$$

As the integral reaches the value 1, it is assumed that auto-ignition of the mixture occures. For the modeling of the ignition delay times τ_{ig}, an approach of [72] is used.

$$\frac{1}{\tau_{ig}} = \frac{1}{\tau_1 + \tau_2} + \frac{1}{\tau_3} \tag{3.20}$$

Each ignition delay time τ_{1-3} can be calculated using an Arrhenius equation similar to (2.9).

$$\tau_i = A_1 \cdot \frac{p_{cyl}}{100bar}^{\alpha_1} \cdot \lambda^{\alpha_2} \cdot (1 - x_{EGR})^{\alpha_3} \cdot exp\left(\frac{A_2}{b_{scale} \cdot T_{ub}}\right) \tag{3.21}$$

In equation (3.21) A_{1-2} and α_{1-3} are calibration parameters. The temperature of the unburned zone T_{ub} is a direct input parameter for the model. This temperature can be adjusted using the scaling factor b_{scale}, allowing hotspots in the combustion chamber to be taken into account. This adjustment may be necessary for model calibration. The time step of the integration is 0.1 $^\circ CA$ in the simulation environment.

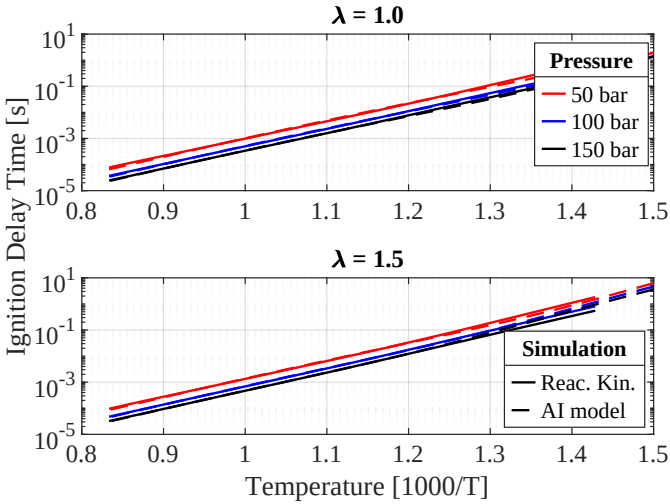

Abbildung 3.10: Ignition delay times of the reaction kinetic simulations compared to the AI model for a variation of temperature, pressure and λ of C65F35

In order to get an overview of the models quality, reaction kinetic simulations are compared with the model results in figure 3.10. It is common to indicate the abscissa with 1000/T (small values correspond to high temperatures) and the ordinate in a logarithmic form since Arrhenius equations are thus represented as straight lines. A pressure variation at two different values for λ is shown. The ignition delay times become shorter with increasing temperature and pressure while they increase with ascending lambda. This behavior is accurately reflected by the model (dashed lines).
In order to be able to compare the models quality with measurement data, single work cycles of the intake temperature variation described in chapter 3.1 are examined. Using the method described in [73], the pressure curve of the measurement is subjected to a Fourier analysis. In this way, it is possible to localize the onset of pressure oscillations. If these oscillations exceed a threshold value, auto ignition can be assumed. The crank angle position at which this pressure oscillation occurs in the measurement data can then be compared

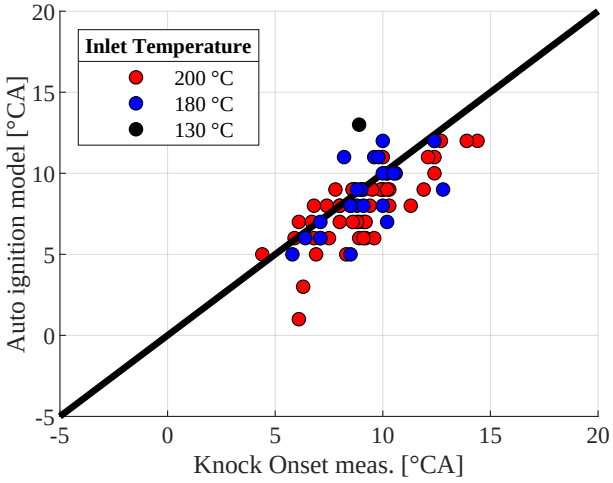

Abbildung 3.11: Knock onset measurement compared to auto ignition model for a variation of inlet temperature of C65F35

with the crank angle at which the Livengood-Wu integral states auto-ignition (=1) in the simulation. This is illustrated in figure 3.11.
Three inlet temperature variations are examined, each with 200 individual work cycles. With increasing temperature, more and more working cycles exceed the threshold value for the pressure oscillation. The bisector of the diagram represents a perfect agreement of the model with the measurement. All the single working cycles are close to it. At this point, it is important to mention that not every auto ignition event automatically leads to engine knocking. In practice, a threshold value for single operating cycles is defined, which is likely to damage the engine if exceeded. At 200 °C, 25 % of the load points already exceed the pressure fluctuation threshold (in this case 1 bar). This is also defined as the knock limit. The knock prediction model can be calibrated further with the calibrated auto-ignition model.

3.4.2 Knock prediction model

The validated ignition delay times serve as input parameters for the knock model. A model developed in [74] is used for this work. This approach evaluates the conditions in the combustion chamber at the time where auto-ignition occurs ($\Pi_{0,AI}$). Also the conditions at the start of combustion, where 2 % mass is burned, is taken into account in particular ($\Pi_{0,start}$). The ratio Π of both values is calculated thereafter.

$$\Pi = \frac{\Pi_{0,AI}}{\Pi_{0,start}} \tag{3.22}$$

$$\Pi_{0,i} = p_{ub} \frac{\rho_{ub} V_{ub}^{1/3}}{\sqrt{\gamma_{ub} R_{ub} T_{ub}}} \tag{3.23}$$

The value calulated in (3.22) is compared to a threshold defined in (3.24). If this value is exceeded, the knock controller retards the combustion center until the criterion $\Pi \leq \Pi_{threshold}$ is satisfied. a_{kn} serves as a model parameter to reproduce the knocking behavior of the engine.

$$\Pi_{threshold} = a_{kn} - a_{kn} \cdot \ln(I_{ig,MFB2}) \tag{3.24}$$

3.4.3 Knock model calibration

To protect the engine from damage, the inlet temperature discussed in the previous section was not raised above 200 °C at the SCE for C65F35. It can be assumed that knocking occurs at 200 °C, allowing the knock model to be calibrated. A further increase in intake temperature or intake pressure should causes the knock controller to retard the center of combustion. For this purpose, simulative inlet temperature and pressure variations are performed for the load point.

Figure 3.12 verifies this behavior. The upper diagram shows the intake temperature variation of the simulation, which causes an increase of MFB50. The same applies to the variation of the intake pressure in the lower area of the figure. The inlet pressure p_{start} is expressed in relation to the pressure at the 200 °C load point $p_{start200C}$. In both diagrams, the measurements of the intake temperature variation (see figure 3.11) of the SCE are marked.

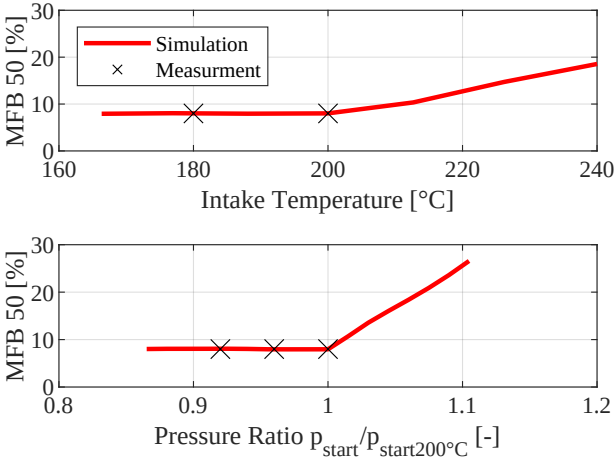

Abbildung 3.12: C65F35 knock model MFB50% forecast compared to measurement data

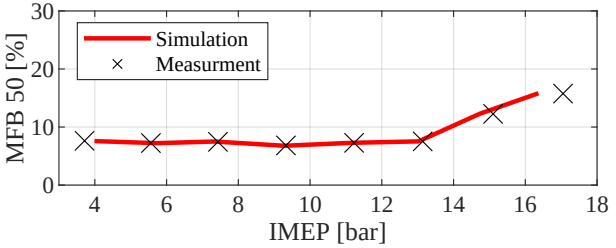

Abbildung 3.13: G85F15 knock model MFB50% forecast compared to measurement data

For the knocking behavior of the gasoline blend fuel G85F15 more measurement data is available at the SCE. The calibration of the knock model is shown as an example using a load variation in figure 3.13. The predicted combustion center of the simulation agrees very well with the measurement data. The ignition delay times of G100 serve as the input variable for the calculation of the knock integral since these do not vary significantly from G85F15 (see figure 2.1).

3.5 NO model

NO_x emissions are calculated using the NO model in the 0D/1D simulation. The chemical species NO_2 is not considered as no sufficiently reliable models are available. For stoichiometric conditions, however, the share of NO_2 of total NO_x production is negligible. The amount of NO_2 becomes more significant with substantial charger dilution, which is not the case for the present work (see [75]). For this reason, only the value for NO will be assessed in the following.

The NO model is linked to the burned zone of the entrainment model described in chapter 3.3. The time-resolved burned temperature and the Air/Fuel ratio of this zone serve as input variables for the model. In [76], it can be seen that the most relevant part of the NOx emissions come from the thermal NO, which can be calculated with the help of the Zeldovich mechanism [77].

$$N_2 + \dot{O} \underset{k_{1b}}{\overset{k_{1f}}{\rightleftharpoons}} NO + N \tag{3.25}$$

$$O_2 + N \underset{k_{2b}}{\overset{k_{2f}}{\rightleftharpoons}} NO + O \tag{3.26}$$

$$N + OH \underset{k_{3b}}{\overset{k_{3f}}{\rightleftharpoons}} NO + H \tag{3.27}$$

NO production is derived from the forward and backward reactions of the above stated chemical reactions, where k represents the strongly temperature-dependent reaction rate constant. This constant can be modeled using an Arrhenius approach (2.9). Therefore, six constants are required for the three chemical reactions. Different values are published in the literature for these constants (e.g. [77]). Since the temperature in the combustion chamber is assumed to be

lower for C65F35 than with G100, a parameter set optimized on reaction kinetic simulations is used, with an additional focus on lower combustion chamber temperatures. Table A.5 in the appendix shows the reaction rate constants used for the simulations. Furthermore, the NO production depends on the concentrations of the individual species coming from the equilibrium calculation (Chapter 2.3).

3.5.1 NO model investigation

In the first step, the influence of the fuels on the NO equilibrium calculation is investigated. For the fuels C65F35, G100, methane (CH4), and hydrogen (H2), different equilibrium compositions are obtained under constant boundary conditions, as shown in figure 3.14. The resulting NO quantity for different pressures and temperatures at $\lambda = 1$ is presented. The lowest NO values are predicted for H2, followed by CH4 and G100, with the highest values for C65F35. This raises the question of whether the newly adjusted Zeldovich constants will reproduce these values and, second, correctly represent the progression of NO formation. It should be mentioned that the equilibrium calculation for NO is only of limited significance, but the process leading to equilibrium is of great relevance.

For this purpose, the individual species of the equilibrium calculation are used as a starting point, and the NO formation is calculated with reaction kinetics simulation. The basis for the reaction kinetic simulation is the GRI3.0 mechanism [12], which is optimized for NO formation. The same is done for the NO model with the Zeldovich approach and fitted reaction rate constants. Figure 3.15 shows the NO formation curves for the different fuels over time. It can be seen that the optimized Zeldovich parameters provide a great agreement with the reaction kinetic simulation for all fuels. The values towards the equilibrium is well captured, and the formation at different timesteps is represented correctly, too.

Two PTAs from the SCE test bench are compared below. Under investigation is one load point (2000 RPM, 9 bar IMEP, and λ =1) with the fuels G100 and C65F35. The left axis of figure 3.16 shows the NO production of the simulation. Significantly more NO is produced for G100 than for C65F35. The reason for this is to be found in the burned temperature of the combustion chamber, which is shown on the right axis. During the compression stroke, the tempe-

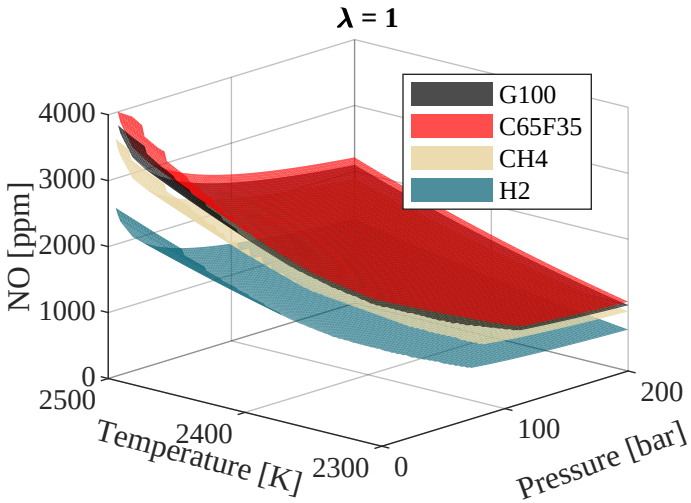

Abbildung 3.14: NO equilibrium calulation for different fuels and boundary conditions at $\lambda = 1$

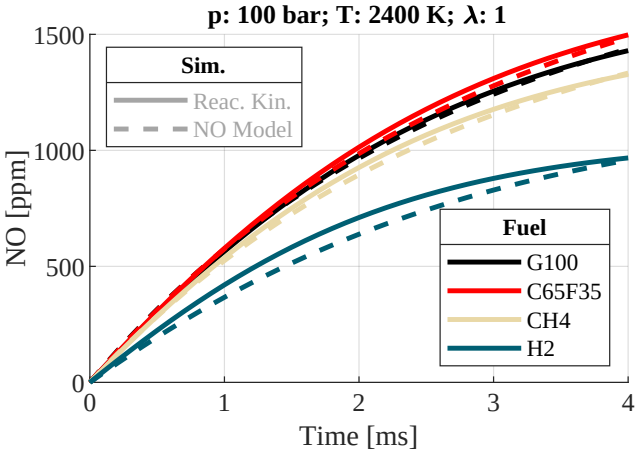

Abbildung 3.15: Comparison of the NO formation time sequence with reaction kinetic simulations (GRI3.0-Mech [12]) and the NO model

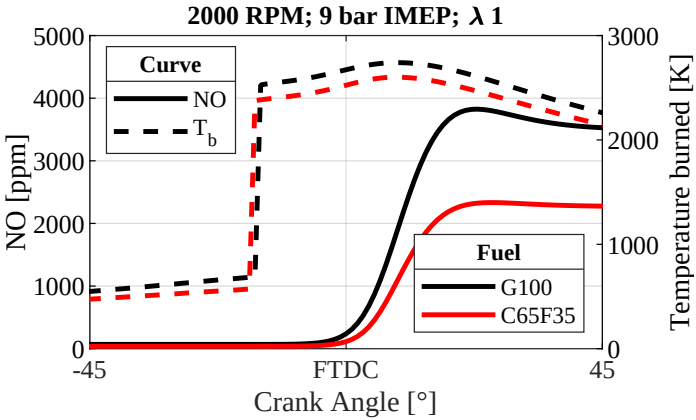

Abbildung 3.16: Comparison of NO production and temperature in the burned zone of PTA for G100 and C65F35 at 2000 RPM 9 bar IMEP and $\lambda = 1$

rature in the combustion chamber is lower for C65F35 than for G100. Due to the cooling effect of the fuel, the temperatures also remain lower during combustion. Despite the higher NO equilibrium values in the previous section for C65F35, this results in significantly lower NO values in the engine process. Another interesting phenomenon of the NO production progression is the only slight back reaction for C65F35. This is significantly higher with G100. However, since back reactions have a strong temperature dependency, this effect is not pronounced for C65F35.

The deviation of the predicted NO values from maesurement data in figure 3.16 is overestimated by about 6 % for G100 . The model quality of the C65F35 load point is shown in the following chapter.

3.5.2 NO model validation

In order to examine the quality of the NO model, simulation results are compared with measurement data from the SCE. Since the reaction rate constants used in the model have already shown good agreement for the NO emission behavior of G100 [78], the investigation is carried out with C65F35. The data is generated for a load sweep and a lambda variation for two different engine

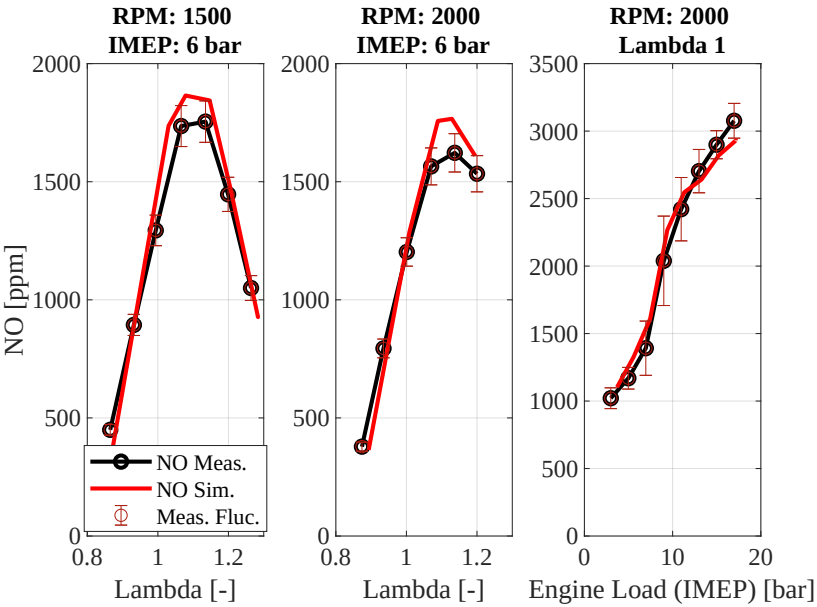

Abbildung 3.17: Simulation of NO compared to measurement data of the C65F35 SCE for a lambda sweeps (left, middle) and a load sweep (right)

speeds. The fluctuation of the measured NO values over 200 averaged operating cycles is marked via an error bar in figure 3.17.
The values of the simulation are based on the PTAs of the measurement data. On the left side of figure 3.17, a lambda sweep at 1500 RPM is shown. The progression of the measurement data can be represented well by the model with a slight overestimation in the range of λ 1.1. The same applies to the middle diagram. The engine speed tendency is well represented. In the diagram on the right, the load variation at stoichiometric conditions also agrees with high quality to the predicted NO values. Of particular interest in the figure on the left is the steep decreasing curve in the direction of higher λ, which causes the NO raw emissions to decrease significantly faster compared to G100 (shown in [52]).

3.6 Additional models needed

So far, only models necessary for calculating the phenomena in the combustion chamber have been discussed. In the following, additional models will be addressed that are required to calculate engine concepts.

The brake efficiency depends on the engine's friction. The **friction model** based on [79] has been further developed in [42] and includes dependencies relating to the compression ratio and cylinder number in accordance with [80]. For the **wall heat model** an approach of [81] is used. The heat transfer coefficient between the cylinder gas and the combustion chamber walls (piston, cylinder head and liner) is modelled. The calculation takes place in two zones. Depending on the combustion progress, a percentage of the combustion chamber area is allocated to the burned area. The remaining surface is assigned to the unburned area. The wall heat flux is divided among the different zones, which corresponds to a more realistic consideration of the the real process. In the simulation software, the **turbocharger model** is represented with the use of characteristic maps. The data for the pressure ratio and the efficiency of the turbine/compressor is given as a function of reduced mass flow and reduced speed. An internal tool at FKFS is used to generate these maps. Based on many real existing turbocharger data, scalable maps can be generated depending on the size of this components. The model also considers friction losses of the turbocharger shaft and the heat transfer from the turbine to the compressor.

3.7 RDE Model

For engines operated in vehicles, both the quantity of substances emitted and the measurement methods for determining emissions are regulated. In addition to measuring emissions on the test bench, the vehicle's behavior in real driving conditions since the introduction of Euro 6 [82] is also examined. Criteria are defined for the procedure of these measurements, which define the vehicles' conditions and the test route. These criteria are taken from [83]. It makes sense to consider emissions and efficiency in the real driving cycle for an engine concept evaluation since this is directly related to fuel consumption. A meaningful assessment of efficiency based on individual load points or a map analysis can deviate significantly from the actual efficiency in real drive operation. For this reason, there are simulation methods that can reproduce the behavior in real

driving operations. These virtual RDE simulations are based on longitudinal 1D models of specific vehicles. The engine must provide the power requirement depending on the route and vehicle conditions. The air resistance, rolling friction of the tires, vehicle weight, altitude difference on the track, gear ratio, and shifting strategy are considered as well.

For the RDE investigation a Passenger car (PC) Mercedes-Benz E-Class model is used. For Heavy-duty (HD) a MAN TGX 18.330 model is used. Table 3.2 presents the boundary conditions and model parameters.

Tabelle 3.2: RDE boundary conditions

Boundary conditions	Paramter	Unit	PC vehicle	HD vehicle
Vehicle Model			Mercedes-Benz E-Class	MAN TGX 18.440
	Total Mass	[kg]	1680	40 000
	Gearbox	[-]	9	12
Engine	Max. Torque	[Nm]	200	2317
	Max. Power	[kW]	96	354
Course			Renningen circuit	Stuttgart - Ulm
	Distance	[km]	92.8	111
	Duration	[min]	102.8	100
	Average Velocity	[km/h]	54.1	66.6

For better comprehension, the speed and elevation profile of the courses are shown in the appendix (see figure A.2). The validation of the simulation mo-

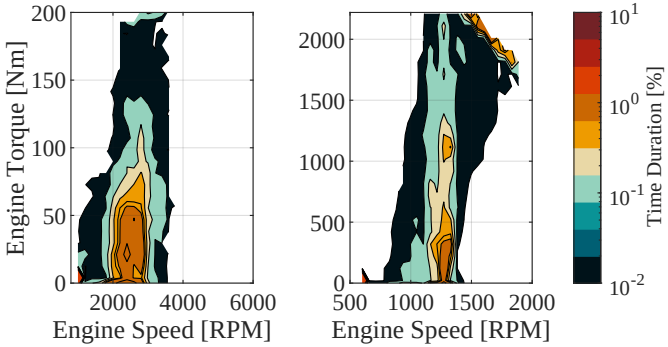

Abbildung 3.18: Engine map time profile visualization of the RDE for a PC (left) and a HD vehicle (right)

dels are carried out by comparing the fuel consumption from the simulation with literature data.
Figure 3.18 shows the time portion of a real drive simulation in the characteristic engine map. From this, it can be derived which load points are of particular significance for the driving cycle. When designing passenger car concepts, one should aim for the highest possible efficiency in the range of low to medium engine speeds at moderate loads. The full-load components play a subordinate role. In the case of truck concepts, a constant speed range is frequently run at different engine loads. This results from the mostly stationary speed during truck operation. It is noticeable that full-load points are passed through more frequently at different engine speeds compared to passenger cars. Therefore, this area also plays a decisive role for truck engine concepts. For reasons of clarity, not all load points addressed in the driving cycle are shown in figure 3.18, but only those with an increased timeshare.

3.8 Preliminary investigations

Two preliminary investigations for the fuel C65F35 are presented in the following. The previously calibrated and validated models serve as the basis for

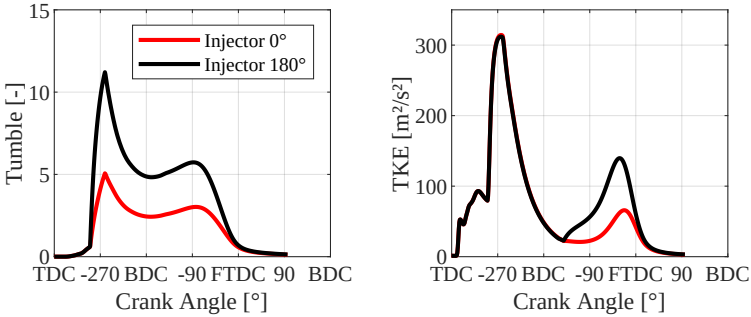

Abbildung 3.19: Tumble (left) and turbulence kinetic energy (right) of a load point with opposit injector positions

this. And on the one hand, the investigations address the effect of low calorific values of C65F35 on the charge motion and the fuels' knock resistance.

3.8.1 Influence of the increased mass flow

The fact that the injection time strongly affects the engine operation with C65F35 fuel is shown in [52]. By retarding the injection timing, CCV could be reduced. The significantly higher impulse energy due to the high mass supplied to the combustion chamber of C65F35 is elaborated with a variation of the injector position. Figure 3.19 shows a simulation where the position of a lateral injector is shifted 180° to the opposite side.
The investigations are carried out at a load point of 2000 RPM and 7 bar IMEP of the SCE. The injector position 0° injects in the direction against the tumble formation while the position 180° assists the tumble build-up. The injection takes place at -290° CA. In this phase, the tumble is built-up by inflow and is supported or inhibited by injection depending on the variant. This leads to a significantly higher charge motion for the variant Injector 180°. Towards TDCF, the tumble drops significantly and ends up at a similar level for both variants. The tumbles' influence on TKE is shown in the figure on the right. The TKE production is similar at the injection event for both positions. However, the following conversion from tumble to TKE leads to different values for the turbulence. This example leads to a higher TKE of 30 % in the area of FTDC

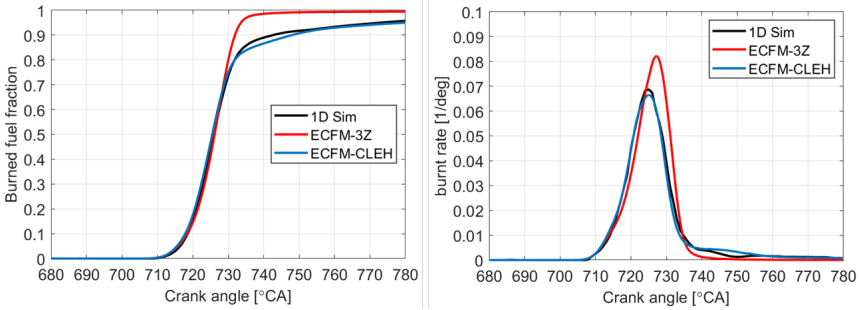

Abbildung 3.20: 3D CFD combustion model calibration (ECFM-3Z ECFM-CLEH) with PTA results of the test bench 4CE [13]

for the Injector 180° variant. The increased TKE reduces the burn duration (φ 10-90) of about 10 %, which increases the efficiency by approx. 1 % relative.

These results are only of limited use for further investigation, as the position strongly affects the results. In order to generate even more reliable results with this model, a variation of the injector position in the combustion chamber of the test-bench would be necessary for model validation. This will not be investigated in this thesis. Since validated data from chapter 3.2 has provided good results, the initial injector position is consequently used for the results presented in chapter 4.

3.8.2 Piston geometry study

To explore the limits of the combustion engine, the compression ratio is increased by changing the piston shape in the 3D CFD simulation. For this purpose, the CFD is adjusted to existing measurements data to forecast the influences of the increased compression ratio in the second step. The following results are based on investigations carried out by [13] as part of the Namosyn project under the supervision of the author.
Figure 3.20 shows the model quality for a load point in comparison to PTA results for different 3D CFD combustion models. The burned fuel fraction is shown on the left side. Especially in the late combustion phase, the ECFM-3Z model deviates clearly from PTA data, while the ECFM-CLEH model shows an almost exact match with test bench data. The burn rate is shown normalized

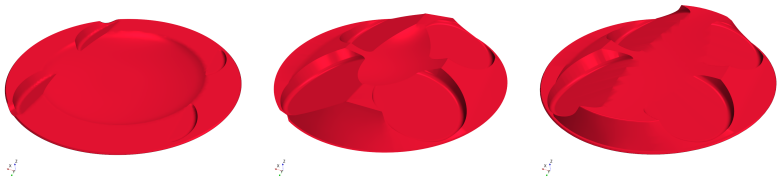

(a) Base **(b)** Variant A **(c)** Variant B

Abbildung 3.21: Piston geometry variation according to [13]

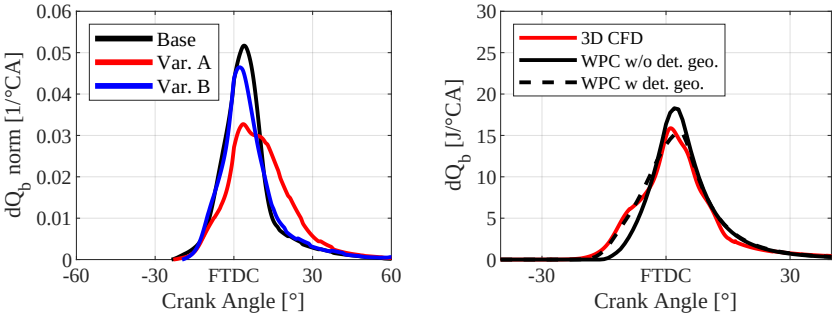

(a) Normalized burn rate 3D CFD **(b)** Burn rate 3D-CFD vs. WPC

Abbildung 3.22: 3D CFD-Simulation based on the piston geometry variation according to [13] (left) and WPC with adapted combustion chamber geometry

to the proportion of the fuel energy provided to the combustion chamber on the right-hand side. The ECFM-CLEH model was used for further investigation.
Figure 3.21 shows the piston geometry study. The original piston was provided with two different piston crowns through which the compression ratio was raised from 9.6 to 14.8. Results of the study are shown in figure 3.22.
On the left side, the normalized burn rate is shown. Variant A has a significantly delayed combustion behavior compared to Variant B. The interaction of the piston shape with the combustion chamber leads to inhibitions of charge motion and flame propagation for Variant A. Due to the modified shape of Variant B, the charge motion and flame propagation are significantly less affected.

The right side of figure 3.22 shows how the WPC responds by adapting the implemented disc-shaped combustion chamber (without detailed geometry) to variant A's geometry (with detailed geometry). The models can reproduce this behavior if the exact geometry is used. It should be mentioned that the use of the detailed geometry affects the flame propagation but has no influence on the charge motion model. Since it is assumed for the studies in the following chapters that the combustion chamber geometry is optimally adapted to the engine concept, the concept studies are made with the standard disc-shaped combustion chamber.

4 Results: Passenger car virtual engine development

The validated models from the previous chapter serve as a basis for the engine concept development of passenger cars. Table 4.1 provides an overview of the models, which are discussed in detail in the individual subsections. The pure synthetic fuel C65F35 and the gasoline blend fuel G85F15 are compared with conventional gasoline fuel as a base variant. The insights are used to develop fuel-specific engine concepts, focusing on cost efficiency and high performance.
The used simulation models regarding laminar flame speed and knock vary between the investigated fuels. While the knock model presented in chapter 3 is used for G85F15 and C65F35, a knock model described in [70] is implemented for the G100 variant.

Tabelle 4.1: Passenger car engine concept overview

Parameter	Reference (Base)	Cost Optimized (CO)	High Efficiency (HE)
Fuel	**G100, G85F15, C65F35**	**G85F15, C65F35**	**G85F15, C65F35**
Displacement volume	1500 ccm	1000 ccm	1000 ccm
Compression ratio	12.5	12, 17	11-19, 16.5-19
Lambda	1	1	1-1.4
Valve timing	variable (Miller)	static	variable (Miller)
Turbocharger	VGT	VGT	VGT + e-Booster
Cylinder deactivation	Yes	No	Yes

4.1 Base concept

A direct-injection gasoline engine VW EA211 TSI evo is used as the baseline engine in the study. It is characterized by high efficiency over a wide range of the characteristic map (see figure 4.1). Decisive factors are the variable-geometry turbocharger, Miller process (opening event 150°CA > 1 mm), a high compression ratio, and cylinder deactivation in part-load [16]. This engine can be arguably seen as state-of-the-art for current gasoline engines in terms of efficiency. The specifications of the virtual test carrier are shown in table 4.2.

Tabelle 4.2: Specification of VW EA211 TSI evo [16]

Parameter	Unit	VW EA211 TSI evo
Max. Power	[kW]	96@5500 RPM
Max. Torque	[Nm]	200
Displacement volume	[cc]	1500
Compression ratio	[-]	12.5
A/F eq. ratio	[-]	1
EGR	[-]	internal

Figure 4.1 shows the engines' brake efficiency as a function of torque and engine speed operated with G100. The modeling was carried out in the FVV project ICE2025+: Ultimate System Efficiency [42]. Measurement data regarding the specific fuel consumption of the engine is provided in [16]. The deviation of the simulation from the measurements in the relevant map area is less than 2 % relative. The engine achieves its peak efficiency of 38.5 % at 3500 RPM and 120 Nm.

The efficiency behavior of the engine differs when the fuel is changed to the gasoline blend fuel G85F15. This is shown in figure 4.2. As the torque increases, the efficiency increases towards the full load area. On the other hand, efficiency decreases in the part-load range. Peak efficiency of 38.2 % is achieved at 3000 RPM and 200 Nm, slightly lower than with G100.

A similar behavior can be observed for C65F35 (figure 4.3). Due to the significantly higher knock resistance, the efficiency is higher over a wide range of the full load curve compared to other variants. At 2500 RPM and 200 Nm, peak efficiency of 38.8 % is achieved. This means that the basic engine variant has the highest efficiency of the fuels compared. However, this high efficiency occurs at different load points in the engine map compared to G100.

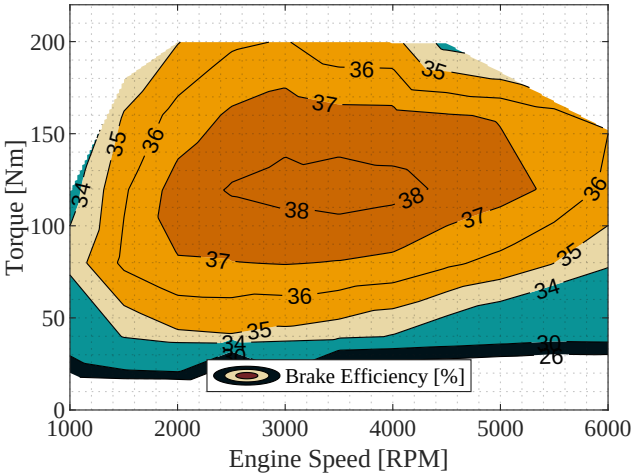

Abbildung 4.1: Simulation of the characteristic map of VW EA211 TSI Evo operated with G100

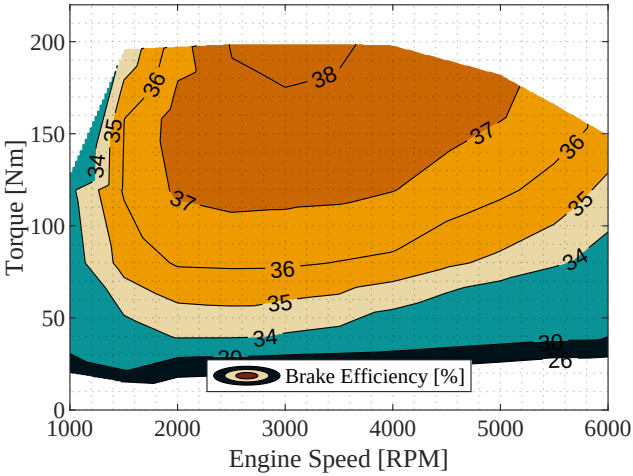

Abbildung 4.2: Simulation of the characteristic map of VW EA211 TSI Evo operated with G85F15

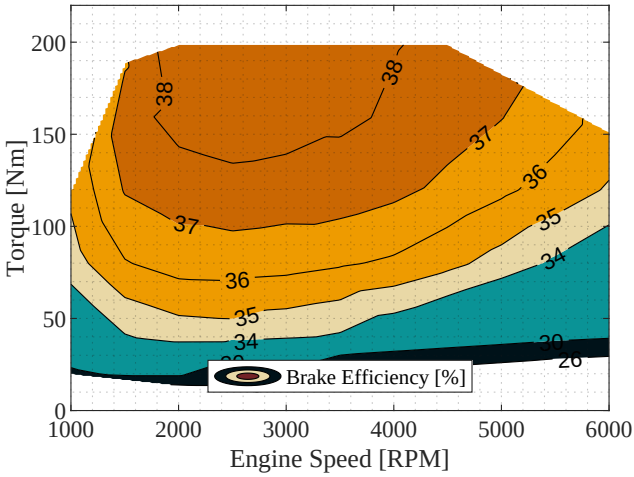

Abbildung 4.3: Simulation of the characteristic map of VW EA211 TSI Evo operated with C65F35

The peak efficiency at a torque of 200 Nm points directly to the potential of efficiency-enhancing measures for G85F15 and C65F35. In order to be able to examine the effects of the fuel in more detail, an energy share distribution is considered in the following. For this purpose, load points are taken into account that are of particular interest for the RDE.

Figure 4.4 shows the distribution of the single engine losses for the load points. These are divided according to table 2.2 in chapter 2.2, with the difference that unburned fuel corresponds to the combustion loss. At moderate loads, the base engine with G100 has advantages in terms of efficiency due to its faster combustion process, resulting in lower exhaust losses (top left and center). The higher throttling of the C65F35 ICE in the part-load range results in high gas exchange losses (center right). This is due to the 14 % higher mixture heating value of C65F35 compared to G100 fuel (see chapter 2.1). The fuels less prone to knock show an increasing efficiency compared to G100 at high loads due to advantageous locations of combustion center (top right and bottom left).

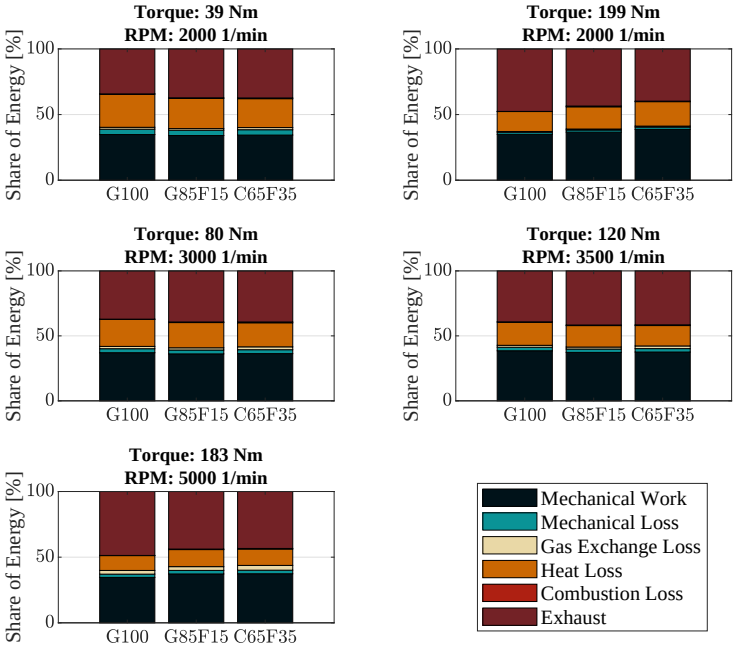

Abbildung 4.4: Share of energy of different load points in the base enignes' characteristic map for different fuels

It can be concluded that G85F15 and C65F35 variants are well suited for downsizing concepts. The components are scaled according to the downsizing degree for the following engine models. This ensures that the engine periphery matches the displacement volume, including valve lift and diameter, turbocharger, pipings, and exhaust after-treatment system. Since there is little data available to validate the knock model for C65F35, a peak pressure limitation of 180 bar in the combustion chamber is set. This extreme cylinder pressure has already been tested in the low-end-torque area on the test bench and is free of knock behavior.

4.2 G85F15 dedicated engine concepts

To make a fair comparison of the different engine concepts, all of the following concepts will have the same performance data as the base engine.

4.2.1 Cost-optimized concept

Figure 4.2 showed the highest efficiency in the full load area. Therefore, a downsizing is carried out for the cost-optimized engine. The displacement volume is reduced by 500 ccm to 1000 ccm. At the same time, technologies that make the propulsion system more complex are omitted. This applies to the cylinder deactivation and the variable valve train.

The compression ratio is reduced to operate the engine over wide ranges in the characteristic map with an optimum center of combustion. It is necessary to sacrifice torque in the low-end torque area because the turbocharger does not have enough exhaust gas enthalpy to increase pressure, despite the late center of combustion (20° CA) due to knock avoidance. Further retardation of the combustion center can remedy this, but at significant efficiency costs. 200 Nm torque is reached from 2000 RPM onwards. This results in the characteristic map of the engine is shown in figure 4.5.
The area with the best efficiency moves towards the center and is more extended compared to figure 4.2. The static valve train leads to a tradeoff, resulting in a slightly lower peak efficiency. Due to the knock controller, the center of combustion shifts toward 20 ° CA @ 2000 / 18 ° CA @ 3000 RPM in the full-load range.

Nevertheless, a comparison with figure 4.1 shows that a similar level of efficiency can be maintained with significantly less complexity.

4.2.2 High-efficiency hybridized concept

For the high-efficiency engine, all available technologies are used to achieve the highest possible efficiency. That includes a lean operating strategy, variable compression ratio, variable valve train, and cylinder deactivation. Due to the low exhaust gas enthalpy offered by the substantial downsizing in the low-end torque area, it is necessary to support the exhaust gas turbocharger with

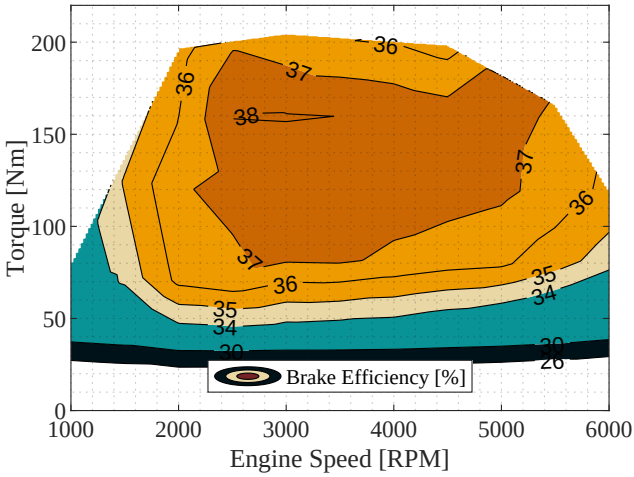

Abbildung 4.5: Characteristic map of the G85F15 cost-optimized engine

the assistance of an e-turbo. In the FVV-Project ICE2025+ ([42]), it was determined that measures such as optimized diffuser geometry, bearing resistance reduction, and advanced manufacturing processes will lead to efficiency improvements in turbochargers in the coming years. A relative increase of 11 % is therefore assumed for the compressor, and 14 % for the turbine following [42].

Stoichiometric operation is applied over a wide range of the characteristic map. This is advantageous for the turbocharger, which reaches its performance limit at a higher air-fuel equivalence ratio (λ) at high loads. This, too, prevents the e-turbo from operating in large parts of the engine map, thus negatively impacting the engine concept's efficiency. An air-fuel equivalence ratio of 1.4 is used in the low load range to benefit from the de-throttling of the engine. A disadvantage for the lean condition at λ 1.4 is that the engine becomes prone to knocking at higher loads (see. [84]), leading to a limited range where lean operation can be applied. The operating strategy is shown in figure 4.6 (top, left). A lean operation strategy is used up to 60 Nm, and thereafter a stoichiometric one. The power output map for the e-turbo is presented at the bottom left. This component assists the turbocharger in the area of the low-end torque with

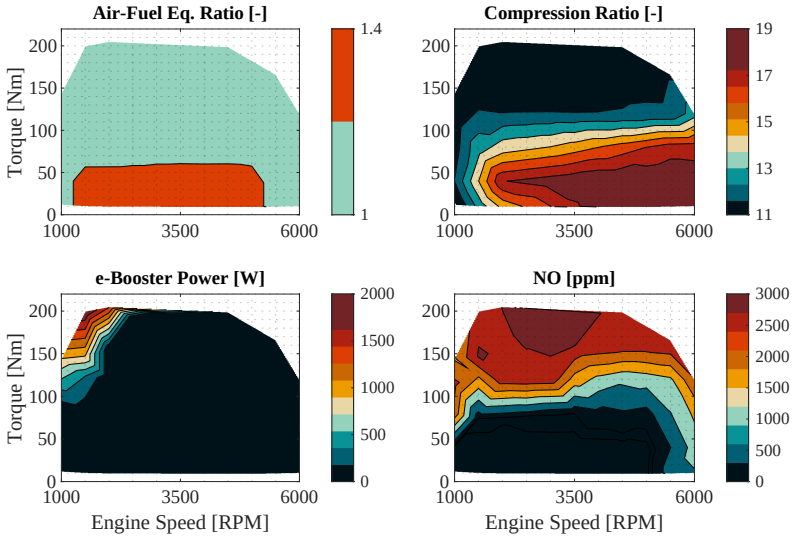

Abbildung 4.6: Maps of the G85F15 high efficiency engine for A/F eq. ratio (top,left), Compression ratio (top, right), e-turbo power (bottom,left) and NO emissions (bottom, right)

around 2000 W (1500 RPM 200 Nm) propulsion power for the turbomachines shaft. The variable compression ratio is displayed at the top right. At low loads and moderate to high engine speeds, a compression ratio of 19 is applied. A higher compression ratio would be conceivable, but due to geometry limitations, the compression volume gets too small and leaves no space for the spark plug if a flat piston is maintained. At high loads, the compression ratio is successively reduced to 11 due to the increasing knock tendency. At low speed, a high compression ratio impairs brake efficiency. A significantly increased frictional power causes this at high compression ratios. The NO emission behavior is shown at the bottom right. In lean operation, the NO concentration is below 50 ppm. With increasing load and stoichiometric operation, the NO emissions increase strongly. The current exhaust gas legislation may be complied with an LNT and 3-way catalytic converter.
Figure 4.7 shows the efficiency of the engine concept. Due to the variable compression ratio, the center of combustion can mostly be kept at an optimal level at around 8° CA. Compared to figure 4.2 where the optimum is reached at full

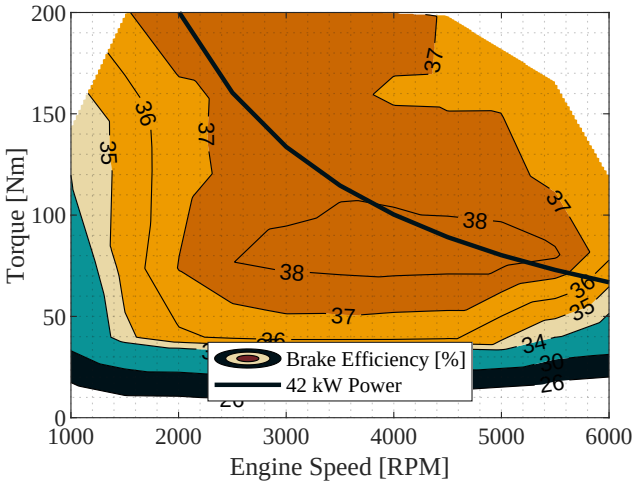

Abbildung 4.7: Characteristic map of the G85F15 high-efficiency engine with the power demand of an range extender concept

load, the optimum efficiency is achieved in the partial load range. The range with high efficiency is significantly extended (peak brake efficiency of 38.6 % at 4000 RPM and 80 Nm). In addition, the lower partial load range is improved by additional technologies, which provides clear advantages to the real driving cycle.

Range extender concept

For the design of a range extender concept, data from [85] and [86] are used. According to the sources, a range extender power of 41.5 - 43.1 kW is required for a vehicle weight between 1500 - 1700 kg. The area with the highest efficiency in the engine map of the high-efficiency concept is investigated at 42 kW power (see figure 4.7). Due to the significantly higher complexity of the exhaust gas after-treatment in the lean operating range, the system is particularly suitable for load points above 80 Nm torque (stoichiometric operation). This allows the exhaust gas after-treatment to operate via a conventional 3-way catalytic converter. The efficiency at 4000 RPM is 38.4 %.

4.3 C65F35 dedicated engine concepts

After G85F15 has shown clear advantages in terms of efficiency in vast areas of the engine characteristic map, the pure synthetic fuel C65F35 is now being discussed for various engine concepts. The following concepts will also have the same performance data as the reference engine.

4.3.1 Cost-optimized concept

The model for the cost-optimized engine of C65F35 is similar to the model in chapter 4.2.1 (see also 4.1). Due to the high knock resistence of C65F35, the compression ratio can be increased significantly to a value of 17. Again, there are drawbacks in the characteristic map (figure 4.8) at low engine speeds concerning the peak torque. The exhaust gas enthalpy does not suffice to build up the charging pressure since it is possible to operate with an optimum center of combustion in the low-end area. This increases the efficiency but reduces the exhaust gas enthalpy available for the turbocharger. This problem could be counteracted by retarding the combustion. However, this is not done for a better comparison with the G85F15 engine concept, where the combustion center is already at 20°CA after TDC. The best efficiency for the C65F35 concept is at 3500 RPM and has a value of 41.1 %. This results in a peak pressure of 177 bar at a BMEP of 25 bar. The area of high efficiency extends over large parts of the full-load region down to the partial-load area.

4.3.2 High-efficiency hybridized concept

A lean concept in a wide range of the engine map is used for the high-efficiency concept, including the area of mid torque levels and a vast high torque area (see figure 4.9 top, left). According to [52] the NO production at λ 1.4 of C65F35 is at a similar level as G100 with λ 1.6, resulting in less mixture dilution due to emission reduction. The investigation was carried out at a constant load point. This offers potential for exhaust gas after-treatment even at λ 1.4, an area avoided when using G100 due to considerable NO emissions. The reduced air-fuel equivalence ratio has a favorable effect on the turbocharger, which needs to provide a lower boost pressure. Nevertheless, the limiting range of the characteristic map for a λ value of 1.4 is determined by the turbocharger.

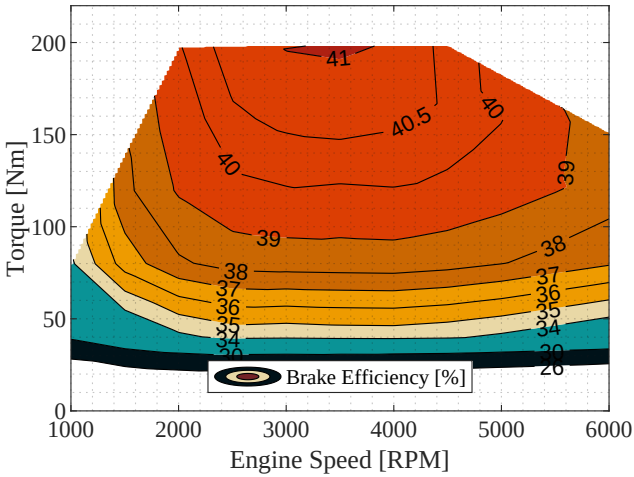

Abbildung 4.8: Characteristic map of the C65F35 cost optimized engine

The mass flow rate at rated power is too high for the turbomachines design resulting in a stoichiometric operation in this area.

At the top right of figure 4.9, the compression ratio is shown. The behavior is similar to the G85F15 engine concept with a significantly higher compression ratio (CR = 16.5) at high loads. It would also be possible to use higher compression ratios in this area since the center of combustion is optimal in large areas. However, due to the limited peak pressure in the combustion chamber, the compression rate is not increased any further. Compared to the cost-optimized concept, the compression ratio is reduced by 0.5 units in the high torque area to account for the lean mixture operation. In Figure 4.9 (bottom left) it can be seen that the support from the e-turbo is similar to the G85F15 variant despite the higher air-fuel equivalence ratio. This shows the effect of lower air requirement of C65F15.

The NO emission map is presented at the bottom right. In the blue area, the raw NO emissions are below 200 ppm and rise to approx. 300 ppm in the low-end torque area. In stoichiometric operation at rated power, emissions become significantly higher.
The effects of the changed process parameters can be seen directly in figure

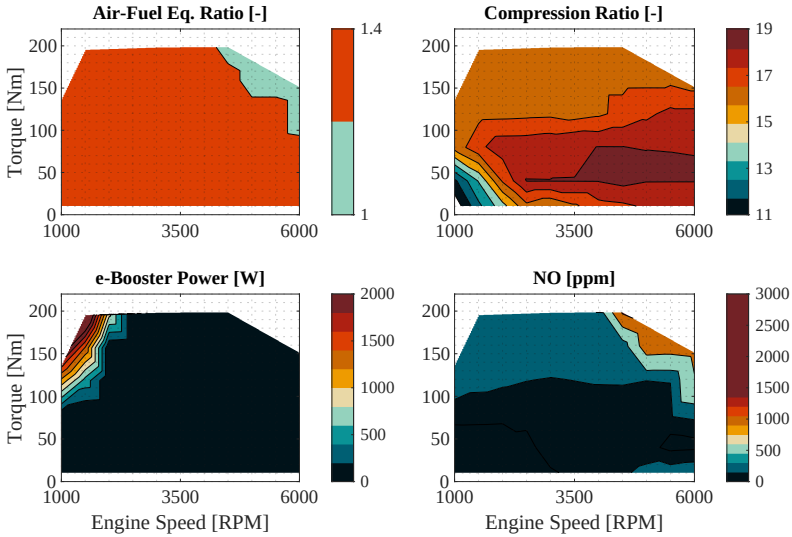

Abbildung 4.9: Maps of the C65F35 high efficiency engine for A/F eq. ratio (top, left), Compression ratio (top, right), e-turbo power (bottom, left) and NO emis- sions (bottom, right)

4.10. A peak efficiency of 42.8 % is achieved in the lean area at 3500 RPM and 160 Nm. A potential C65F35 range extender concept results in an efficiency of 42.2 % at 2500 RPM.

Short study: Influence of an active pre-chamber spark plug

The higher burn duration due to lower laminar flame speed and lower process temperatures of C65F35 can be counteracted by using active pre-chamber spark plugs (PC). The combustion model is adapted to represent this reduced burn duration in a simple approach. For this purpose, the burn rate model parameter a_u discussed in chapter 3.3 is increased. This corresponds to the recommendation of [68], where this value is increased by at least 50 % in case of active pre-chambers for a good agreement with measurement data (54 % in the following example). This study is performed only for C65F35 since it is assumed that the effects for G85F15 behave similarly concerning combustion duration.

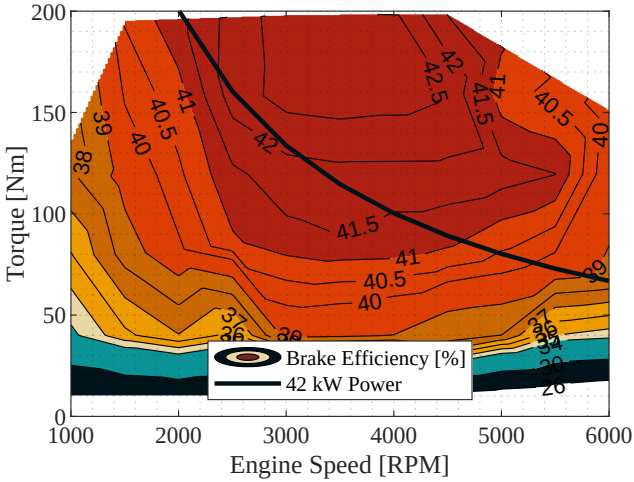

Abbildung 4.10: Characteristic map of the C65F35 high-efficiency engine with power demand of a range extender concept

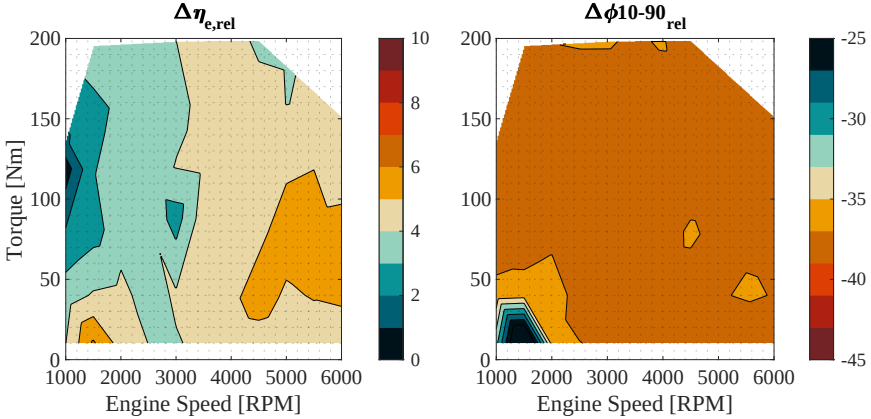

Abbildung 4.11: Characteristic map of the relative difference in brake efficiency (left) and combustion duration (right) for the C65F35 high efficiency engine with and without PC

Figure 4.11 shows the increased brake efficiency by up to 6 % relative at high engine speeds and moderate load. The average efficiency gain over the characteristic map is approx. 4 % relative. On the right side, it can be seen that the average burn duration (φ_{10-90}) is reduced by roughly 37 %. The burn duration refers to the period in which 10 % up to 90 % of the fuel mass is converted.

4.4 Evaluation of engine concepts in the RDE-Cycle

In the following, the engine concepts presented above are evaluated in the real driving cycle according to chapter 3.7. Figure 4.12 shows the RDE effective efficiency on the left axis and the raw NO RDE emissions in mg/km on the right axis for the different fuels and engine concepts. In the RDE cycle, the G100 fuel performs best for the base engine concept (approx. 34 % effective efficiency). This is due to the lower throttle losses and faster combustion duration (figure 4.4), especially at a high part-load timeshare. Nevertheless, it can be seen that the amount of NO predicted in the RDE becomes significantly lower with G85F15 and C65F35. For the latter fuel, reduction can be quantified at 60 %.

In the case of cost-optimized engine concepts (CO), an efficiency advantage for C65F35 can already be achieved with downsizing, despite the lack of technologies to increase efficiency (cylinder deactivation, variable valve train) compared to the G100 base variant. The lower load on the single cylinders explain the advantage in terms of NO due to the lack of cylinder deactivation. The efficiency level for G85F15 can be maintained with the CO concept compared to its base variant. For the high-efficiency concepts (HE), efficiency increases significantly (37.3 % for C65F35). The effect of lean combustion can be seen in NO emissions, which causes a more substantial reduction for C65F35 than for G85F15. The NO raw emissions in the RDE simulation for C65F35 are 550 mg/km, correlating to the level of Diesel passenger cars in this segment. The limit value for NOx is 60 mg/km [82], which leads to a reduction requirement of approx. 89 %. Exhaust gas after-treatment concepts (NOx storage catalyst and SCR system) make it possible to keep emissions well below the Euro 6 limit (see [87]).
For the pre-chamber spark-plug engine concept, an effective efficiency of over 39 % can be achieved in the virtual driving cycle.

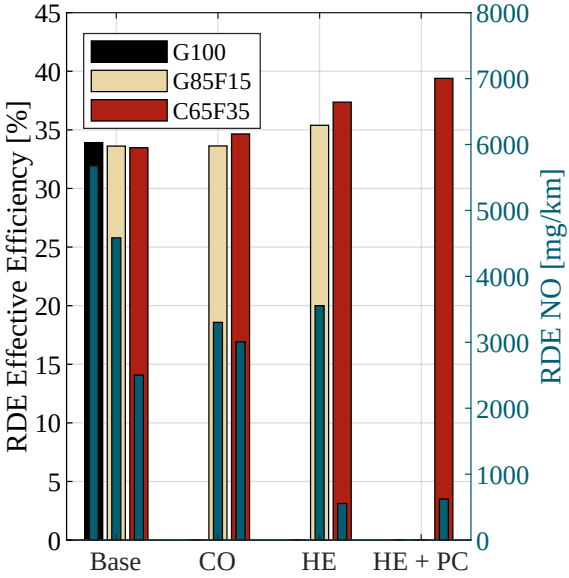

Abbildung 4.12: Effective efficiency of investigated engine concepts in the RDE with associated NO emissions

Before discussing the reliability of the results in the next chapter, the fuel consumption of the engine concepts is shown in figure 4.13. As the oxygenate content in the fuel increases, fuel consumption rises. Due to the lower heating value, a significantly larger amount of fuel is converted in the vehicle. For the base variant, the fuel consumption in liters/100km is about twice as high for C65F35 compared to G100. For the G85F15 variants the additional consumption of the CO concept is less than 1 % relative, while the HP concept saves 0.3 liters/100km of fuel compared to the base. Fuel consumption of the C65F15 is steadily decreasing with the studied concepts starting from the base. By applying the complete package of measures (HE + PC), fuel savings of up to 2 liters/100km can be achieved for C65F35 compared to its base.

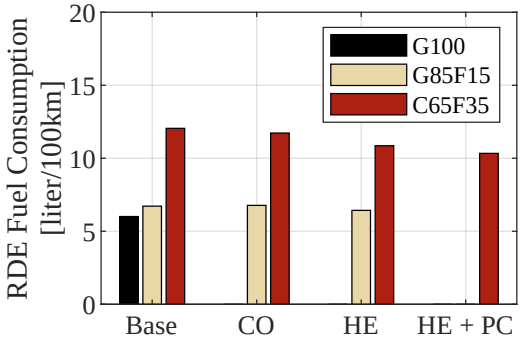

Abbildung 4.13: Total fuel consumption of investigated engine concepts in the RDE

4.5 Discussion

Five key statements can be taken from this chapter:

- Today's state of the art engines perfectly match with the properties of conventional fossil fuel
- By only exchanging the fuel in the existing engine concept, disadvantages will occure concerning fuel consumption in the RDE driving cycle
- The fuel itself is a powerful lever for increasing efficiency and reducing emissions
- The fuel can compensate for cost-driven technologies
- Significant increases in efficiency can be achieved with vehicle concepts optimized for tailor-made fuels

In the following the validity of these statements based on the presented results will be discussed. While the initial model is based directly on publications of measurement data from the engine, it can be assumed that the model behavior correctly represents the physical processes of G100. Studies of the models behavior used in this thesis with different fuels are discussed in [68]. The influence on the engine's combustion process can be represented for different fuels accurately. The excellent agreement of the reaction kinetics simulation of the

specific fuels with the models (see chapter 3) assures that the behavior of the base engine simulation can be reproduced very well. Since the models are adjusted to single-cylinder test bench data with different fuels, this continues to lead to reliable results.

The investigated cost-efficient concepts avoid technology that does not need to be modeled, making the system more straightforward. For G85F15, the question of the accuracy of the knocking model remains open. A minimal error is expected in modeling the ignition delay times since the behavior is similar to gasoline. The knock model developed in [74] is based on conventional gasoline. Validation with different fuels is still required. Nevertheless, as discussed in chapter 3, the available measurement data is correctly represented by the simulation. This also applies to C65F35. While the model is validated for ignition delay times, there is very little measured data for knock behavior. However, due to the pressure limitation in the combustion chamber, it can be assumed that engine knock plays a subordinate role in the engine concept, as indicated based on measurements. The extreme compression ratio, however, is an open issue. In the preliminary study in chapter 3.8.2, the influence of piston geometry on combustion behavior is shown. It has been stated that the piston geometry investigated is only suitable to a limited extent for a substantial increase in compression ratio. Nevertheless, the results from the preliminary study are not directly transferable since it is assumed that future engine concepts will include a highly adapted combustion chamber geometry for high compression concepts, as it is the case with Diesel engines.

For the high-efficiency concepts, the same applies as described above. The turbulence increase in the combustion chamber with the use of an active pre-chamber spark plug was discussed in the previous chapter. In the context of this work, no measurements of high-turbulence concepts or active pre-chamber spark plugs were available. This technology can reduce burn duration by up to 1.5 times as shown in [43] (see 2.2.2). In the approach used, 1.4-fold burn durations are predicted. This shows that there is still great potential in the efficiency of engine concepts that have not been exploited. It should be pointed out that the engine concepts strongly depend on the combustion duration which is responisble for two factors: Firstly, the isochoric part of the engine process increases significantly due to fast combustion, leading to increased efficiency. Secondly, the fast combustion process makes the engine less prone to knock since auto-ignition starts when most of the mixture has already been conver-

ted. This would result in a high potential for the fuel G85F15 with an active pre-chamber spark plug, which was not considered in this work. However, it is expected that no comparable knock resistance to C65F35 will be achieved. With the less favorable air demand compared to C65F35, this should result in lower overall efficiency for G85F15.

The validation of the RDE simulation is performed using driving reports. Since the investigated engine concept and the longitudinal dynamics model are derived from the portfolio of different manufacturers, the validation can be carried out rudimentarily. Driving reports from [88] state a fuel consumption of 5.1 liters/100km for a vehicle operated with the engine used in the simulation for G100. The vehicle model used in the simulation is 300 kg heavier than the vehicle examined in the driving report. Assuming 0.3 liters of additional consumption per 100 kg vehicle mass [89], the results fit very well with the simple modeling approach (6 liters/100km for the G100 base engine variant in the RDE simulation).

The dynamic gain of e-turbos is not investigated in this thesis. Since this is one of the key functional principles of this technology, the exact impact on the vehicle engine system is not considered. This also raises the question of the dynamic behavior of the engine concepts, which can be the subject of future investigations. The simplified approach that the energy output of the e-turbo is compensated by recuperation is difficult to prove with the steady-state approach used here and can therefore also be the subject of further investigations.

The last point to be addressed is the reliability of the emissions calculated. In [52] the NO emissions of C65F35 are compared to G100. It is shown that in stoichiometric part-load operation, the NO production for G100 is three times higher compared to C65F35. The simulation reflects this behavior. The models have also shown excellent predictive ability with charge dilution. The validation of NO emissions is only performed up to λ 1.3 as the engine conditions were changed for measurements of higher dilution. The course of NO emissions over lambda is very steep in this area, leading to uncertainties in the model prediction. Further test bench and RDE measurements with lean combustion can confirm the simulation results.

5 Results: Heavy-duty trucks virtual engine development

The truck and bus sector accounts for 27 % of road transport emissions in the European Union [28]. Most of these vehicles currently operate on Diesel fuel. The Soot-NO_x problem of the propulsion system is typical in this case. To reduce pollutant emissions with simultaneous CO_2 savings, more and more focus is being shifted to natural gas-based concepts. In the future, H_2-powered vehicles will also be developed, which are not yet available on a series production scale. These concepts can then be operated locally in a CO_2-neutral way. Since the storage technology for hydrogen is very complex, an alternative liquid synthetic fuel can also offer advantages in this context. This can improve energy efficiency and range restrictions. A comparison of virtual engine concepts operated with different fuels is carried out to answer this question. In this context, well-known engine concepts with natural gas (CH4) and Diesel fuel serve as benchmarks for future engine concepts. A C65F35 engine concept based on the natural gas engine is introduced. This concept will then be optimized to take advantage of the fuel properties. Since hydrogen combustion in the ICE is becoming more and more popular in heavy-duty trucks, an H_2-concept will be presented. Table 5.1 shows the boundary conditions for the engine models presented below.

Tabelle 5.1: Heavy-duty engine boundary conditions

Parameter	Unit	Value
Max. Power	[kW]	353@1800 RPM
Max. Torque	[Nm]	2300
Displacement volume	[l]	12.5
Cylinder	[-]	6
EGR	[-]	external

The evaluation of the propulsion concepts is based on characteristic engine maps and is also assessed in the context of a real driving cycle, analogous to chapter 4. The vehicle model and route described in chapter 3.7 are used for this procedure.

5.1 Engine models

Table 5.2 provides an overview of the engine concepts, which are discussed in detail in the individual subsections. As shown in figure 3.18, a significant part of the engine operation occurs in the full load range for heavy-duty vehicles. Fuels that are prone to knock suffer substantial losses in efficiency in this area. For this reason, the gasoline blend fuel G85F15 is not considered. Based on the findings of the previous chapter, it is also assumed that engines operated with C65F35 perform significantly better in efficiency than G85F15.

5.1.1 Diesel engine

A heavy-duty truck Diesel engine flow model, including exhaust gas after-treatment, is already existing for this work. The model based on a MAN D2676 engine was developed in a research project funded by the BMWi [95]. The dimensions and specifications of the engine and exhaust gas after-treatment are determined from literature (see [90], [91], [92] and [93]) and comply with the Euro-6 exhaust gas standard. A compression ratio of 17.5 and a displacement volume of 12.5 liters are used. The engine has a wastegate-controlled two-stage

Tabelle 5.2: Heavy Duty engine concept overview

Parameter	Reference Engines		New Concepts		
Fuel	**Diesel**	**CH4**	**C65F35**	**C65F35**	**H2**
Displacement volume	12.5 l	12.5 l	12.5 l	11.5 l	12.5 l
Compression ratio	17.5	12.5	12.5	14	12
Lambda	1.2-5.5	1	1	1	1-4
Turbocharger	2x wastegate + charge air intercooler		1x wastegate + charge air intercooler		

turbocharger, making it possible to run the engine with a high percentage of EGR (25 %) even at higher AFR. In addition, a cooling system is implemented in the model for the EGR and the charge air. Exhaust gas after-treatment includes Diesel oxidation catalyst (DOC), Diesel particulate filters (DPF) and Selective catalytic reduction (SCR) in the model. Since this engine serves as a reference model for comparison with other models, the specific modeling of Diesel engine combustion will not be discussed here. Details on the modeling can be found in [94]. The brake efficiency map of the diesel engine is shown in figure 5.1.

The peak brake efficiency of the engine model is 44.2 % at 2200 Nm and 1000 RPM. The highest efficiencies (>43 %) are in a λ range between 1.2 and 1.5. At high loads and engine speeds, the burn duration increases due to the longer injection time, which leads to a declining brake efficiency. It is intensified in this area by the higher friction and gas exchange losses.

5.1.2 Natural gas engine

The initial model for the new SI concepts in heavy-duty vehicles is a natural gas (CH4) engine based on [95] and [96]. This model represents a commercial state-of-the-art natural gas engine. The engine has a displacement volume of 12.5 liters and a compression ratio of 12.5, which is significantly lower than the previous Diesel model. This follows from the fact that CH4 is significantly more prone to preignition and knock phenomena. Nevertheless, due to the chemical composition of the fuel, CO_2 emissions can be reduced. Since the

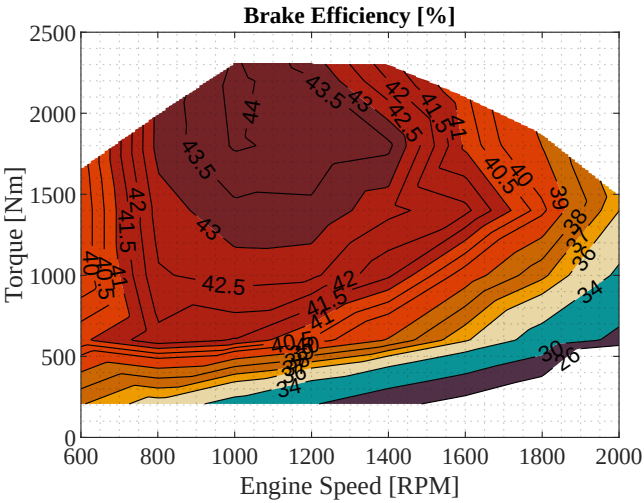

Abbildung 5.1: Brake efficiency map of the heavy-duty Diesel engine

results generated in [95] are carried out with a different burn rate model, the simulation is adapted to the models described in chapter 3. The burn rate model presented in [68] has been validated on natural gas data and is thus able to represent the fuel behavior correctly. The new models are adjusted to match the brake efficiency published in [95] with a deviation under 1 % relative.

The engine is operated stoichiometricly and has a conventional 3-way catalytic converter. Despite possible fuel consumption advantages in lean operation, stoichiometric operation is chosen due to the simpler exhaust gas aftertreatment and lower engine complexity. Furthermore, the boost pressure is provided by only one wastegate turbocharger, since, compared with the Diesel engine, no excess air needs to be provided in the combustion chamber due to stoichiometric operation. The fuel is injected via the intake port. For comparison with the following engine concepts, the power output level of the model is increased by 4 % compared to [95] and [96]. For natural gas, the knock model described in [97] is used, as this is a model developed specifically for methane-based fuels. Figure 5.2 shows the brake efficiency map of the natural gas engine.

In the characteristic map, the engine is at the optimum center of combustion.

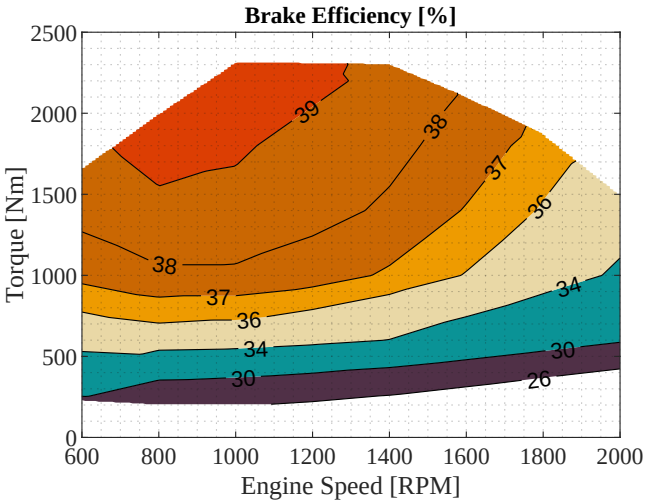

Abbildung 5.2: Brake efficiency map of the heavy-duty natural gas engine

This results in a peak efficiency of 40.0 % at 1000 RPM and 2300 Nm. At high engine speeds, the mechanical losses and gas exchange losses increase while the isochoric part of the engine process decreases (φ_{10-90} increases). A comparison of the engine concepts is given in chapter 5.1.5.

5.1.3 C65F35 engine

The natural gas engine serves as the base for further investigation with the fuel C65F35. The following adjustments are made concerning the base engine model:

- Characteristic data of the fuel
- Laminar flame speed
- Ignition delay times & knock model
- Injection concept

In [68] it was shown that the used burn rate model can represent the fuel conversion from gaseous to liquid energy sources and vice versa with high quality

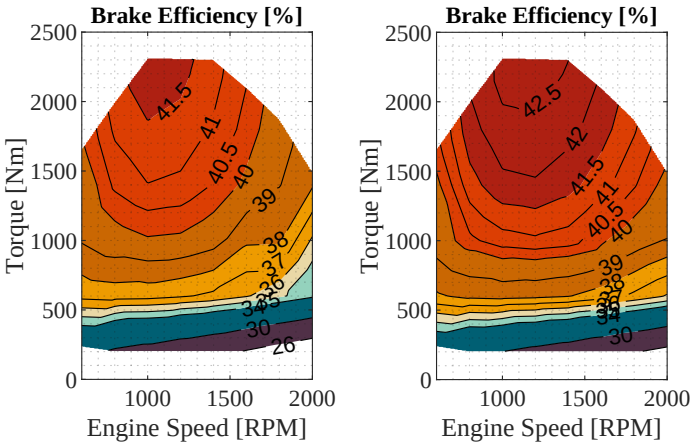

(a) Base Engine **(b)** Optimized Engine

Abbildung 5.3: Brake efficiency maps of the heavy duty C65F35 base and optimized engine

for a premixed SI combustion process. In the first step, the engine is presented with the same specifications as the natural gas engine, meaning a compression ratio of 12.5 and a displacement of 12.5 liters are used. The engine is operated stoichiometricly which is why a single-stage turbocharger is used. In addition, compared with the natural gas concept, the fuel is injected directly into the combustion chamber, which means that no fuel-air mixture needs to be supplied to the combustion chamber. In the second step, the engine parameters are adjusted to increase efficiency. This leads to an engine concept with a compression ratio of 14 and a displacement of 11.5 liters.
On the left side of figure 5.3, the brake efficiency of the engine adapted to C65F35 can be seen with its highest value of 41.8 % at 1000 RPM and 2300 Nm. Compared to the natural gas engine, the efficiency is significantly higher. The first reason is the higher laminar flame speed of C65F35, which increases the burn rate (see Appendix of [68]). Secondly, the cooling effect due to the high amount of evaporating C65F35 leads to lower combustion chamber pressures. Also, the direct injection ensures a higher amount of charge air resulting in increased power density of the engine. In the optimized concept on the left side of figure 5.3, the compression ratio and displacement volume are adjusted in such a way that the engine model meets the knock limit in the low-end torque

area. As a result, the optimum center of combustion is maintained throughout the entire engine map. The trade-off between increasing the compression ratio and the optimal center of combustion is due to the sensitive response of the knock model in the low-end torque area, which causes the efficiency losses to increase disproportionately when the compression ratio is enhanced further. Peak brake efficiency is achieved at 1200 RPM and 2300 Nm with 42.8 %. The different characteristics of the engine concepts to the Diesel concept can be observed here. The decline in efficiency from Brake specific fuel consumption (BSFC) optimum to rated power is much less pronounced compared to the CI-concepts. This is due to the increasing injection time at high loads for the Diesel engine. In chapter 3.7, it can be seen that the full-load portion is of great importance for the efficiency evaluation of heavy-duty driving cycles, which is advantageous for the SI-concepts.

5.1.4 H_2 engine

The last part of the concept discussion is the hydrogen engine. Like the C65F35 engine, the virtual engine concept is based on the natural gas engine provided by the FKFS for the subsequent studies.

The engine has a compression ratio of 12.0 and a displacement volume of 12.5 liters. One turbocharger is used and is operated in the range of λ 1.0 -4.0. The homogeneous lean burning process is particularly suitable for H_2 due to the high laminar flame speeds. This is a major advantage of the fuel. Its characteristic values were implemented, and the fuel vapor calorific calculation was adjusted. The charge motion, turbulence and burn rate model is based on the models described in chapter 3. Model validation data and quality can be reviewed in [98]. The ignition delay times were adjusted to H_2 using a simple Arrhenius approach without the influence of AFR and EGR. The knock model is based on the so-called Schmid model [54], which is used in its initial settings since no hydrogen knock measurements are available. Auto-ignition phenemena in H_2 are assumed to be triggered mainly by local hot spots or lube-oil intrusion. This is difficult to represent with 0D/1D simulation methods, which is why the results must be seen in this context. The models used allow generating an estimate of the efficiency map for hydrogen engines.

Since this engine has degrees of freedom with regard to

- Air-fuel equivalence ratio
- Throttle angle
- Turbocharger wastegate opening angle
- EGR

a calibration of the engine map was carried out at FKFS, which will be briefly described in the following. Figure 5.4 (a) shows the control strategy of the engine. The lower left area is filling-controlled by the throttle valve, while the area above is controlled by the air-fuel equivalence ratio, which varies between 1.8 and 4.0. Outside the red area λ is set to 4.0 at low torque. In this range, the wastegate controls the load. At high torque (full load), the engine is operated stoichiometrically. In this area, the wastegate of the turbocharger controls the load. Additionally EGR is introduced of up to 27 %. The discontinuity between $\lambda = 1$ and $\lambda = 1.8$ is implemented to avoid the window of high NO_x emissions between λ 1.0 and 1.8. This is also observed in [99], where λ of approx. 2.0 is stated.

Figure 5.4 (b) shows the corresponding efficiency map. The highest efficiency of 42.6 % is achieved at 1000 RPM and 1400 Nm. The steep decrease in efficiency towards engine speeds > 1600 results from the turbocharger derived of the natural gas model. Within the scope of this project, it was not possible to implement a two-stage turbocharger, which means that the brake efficiency may tend to be slightly lower in the used setup. Due to the high mass flow, the small turbocharger generates a large cylinder backpressure. The losses of efficiency in the area of the full load curve come from the later center of combustion, which is caused by the knock model.

5.1.5 Engine concept comparison

This chapter compares specific operating points of the engine concepts described above. Figure 5.5 shows a partial load point at low engine speed (top, left), a low load point at medium engine speed (top, right), and a high load point at high engine speed (bottom, left). For C65F35, the optimized concept is being

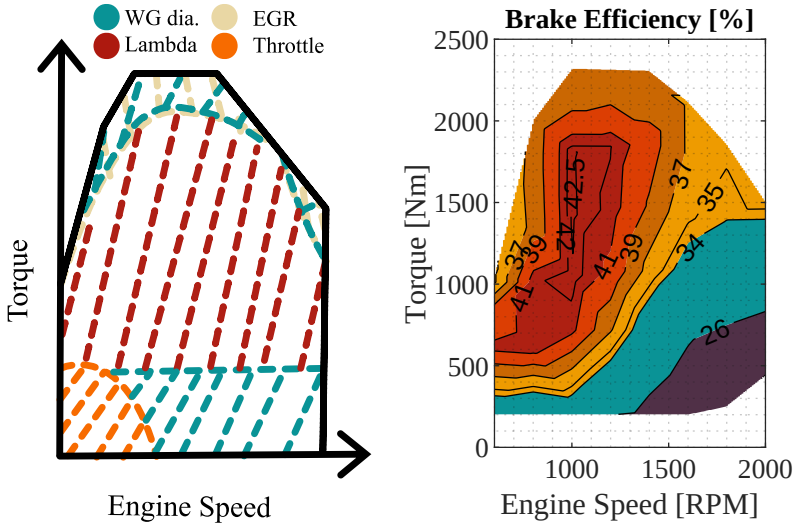

(a) Calibration scheme **(b)** Brake efficiency

Abbildung 5.4: Calibration scheme and brake efficiency map of the heavy-duty H_2 engine

compared. At the first load point, the advantages are given to the concepts that have the shortest burn duration. The burn duration of natural gas and C65F35 (approx. 24 and 25 φ_{10-90}) is about 1.5 times higher compared to H_2 and Diesel (approx. 19 and 16 φ_{10-90}). There is a further advantage for the Diesel concept that lies in the high compression ratio. However, at the expense of higher mechanical losses. To ensure mechanical stability at higher peak pressures (1.4 times higher compared to H_2 with a similar cylinder charge mass), the system must be designed to be more stable, which leads to higher mechanical losses. Despite the higher compression ratio of C65F35, the maximum pressure is lower than with natural gas, which can be attributed to the lower stoichiometric AFR. The substantial charge dilution with the H_2 concept (λ = 1.95) leads to the lowest peak temperature in the combustion chamber, resulting in the lowest heat losses.

The low load point has advantages for the concepts controlled by the air-fuel equivalence ratio concerning gas exchange losses, which play a major role in

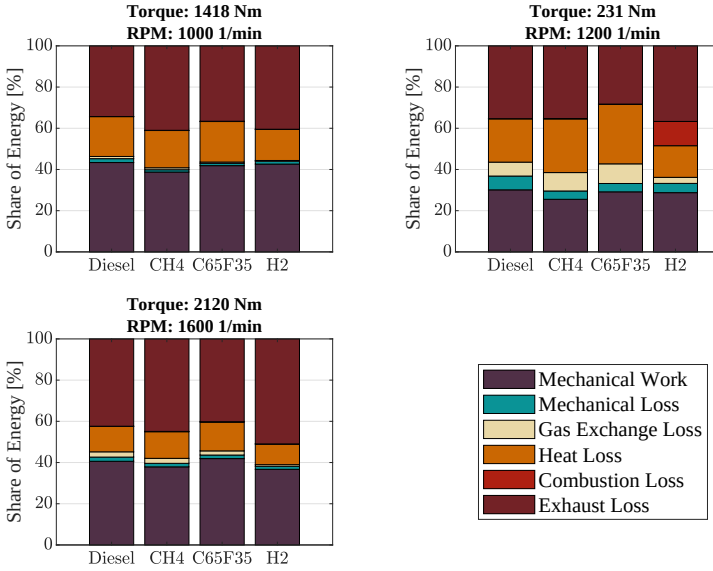

Abbildung 5.5: Share of energy of the heavy-duty engine concepts for different load points

this load area. The high λ also reduces the wall heat loss. The burn durations for Diesel and C65F35 are comparable, while the temperature level in the combustion chamber for the Diesel concept is significantly lower. This results in low wall heat losses. The share of losses is reversed for C65F35. A higher proportion is lost via the wall heat than via the exhaust gas. In the case of H_2 the burn duration increases due to the charge dilution in such a way that the fuel is not entirely converted and is wasted via the combustion losses (see also 5.3).

At high engine speeds and high loads, the advantage of C65F35 becomes obvious. The burn duration of the Diesel engine increases significantly towards higher engine speeds as fuel injection becomes relatively longer. Also, the natural gas engine has an 8 % longer burn duration than C65F35 and performs worse due to the lower compression ratio, among the other disadvantages. The H_2 engine runs in stoichiometric mode at this load point. Assuming that abnormal combustion behavior is to be avoided (back-fire, knock), the load point is

run with 20 % EGR (see [100] and [101]). The high cylinder mass causes the knock control to retard the center of combustion, and thus considerable energy is lost via the exhaust gas.

5.2 Evaluation in the RDE-Cycle

For the final analysis of the engine concepts, a real driving operation is examined according to chapter 3.7. Figure 5.6 shows the average efficiency of the individual concepts for the Stuttgart-Ulm route (see table 3.2) on the left axis. The natural gas engine performs weakest (35.5 %) while the Diesel has the best efficiency (37.7 %). The C65F35 engine nevertheless performs very well in this comparison and reaches the Diesel level within 0.1 percent efficiency in absolute terms. The H_2 engine has an efficiency of 36.5 %, which makes it slightly less efficient than the Diesel and C65F35 engines (also refer to the discussion chapter 5.3).

As a result, similar efficiencies in the real driving cycle can be achieved with a significantly less complex powertrain unit for C65F35. Since a stoichiometric concept is used, complex exhaust gas after-treatment systems can be dispensed. This also leads to lower requirements for the turbocharging concept, which makes the engine periphery more compact and, in this example, even allows one turbocharger stage to be spared.

The fuel consumption is plotted on the right axis of figure 5.6. The natural gas engine requires 29.2 kg/100km (corresponding to a tank volume of 62 l with liquid storage at a temperature of -163.5 °C and 8 bar pressure), while the H_2 engine requires 12 kg/100km (corresponding to a tank volume of 169 l with liquid storage at a temperature of -253 °C and 6 bar pressure). In the case of liquid fuels, Diesel consumption is 34.1 l/100km, while the C65F35 engine consumes 79.5 l/100km. In order to achieve a similar range for the C65F35 engine, the tank volume must be approx. 2.2 times the size of a Diesel tank. In the last chapter, the reliability of the provided results will be discussed.

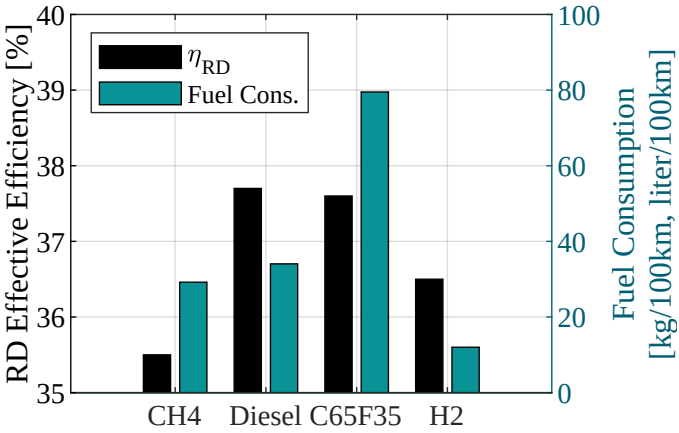

Abbildung 5.6: Real drive brake efficiency and fuel consumption (natural gas and H_2 in kg; Diesel and C65F35 in liter) of engine concepts operated with different fuels

5.3 Discussion

As in the previous chapter, the quality of the results will be discussed. The natural gas base model was built on data from an engine with a lower displacement volume. The highly-sophisticated models should be able to correctly reproduce a 4 % increment in engine displacement with the same technology. The engines' peak efficiency predicted in the simulation agrees very well with publications of other natural gas engine data (see [102]). It should be noted that natural gas engines are constantly evolving. In particular, the direct supply of gas to the combustion chamber and the use of EGR still offer plenty of potential for engines, which was not taken into account in this work [103]. In addition, the gas quality of natural gas has a strong influence on the engine operation (see [104]). In the simulation, 100 % pure methane was used, resulting in a best-case scenario for the fuel.

For the evaluation of the C65F35 engine, the components of the natural gas engine are not varied. The difference in the results is directly related to the fuel used. The turbulence of both engine concepts is at a similar level. Therefore, the models used should be able to reproduce the combustion behavior

of C65F35 very accurately and thus provide a valid estimation. The main unknown in terms of the C65F35 engine is the knock model. It is assumed that a truck engine has a different knock behavior due to lower engine speeds and different combustion chamber geometry compared to passenger car engines. Nevertheless, the knock model settings matched to the passenger car engine in the previous chapter are implemented since no heavy-duty engine data was available. This approach is justified by the fact that the knock model takes the ignition delay times of the fuel into account, where time and spatial scales are considered by the models. The process parameters (cylinder pressure and temperature) for the downsizing engine are significantly lower than the engines values used in passenger cars. For this reason it is assumed that the engine operation is far away from knocking limit.

With regard to the combustion process, the same burn rate models are used for the SI-engine variants. However, these models are based on reaction kinetics simulations. The laminar flame speeds for natural gas and C65F35 are derived from the exact reaction mechanism, while H_2 uses a different mechanism [12]. In [68] it is shown that the use of different reaction mechanisms can have an influences on the laminar flame speed calculated, which are, in this case, assumed negligible.

There are four important things to keep in mind about the H_2 engine:
The characteristic map calibration has not been optimized for the best efficiency concept and therefore serves as an example of how the calibration could be executed.
As a second point, the default settings of the knock model are used, which has not been validated for H_2 combustion. Since the ignition delay times are implemented without EGR and lambda dependency as input variables for the knock model, the most significant uncertainty for the engine efficiency map can be seen here. This subject represents a major research demand for future predictive H_2 knock models and is far beyond the scope of this work.
There is also a strong demand for further research in the emission models for H_2 engines. In the above example, λ was limited to 1.8 to avoid NO_x emissions that are too high for the present consideration. However, this value is only an estimate due to the lack of reliable measurements. There is still potential in terms of optimizing engine operation.
The last point to mention for the H_2 engine is the turbocharger, which was taken from the natural gas engine model. This turbocharger is significantly un-

dersized for high λ and high engine speeds and causes a substantial decrease in efficiency due to the increasing exhaust backpressure. The high combustion losses of the H_2 engine (see chapter 5.1.5) at low speeds are rooted in the de-throttling of the engine. Changing the operating strategy to achieve higher combustion speeds would also be conceivable, but will increase the gas exchange losses. The efficiency gain is estimated to be high, but the effect on the real drive results is estimated to be low for this measure.

The validation of the real driving cycle is based on published data from commercial vehicle magazines on the fuel consumption of Diesel trucks. The route analyzed in the simulation has a similar topography to the truck test route used in [105]. In a real drive test of the truck modeled in this work, fuel consumption of 35.9 liters/100km Diesel was measured with a fully-loaded vehicle [106]. The simulated fuel consumption of the Diesel engine concept on the route described in 3.7 is 34.1 liters/100km. The model is thus considered validated.

The C65F35 engine concepts still have a lot of potential with the major levers:

- Increase of the turbulence level to enhance the combustion speed
- better choice of compression ratio thanks to the improved knowledge on knock behavior
- charge dilution

Many studies are being carried out on the enhancement of the combustion speed, especially in the passenger car sector. For SI-engines, there is excellent potential for a combination of swirl and tumble to increase charge motion [107]. Due to the reduced combustion duration, the efficiency can be improved significantly. This is also reflected in a lower knocking tendency at the expense of higher peak pressures.
Since C65F35 has proven to be an extremely promising fuel for future heavy-duty engines based on the results shown, wide-ranging investigations on the knock behavior of the fuel based on test-bench data should be carried out. This allows the engine concepts to be developed to the limits of the fuels properties. An optimization measure for the C65F35 is a homogeneous lean operation. In chapter 4, it was shown that lean operation results in significant advantages in terms of efficiency. With regard to NO emissions, the degree of charge dilution could also be lower than with gasoline due to the evaporative cooling of

C65F35. This also significantly reduces the workload of the turbocharger. In summary, this enables C65F35 engine concepts to be a cost / high efficient, and low emission solution for future mobility, with a vast potential for further optimization.

6 Conclusion and Outlook

In the course of this thesis, models were adjusted and validated for the e-fuel C65F35 and the gasoline blend fuel G85F15. These models can be used to design engine concepts at an early stage of development. This enables the potential of synthetic fuels to be evaluated. For the development of future propulsion concepts, the simulative design of these concepts is an essential component. The quality of the further developed and validated submodels were discussed in detail, and it was shown that measured test bench data could be reproduced very well with the models.

When examining the engine models with the synthetic fuel C65F35, three main findings can be identified:

- The knock behavior of the fuel no longer necessarily limits the engine concepts.
- With increasing compression ratio, the combustion chamber geometry is of decisive importance for the combustion process, resulting from its influence on charge movement and flame propagation.
- The combustion duration is longer, especially at lower loads, due to the slower laminar flame speed and lower process temperatures compared to gasoline.

The same applies to the G85F15 fuel, although less significantly.

In addition to proper model implementation, a major challenge was to adapt the engine concepts to the respective fuel. The requirements of the engine concepts for C65F35, G85F15, and gasoline are clearly different. This behavior of the fuels can be assessed in the engine map based on a state-of-the-art passenger car engine. It can be shown that C65F35 and G85F15 have clear advantages over gasoline in the upper load range in terms of efficiency due to the higher knock resistance. In the lower part-load range, this advantage is not relevant.

In this case, gasoline showed a higher efficiency. Fistly because of the higher laminar flame speed, secondly because the higher mixture heating value of the blended fuel and even higher mixture heating value for C65F35. This effects causes the engine model to be throttled significantly more. This already indicates a high downsizing potential for the investigated fuels. The lower air demand of C65F35 significantly reduces the load on the charging group and results in more degrees of freedom for the engine design. The fuel properties in terms of knock behavior are also advantageous for the design, making a significantly more compact engine design possible.

For the state-of-the-art passenger car engine, the assessment in the virtual RDE for gasoline shows advantages in terms of efficiency. This is no longer the case when the engines are adapted to the respective fuel. The downsizing potential for cost-efficient engine concepts already leads to significant advantages for C65F35 over gasoline. By reducing the displacement volume, it can be shown that the efficiency of the concept can increase by 1 point in the real driving cycle with less complexity of the ICE. The complexity refers to components used to increase the efficiency of the basic variant (variable valve train, cylinder deactivation). The blended fuel can maintain the efficiency level of its base variant at lower complexity and size.

An increasing efficiency of up to 10 % is possible for the high-efficiency C65F35 concept compared to the conventional state-of-the-art gasoline engine in RDE. This lean-burn engine concept can be maintained within the emission standards with conventional exhaust gas after-treatment systems (SCR and LNT). It has been shown that this is possible with significantly less mixture dilution compared to G100, which is also demonstrated in emission measurement on the test bench. The resulting lower mass flows are advantageous for turbocharging, leading to more efficient design possibilities. With measures to increase turbulence during combustion (active pre-chamber ignition, high-turbulence concepts), efficiency could even be increased by up to 16 %. The G85F15 engine also shows an efficiency growth of 4 % in the driving cycle, although with significantly higher NO emissions.

The evaluation of a C65F35 engine for heavy-duty vehicles was carried out analogously to the passenger car section. Based on a modified methane engine, the combustion process can be switched to C65F35. At the same turbulence level, efficiency advantages can already be achieved compared to the methane

engine. With a C65F35 downsizing concept, this corresponds to an advantage of 6 % in the virtual real driving cycle. This is due to the better knock behavior of C65F35 and the disadvantageous port-injection technology with methane. In a cross-comparison with conventional Diesel fuel, the enormous potential of C65F35 engine concepts becomes ovious. C65F35 shows similar efficiencies to conventional Diesel fuel in the real drive cycle. The major advantage of the C65F35 concept is the much simpler exhaust gas after-treatment since a conventional 3-way catalyst can be used due to the stoichiometric concept. Secondly, the turbocharger is subjected to significantly less workload, which means that it is possible to move from twin-turbocharging to a single turbocharging system, leading to additional components being saved. Since this is a stoichiometric concept, further high potential can be expected in the combustion process especially for lean engine concepts, which could be subject in further research projects.

Only one pure and one blended possible candidate for future mobility with e-fuels was discussed in this work. Since the 0D/1D simulation allows the fuel to be exchanged in a comparably simple way, further fuels can be analyzed in future works with existing models since many other fuels show high potential for further efficiency increases with lowest possible emissions. Methanol, for example, is currently being treated as a promising fuel for the future. As this fuel has similar material properties, especially regarding to its heating value compared to C65F35, an investigation would be highly recommended. The more efficient production of methanol has an advantage, as the discussed fuels are produced perspectively on the basis of methanol. Nevertheless, a disadvantage of methanol is its toxicity to the human body, which necessitates strong efforts towards safety in engine concepts, making the propulsion system expensive.

The much-discussed polyoxymethylene dimethyl ethers (PODE) for Diesel engines, which consists of longer-chain molecules than DMC and MeFo, is also based on methanol in production. This leads to the assumption that the production of PODEs is more cost-intensive per energy content of the fuel, making alternative gasoline fuels more attractive for future mobility. In addition, these are not suitable as a drop in solution for existing engines.

Outside the combustion process, however, there are still problems with the fuels under consideration which need to be solved technically. MeFo, for example, tends to decompose to formic acid in the presence of water. This can

be prevented if the fuel is suitably additivated. However, further research is needed in this area. It has also been shown that some of the plastics used in the internal combustion engine are incompatible with DMC and MeFo. These components must be replaced specifically.

The knowledge gained will enable a well-founded assessment of synthetic fuels in engine operation for a comprehensive evaluation of different propulsion concepts. This can provide guidance for political decisions based on systemic analyses regarding the environmental impact and energy balance throughout the entire life cycle of products.

Finally, the potential that still lies in the combustion engine should be mentioned once again, especially concerning alternative fuels. If the development in this area is strongly reduced, these are disadvantageous preconditions for a CO_2 neutral society in the future. The results encourage for further pursuing research and development work on synthetic fuels, which can provide a fast and cost-effective route to sustainable future mobility.

Appendix

Tabelle A.1: Values of the adjustment parameters in the 3D CFD Simulation

Parameter	Value
Combustion model constant α	1.3
Combustion model constant β	1.0

Tabelle A.2: Values of a_{δ_L} [17, 18, 19]

Fuel	a_{δ_L} [-]
Gasoline	1.6661
C65/F35	1.652

Tabelle A.3: Calibration parameters of the laminar flame speed model: gaseous fuels

Parameter	Unit	G100	C65F35
L_{min}	-	14.3	4.64
Z^*_{st}	-	0.063669935	0.173611111
E_i	K	51133.83901	56157.85934
B_i	bar	6.16492001E+17	6.14883E+17
m	-	1.5	1.5
r	-	0.985	0.985
n	-	2.439	2.439
F	m/s	0.005920496	0.018121893
G	K	-9017.0561	-8610.31
n_{EGR}	-	1.592770067	1.037942506
n_a	-	0.945493	0.94549
c	-	0.747894	0.74789
b_{yH20}	-	0.431049978	0.975659811
d_{yH20}	-	8.621163808	30.00

Tabelle A.3: Calibration parameters of the laminar flame speed model: splines for methane and gasoline

	G100				C65F35			
λ	S1 [-]	S2 [-]	S3 [K]	S4 [-]	S1 [-]	S2 [-]	S3 [K]	S4 [-]
0.6	0.0000	1.017912	1412.1	0.7688	-0.06165463	1.00576514	1339.67078	0.75365897
0.7	0.0000	1.017446	1522.1	0.8084	-0.04922269	1.00784653	1476.78705	0.78733008
0.8	0.0000	0.996815	1707.8	0.6482	-0.03981091	0.99813438	1691.72111	0.64458907
0.9	0.0000	0.995619	1889.3	0.5837	-0.03932092	1.00552895	1880.01205	0.5698946
1	0.0000	0.995548	1958.0	0.5090	-0.03538999	1.00568551	1947.18081	0.52646447
1.1	0.0000	0.996459	1931.5	0.4932	-0.00464921	0.98579541	1919.05352	0.49561178
1.2	0.0000	1.000830	1847.1	0.5800	0.00636085	0.98176496	1826.69813	0.58065503
1.3	0.0176	0.983174	1718.5	0.5391	0.01745615	0.96820217	1750.67021	0.54417913
1.4	0.0288	0.972679	1611.7	0.5532	0.02832031	0.95590648	1647.70849	0.55960007
1.5	0.0409	0.960939	1521.3	0.5446	0.03964983	0.93906281	1548.99895	0.54935489
1.6	0.0542	0.948393	1433.8	0.5527	0.05257797	0.92390624	1460.77312	0.55951251
1.7	0.0689	0.931626	1366.8	0.5353	0.06731248	0.91124647	1406.42673	0.55769245
1.8	0.0818	0.920171	1300.1	0.5423	0.07993159	0.89359368	1342.7093	0.54194641
1.9	0.0946	0.907679	1240.6	0.5499	0.09247153	0.87427902	1263.88411	0.5489261
2	0.1074	0.891913	1180.4	0.5563	0.10495744	0.8621375	1210.24623	0.56590719
2.1	0.1203	0.875526	1127.4	0.5631	0.11800274	0.84861052	1165.64557	0.57280733
2.2	0.1331	0.859768	1077.0	0.5693	0.1269517	0.83776101	1124.7586	0.58107062
2.3	0.1460	0.846646	1038.1	0.577	0.15053307	0.81948838	1092.18845	0.58466152
2.4	0.1588	0.831071	997.1	0.5841	0.15355805	0.84077614	1098.00367	0.64775382
2.5	0.1716	0.820481	971.1	0.5943	0.17334996	0.79152992	1019.48976	0.59559376
2.6	0.1845	0.808074	941.7	0.6032	0.18401177	0.81979381	954.373542	0.6049062
2.7	0.1973	0.797971	919.3	0.6141	0.19688313	0.80699068	923.994106	0.61299207
2.8	0.2101	0.778220	880.7	0.6188	0.20969527	0.79406834	895.089336	0.62145187
2.9	0.2230	0.764619	855.3	0.6278	0.22258843	0.78120768	868.71632	0.62985577
3	0.2358	0.743352	815.5	0.6356	0.23556417	0.76833242	843.822566	0.63785308
4	0.3642	0.637878	674.5	0.7171	0.36207944	0.63496512	631.427359	0.72384311
5	0.4925	0.510704	508.1	0.7986	0.50699991	0.55164567	585.723591	0.77786751

Figure A.1 shows the burn rate of the measurement data (PTA) and the burn rate of the WPC on the left for G85F15. On the right side, the deviation of the IMEP is shown, which is significantly lower than 5 % for most load points.

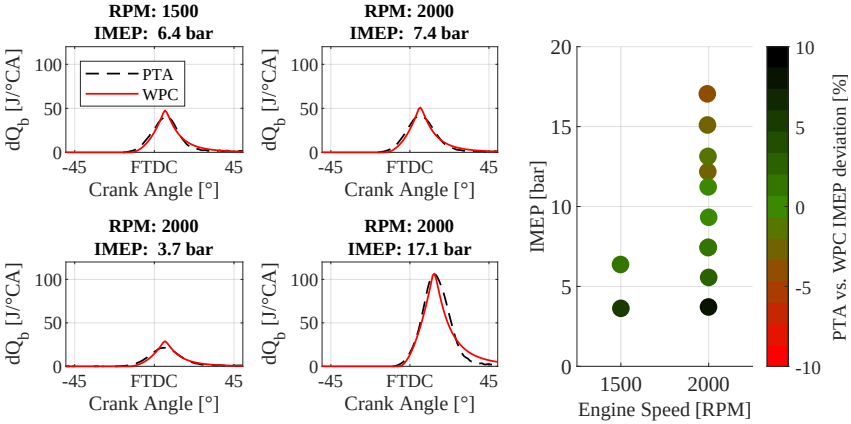

Abbildung A.1: Comparison of the PTA and WPC burn rate for a engine load and speed variation (left) of the SCE for G85F15 and deviation of IMEP (right)

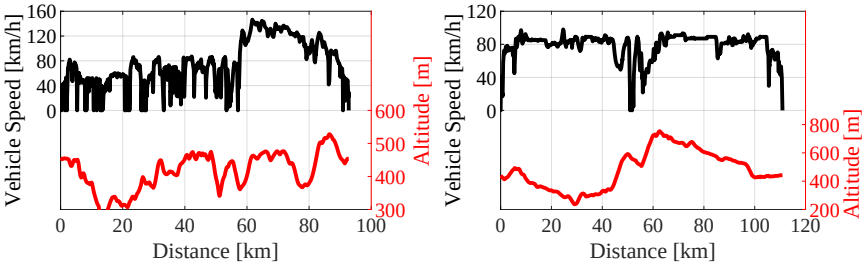

(a) Passenger car RDE

(b) Heavy-duty cycle

Abbildung A.2: Vehicle speed and altitude profile of the driving cycles

Tabelle A.4: Ignition delay time model parameters of C65F35

τ_i	Parameter	Unit	C65/F35
τ_1	A	[s]	3.12 E-15
	α_1	[-]	0.904280937
	α_2	[-]	6.957069939
	α_3	[-]	-8.444290489
	A_2	[K]	17309.01746
τ_2	A	[s]	7.63E-6
	α_1	[-]	-1.185932067
	α_2	[-]	1.123353421
	α_3	[-]	-2.913819107
	A_2	[K]	11526.48545
τ_3	A_1	[s]	2.03457E-8
	α_1	[-]	-0.894181338
	α_2	[-]	0.623832894
	α_3	[-]	- 0.116471289
	A_2	[K]	17770.02333
	b_{scale}	[-]	1.18

Tabelle A.5: Reaction kinetics constants model parameters of the NO model

Parameter	Unit	Value
A1f	[-]	9.912992
A1b	[-]	3.822929
A2f	[-]	0.62847
A2b	[-]	0.485813
A3f	[-]	4.439072
A3b	[-]	9.406126
b1f	[-]	0
b1b	[-]	0
b2f	[-]	1.5
b2b	[-]	1.612
b3f	[-]	0
b3b	[-]	-0.212
Ea1f	[-]	72.707609
Ea1b	[-]	0
Ea2f	[-]	5.68
Ea2b	[-]	37.69
Ea3f	[-]	0
Ea3b	[-]	49.34

Literaturverzeichnis

[1] M. Härtl, S. Blochum, C. Kraus, and G. Wachtmeister, "Energy carriers for future mobility," in *Internationaler Motorenkongress 2021*, 2021. doi: 10.1007/978-3-658-35588-3_23.

[2] Agora Verkehrswende und Agora Energiewende, "Die zukünftigen Kosten strombasierter synthetischer Brennstoffe: Schlussfolgerungen aus Sicht von Agora Verkehrswende und Agora Energiewende," https://www.agora-energiewende.de/fileadmin/Projekte/2017/SynKost_2050/Agora_SynCost-Studie_WEB.pdf (accessed June 5, 2022).

[3] M. Bargende, F. Negüs, V. Kelich, C. Beidl, A. Kuznik, M. Grill, A. Döhler, A. Kulzer, "Potential of the methanol-powered SI engine in the hybrid powertrain: A simulative investigation," in *Der Antrieb von morgen 2021*, Springer Berlin Heidelberg, 2021. doi: 10.1007/978-3-662-63403-5_6.

[4] V. Kumar Sahu, I. Singh, A. Dhar, P. Kumar, P. Chandra Shukla, "Investigation on the effect of injection timings on combustion, performance and emissions of a pure methanol fuelled DISI engine through 1-D simulations," in *Engine Modeling and Simulation*, Springer Singapore, 2022. doi: 10.1007/978-981-16-8618-4_11.

[5] European Environment Agency, "CO2 emission intensity," https://www.eea.europa.eu/data-and-maps/daviz/co2-emission-intensity (accessed June 5, 2022).

[6] Wissenschaftliche Dienste des Deutschen Bundestages, "CO2-Bilanzen verschiedener Energieträger im Vergleich: Zur Klimafreundlichkeit von fossilen Energien, Kernenergie und Erneuerbaren Energien," 2007. https://www.bundestag.de/resource/blob/406432/70f77c4c170d9048d88dcc3071b7721c/wd-8-056-07-pdf-data.pdf (accessed June 5, 2022).

[7] The European Parliament and the Council of the European Union, "Directive (eu) 2018/2001," *Official Journal of the European Union*, 2018.

[8] Weltenergierat Deutschland e. V./ Frontier Economics, "International aspects of a power-to-x roadmap: A report prepared for the world energy council germany," 2018. https://www.frontier-economics.com/media/2642/frontier-int-ptx-roadmap-stc-12-10-18-final-report.pdf (accessed June 5, 2022).

[9] F. vom Lehn, S. Jacobs, C. Bariki, Q. Mao, D. Yan, J. Beeckmann, K. A. Heufer, H. Pitsch, and L. Cai, "Combustion kinetics of the synthetic e-fuels methyl formate and dimethyl carbonate: A modeling and experimental study," in *30. Deutscher Flammentag, September 28-29, Hannover (Germany) / Online, 2021*.

[10] L. Cai, A. Ramalingam, H. Minwegen, K. Alexander Heufer, and H. Pitsch, "Impact of exhaust gas recirculation on ignition delay times of gasoline fuel: An experimental and modeling study," *Proceedings of the Combustion Institute*, 2019. doi: 10.1016/j.proci.2018.05.032.

[11] M. Wenig, M. Grill, and M. Bargende, "A new approach for modeling cycle-to-cycle variations within the framework of a real working-process simulation," *SAE International Journal of Engines*, 2013. doi: 10.4271/2013-01-1315.

[12] Gregory P. Smith, David M. Golden, Michael Frenklach, Nigel W. Moriarty, Boris Eiteneer, Mikhail Goldenberg, C. Thomas Bowman, Ronald K. Hanson, Soonho Song, William C. Gardiner, Jr., Vitali V. Lissianski, and Zhiwei Qin, "Gri-mech 3.0," http://combustion.berkeley.edu/gri-mech/ (accessed June 5, 2022).

[13] Ye Feng, "3d simulation of an si-engine operated with synthetic fuel" *Master's thesis*, 2021.

[14] T. Maier, M. Härtl, E. Jacob, and G. Wachtmeister, "Dimethyl carbonate (dmc) and methyl formate (mefo): Emission characteristics of novel, clean and potentially CO2-neutral fuels including pmp and sub-23 nm nanoparticle-emission characteristics on a spark-ignition DI-engine," 2019. doi: 10.1016/j.fuel.2019.115925.

[15] G. P. Merker and R. Teichmann, *Grundlagen Verbrennungsmotoren: Funktionsweise und alternative Antriebssysteme Verbrennung, Messtechnik und Simulation*. Wiesbaden: Springer Vieweg, 2018. doi: 10.1007/978-3-658-19212-9.

[16] Eichler, F., Demmelbauer-Ebner, W., Theobald, J., Stiebels, B., "Der neue EA211 TSI evo von Volkswagen," International Vienna Motor Symposium, 2016. doi: 10.1007/978-3-658-19212-9.

[17] S. Hann, M. Grill, and M. Bargende, "Reaction kinetics calculations and modeling of the laminar flame speeds of gasoline fuels," *SAE Technical Paper*, 2018. doi: 10.4271/2018-01-0857.

[18] S. Hann, L. Urban, M. Grill, and M. Bargende, "Prediction of burn rate, knocking and cycle-to-cycle variations of binary compressed natural gas substitutes in consideration of reaction kinetics influences," *International Journal of Engine Research*, 2018. doi: 10.1177/1468087417732883.

[19] Hann, S., Grill, M., Bargende, M., "A quasi-dimensional si combustion model predicting the effects of changing fuel, air-fuel-ratio, egr and water injection," in *SAE Technical Paper*, 2020. doi: 10.1007/978-3-658-33232-7.

[20] V. Masson-Delmotte, P. Zhai, A. Pirani, *Climate Change 2021: The Physical Science Basis. Contribution of Working Group I to the Sixth Assessment Report of the Intergovernmental Panel on Climate Change*. Cambridge University Press, 2021.

[21] Bundesregierung, "Klimaschonender Verkehr," `https://www.bundesregierung.de/breg-de/themen/klimaschutz/klimaschonender-verkehr-1794672` (accessed June 5, 2022).

[22] Shell, "Sky scenario," 2018. `https://www.shell.com/energy-and-innovation/the-energy-future/scenarios/shell-scenario-sky.html` (accessed June 5, 2022).

[23] Eurostat, "Abhängigkeit von Energieimporten in Deutschland in den Jahren 2002 bis 2019," 2021. `https://ec.europa.eu/eurostat/databrowser/view/sdg_07_50/default/table?lang=en` (accessed June 5, 2022).

[24] Bundestag, "Bundes-Klimaschutzgesetz vom 12. Dezember 2019 (BGBl. I S. 2513), das durch Artikel 1 des Gesetzes vom 18. August 2021 (BGBl. I S. 3905) geändert worden ist," 2019. https://www.gesetze-im-internet.de/ksg/BJNR251310019.html

[25] European Commission, "The european green deal," *COM(2019) 640 final*, 2019.

[26] China Association of Automobile Manufacturers, "Sales of autombiles/sales of new energy vehicles," 2022. http://en.caam.org.cn (accessed June 5, 2022).

[27] European Commission, "Development of post-euro 6/VI emission standards for cars, vans, lorries and buses," https://ec.europa.eu/info/law/better-regulation/have-your-say/initiatives/12313-Europaische-Normen-fur-Fahrzeugemissionen-Euro-7*-fur-Pkw-leichte-Nutzfahrzeuge-Lastkraftwagen-und-Busse_de (accessed June 5, 2022).

[28] Statistisches Bundesamt Destatis/StBA, "Straßenverkehr: EU-weite CO2–Emissionen seit 1990 um 29 % gestiegen," https://www.destatis.de/Europa/DE/Thema/Umwelt-Energie/CO2_Strassenverkehr.html (accessed August 5, 2022).

[29] DIN e.V., "DIN EN 228," 2017.

[30] O. Scharrer, P. Wieske, M. Warth, D. Schwarzenthal, K. Dums, and T. Wasserbäch, "Fahrspaß ohne Reue dank synthetischem Kraftstoff-Blend," in *40. Internationales Wiener Motorensymposium 15.-17. Mai 2019*, Band 2, 2019.

[31] Porsche AG, "Baubeginn für weltweit erste integrierte kommerzielle Anlage zur Herstellung von eFuels," https://newsroom.porsche.com/de/2021/unternehmen/porsche-baubeginn-kommerzielle-anlage-herstellung-co2-neutrale-kraftstofe-chile-25681.html (accessed June 5, 2022).

[32] F. Mantei, R. E. Ali, C. Baensch, S. Voelker, P. Haltenort, J. Burger, R.-U. Dietrich, N. von der Assen, A. Schaadt, J. Sauer, and O. Salem, "Techno-economic assessment and carbon footprint of processes

for the large-scale production of oxymethylene dimethyl ethers from carbon dioxide and hydrogen," *Sustainable Energy & Fuels*, 2022. doi: 10.1039/D1SE01270C

[33] R. van Basshuysen, *Ottomotor mit Direkteinspritzung: Verfahren, Systeme, Entwicklung, Potenzial*. Wiesbaden: Springer Fachmedien Wiesbaden GmbH, 2013. ISBN: 9783658014087.

[34] R. Golloch, *Downsizing bei Verbrennungsmotoren: Ein wirkungsvolles Konzept zur Kraftstoffverbrauchssenkung*. Berlin, Heidelberg: Springer Berlin Heidelberg, 2005. doi: 10.1007/3-540-27490-1.

[35] N. Fraser, H. Blaxill, G. Lumsden, and M. Bassett, "Challenges for increased efficiency through gasoline engine downsizing," *SAE International Journal of Engines*, 2009. doi: 10.4271/2009-01-1053.

[36] E. Sher and T. Bar-Kohany, "Optimization of variable valve timing for maximizing performance of an unthrottled SI engine - a theoretical study," *Energy*, 2002. doi: 10.1016/S0360-5442(02)00022-1.

[37] F. Bozza, V. de Bellis, A. Gimelli, and M. Muccillo, "Strategies for improving fuel consumption at part-load in a downsized turbocharged si engine: a comparative study," *SAE International Journal of Engines*, 2014. doi: 10.4271/2014-01-1064.

[38] GOMECSYS, "A fully variable VCR crankshaft." `https://gomecsys.com/` (accessed June 5, 2022).

[39] R. Weinowski, K. Wittek, C. Dieterich, and J. Seibel, "Zweistufige variable Verdichtung für Ottomotoren," *MTZ - Motortechnische Zeitschrift*, vol. 73, no. 5, 2012. doi: 10.1007/s35146-012-0323-4.

[40] M. Wilcutts, H.-J. Schiffgens, and M. Younkins, "Co2-reduzierung durch dynamische zylinderabschaltung," *MTZ - Motortechnische Zeitschrift*, vol. 80, no. 4, 2019. doi: 10.1007/s35146-019-0011-8.

[41] A. W. Berntsson, G. Josefsson, R. Ekdahl, R. Ogink, and B. Grandin, "The effect of tumble flow on efficiency for a direct injected turbocharged downsized gasoline engine," *SAE International Journal of Engines*, 2011. doi: 10.4271/2011-24-0054.

[42] A. Kuznik, F.Negüs, V.Kelich, M. Thielen, E. Wenz, C. Wouters, *ICE2025+: Ultimate System Efficiency: Limits of overall SI engine efficiency in hybridized powertrains*. Final report FVV-Project no. 1307. Frankfurt am Main: Forschungsvereinigung Verbrennungskraftmaschinen, 2020.

[43] M. Sens and E. Binder, "Vorkammerzündung als Schlüsseltechnologie für den zukünftigen Antriebsmix," *MTZ - Motortechnische Zeitschrift*, no. 2, 2019. doi: 10.1007/s35146-018-0152-1.

[44] K. Takeuchi, P. Luszcz, and P. Adomeit, "Konzeptentwicklung und Validierung eines homogenen Otto-Magerbrennverfahrens," *MTZ - Motortechnische Zeitschrift*, vol. 80, no. 3, 2019. doi: 10.1007/s35146-018-0161-0.

[45] J. Ganser, H. Blaxill, and A. Cairns, "Hochlast-AGR am turboaufgeladenen Ottomotor," *MTZ - Motortechnische Zeitschrift*, vol. 68, no. 7-8, 2007. doi: 10.1007/BF03227421.

[46] M. Tabata, T. Yamamoto, and T. Fukube, "Improving NOx and fuel economy for mixture injected si engine with EGR," in *SAE Technical Paper Series*, SAE Technical Paper Series, 1995. doi: 10.4271/950684.

[47] D. Zeppei, S. Koch, and A. Rohi, "Wälzlagerungstechnologie für PKW-Turbolader," *MTZ - Motortechnische Zeitschrift*, vol. 77, no. 11, 2016. doi: 10.1007/s35146-016-0112-6.

[48] S. Arnold, D. Calta, K. Dullack, C. Judd, and G. Thompson, "Development of an ultra-high pressure ratio turbocharger," in *SAE Technical Paper Series*, 2005. doi: 10.4271/2005-01-1546.

[49] Q. Bi, H. Chen, X. Zou, L. Zhu, and H. Ding, "Five-axis flank milling for design and manufacture of turbocharger compressor impeller," in *Proceedings of the ASME Turbo*. doi: 10.1115/GT2014-25014.

[50] Garrett Motion Inc., "The case for electric turbo to optimize performance, efficiency in advanced hybrid powertrains," 2019. `https://www.garrettmotion.com` (accessed June 5, 2022).

[51] S. Liu, E. R. Cuty Clemente, T. Hu, and Y. Wei, "Study of spark ignition engine fueled with methanol/gasoline fuel blends," *Applied Thermal Engineering*, 2007. doi: 10.1016/j.applthermaleng.2006.12.024.

[52] S. Blochum, B. Gadomski, M. Retzlaff, F. Thamm, C. Kraus, M. Härtl, R. Gelhausen, S. Hoppe, and G. Wachtmeister, "Potential analysis of a dmc/mefo mixture in a DISI single and multi-cylinder light vehicle gasoline engine," in *SAE Technical Paper Series*, 2021. doi: 10.4271/2021-01-0561.

[53] Gamma Technologies LLC, "GT-Power," User's Manual GT-Suite Version 2021. Westmont (USA): Gamma, 2021.

[54] M. Grill, D. Rether, and M.-T.Keskin, "FKFS Usercylinder v2.7.0," 2021. `www.usercylinder.com` (accessed June 5, 2022).

[55] R. Pischinger, *Thermodynamik der Verbrennungskraftmaschine*. Wien: Springer Vienna, Dritte Auflage, 2009. doi: 10.1007/978-3-211-99277-7.

[56] M. Grill, A. Schmid, M. Chiodi, H.-J. Berner, and M. Bargende, "Calculating the properties of user-defined working fluids for real working-process simulations," *SAE Technical Paper*, 2007. doi: 10.4271/2007-01-0936.

[57] D. G. Goodwin, H. K. Moffat, and R. L. Speth, "Cantera: An object-oriented software toolkit for chemical kinetics, thermodynamics, and transport processes. version 2.2.1," 2016. doi: 10.5281/zenodo.45206.

[58] S. R. Turns, *An introduction to combustion: concepts and applications*. Boston: McGraw-Hill, 2011. ISBN: 0073380199.

[59] Siemens Digital Industries Software, "Simcenter Star-CCM+ user guide: Version 2021.2," 2021.

[60] N. Peters, *Turbulent Combustion*. Cambridge monographs on mechanics, Cambridge: Cambridge University Press, 2000. doi: 10.1017/CBO9780511612701.

[61] S. Fritsch, S. Fasse, Q. Yang, M. Grill, and M. Bargende, "A quasi-dimensional charge motion and turbulence model for spark injection engines with fully variable valve train and direct fuel injection," in *Experten-Forum Powertrain: Ladungswechsel und Emissionierung 2020*, doi: 10.1007/978-3-658-28709-2_3.

[62] C. Bossung, M. Grill, M. Bargende, and O. Dingel, "A quasi-dimensional charge motion and turbulence model for engine process calculations," in *15. Internationales Stuttgarter Symposium*, 2015. doi: 10.1007/978-3-658-08844-6_68.

[63] S. Fritsch, M. Grill, M. Bargende, and O. Dingel, "A phenomenological homogenization model considering direct fuel injection and EGR for SI engines," in *SAE Technical Paper Series*, 2020. doi: 10.4271/2020-01-0576.

[64] Q. Yang, M. Grill, and M. Bargende, "A quasi-dimensional charge motion and turbulence model for diesel engines with a fully variable valve train," in *SAE Technical Paper Series*, 2018. doi: 10.4271/2018-01-0165.

[65] M. Grill, T. Billinger, and M. Bargende, "Quasi-dimensional modeling of spark ignition engine combustion with variable valve train," *SAE Technical Paper*, 2006. doi: 10.4271/2006-01-1107.

[66] U. C. Müller, M. Bollig, and N. Peters, "Approximations for burning velocities and markstein numbers for lean hydrocarbon and methanol flames," *Combustion and Flame*, 1997. doi: 10.1016/S0010-2180(96)00110-1.

[67] J. Ewald, *A level set based flamelet model for the prediction of combustion in homogeneous charge and direct injection spark ignition engines*. Gottingen: Cuvillier Verlag, 2006. ISBN: 9783736918009.

[68] S. Hann, *A quasi-dimensional SI burn rate model for carbon-neutral fuels*. PhD thesis, University of Stuttgart, 2021. doi: 10.1007/978-3-658-33232-7.

[69] A. Fandakov, M. Grill, M. Bargende, and A. C. Kulzer, "Two-stage ignition occurrence in the end gas and modeling its influence on engine knock," *SAE International Journal of Engines*, 2017. doi: 10.4271/2017-24-0001.

[70] A. Fandakov, M. Grill, M. Bargende, and A. C. Kulzer, "A two-stage knock model for the development of future si engine concepts," *SAE Technical Paper*, 2018. doi: 10.4271/2018-01-0855.

[71] J. C. Livengood and P. C. Wu, "Correlation of autoignition phenomena in internal combustion engines and rapid compression machines," *Symposium on Combustion*, 1955. doi: 10.1016/S0082-0784(55)80047-1.

[72] G. A. Weisser, *Modelling of combustion and nitric oxide formation for medium-speed DI diesel engines: a comparative evaluation of zero- and three-dimensional approaches*. PhD thesis, ETH Zurich, 2001. doi: 10.3929/ETHZ-A-004317089.

[73] C. Elmqvist, F. Lindström, H.-E. Angström, B. Grandin, and G. Kalghatgi, "Optimizing engine concepts by using a simple model for knock prediction," in *SAE Technical Paper Series*, 2003. doi: 10.4271/2003-01-3123.

[74] M. Hess, M. Grill, M. Bargende, and A. C. Kulzer, "Two-stage 0d/1d knock model to predict the knock boundary of si engines," in *21. Internationales Stuttgarter Symposium*, Wiesbaden: Springer Fachmedien Wiesbaden, 2021. doi: 10.1007/978-3-658-33466-6_37.

[75] M. Rößler, T. Koch, C. Janzer, and M. Olzmann, "Wirkmechanismen der dieselmotorischen NO2-Bildung," *MTZ - Motortechnische Zeitschrift*, vol. 78, no. 7-8, 2017. doi: 10.1007/s35146-017-0055-6.

[76] J. Warnatz, U. Maas, and R. W. Dibble, *Combustion: Physical and chemical fundamentals, modeling and simulation, experiments, pollutant formation*. Berlin and Heidelberg: Springer, 2006. ISBN: 978-3-540-25992-3.

[77] G. Heider, *Rechenmodell zur Vorausrechnung der NO-Emission von Dieselmotoren*, 1996. `https://books.google.de/books?id=RdI0NAEACAAJ` (accessed June 5, 2022).

[78] D. I. Mir, M. Grill, M. Bargende, F. Steeger, M. Günther, and S. Pischinger, "Modeling of NO and CO raw emissions based on mixture inhomogeneities in SI engines," in *22. Internationales Stuttgarter Symposium*, 2022. doi: 10.1007/978-3-658-37011-4_25.

[79] G. Fischer, *Ermittlung einer Formel zur Vorausberechnung des Reibmitteldrucks von Ottomotoren - Abschlussbericht. Reibmitteldruck*, Ottomotor FVV-Vorhaben Nr. 629. Frankfurt am Main: Forschungsvereinigung Verbrennungskraftmaschinen, 1999.

[80] M. Huß, *Übertragung von Motoreigenschaften mit Hilfe charakteristischer Skalierfunktionen zur Simulation verschiedener Varianten von Ottomotoren*. PhD thesis, Technische Universität München, 2013.

[81] G. Woschni, "A universally applicable equation for the instantaneous heat transfer coefficient in the internal combustion engine," in *SAE Technical Paper Series*, 1967. doi: 10.4271/670931.

[82] The European Parliament and the Council of the European Union, "Regulation (ec) no 715/2007 of the european parliament and of the council," *Official Journal of the European Union*, 2007.

[83] H. Tschöke, M. Arndt, M. Baade, R. Berndt, F. Bunar, B. Bunel, G. Graf, M. Grubmüller, H. Jansen, D. Köhler, E.-M. Moser, F. Schrade, K. Vidmar, L. Walter, and R. Wanker, eds., *Real Drive Emissions (RDE): Gesetzgebung, Vorgehensweise, Messtechnik, Motorische Maßnahmen, Abgasnachbehandlung, Auswirkungen*. ATZ/MTZ-Fachbuch, Wiesbaden and Heidelberg: Springer Vieweg, 2019. ISBN: 978-3-658-21078-6.

[84] G. Doornbos, I. Denbratt, and D. Dahl, "Knock phenomena under very lean conditions in gasoline powered SI-engines," *SAE International Journal of Engines*, 2018. doi: 10.4271/03-11-01-0003.

[85] M. Bassett, N. Fraser, T. Brooks, G. Taylor, J. Hall, and I. Thatcher, "A study of fuel converter requirements for an extended-range electric vehicle," *SAE International Journal of Engines*, 2010. doi: 10.4271/2010-01-0832.

[86] J. Liebl, *Der Antrieb Von Morgen 2014: Elektrifizierung: Was Erwartet der Kunde? 9. MTZ-Fachtagung*. Wiesbaden: Springer Fachmedien Wiesbaden GmbH, 2018. ISBN: 9783658237851.

[87] J. Demuynck, D. Bosteels, F. Bunar, and J. Spitta, "Diesel-PKW mit extrem niedrigem NOx-Niveau im Realfahrbetrieb," *MTZ - Motortechnische Zeitschrift*, no. 1, 2020. doi: 10.1007/s35146-019-0157-4.

[88] Motoreport.de "Fahrbericht: Golf sportsvan 2018 1.5 tsi mit 130 ps," 2017. `https://www.motoreport.de/fahrbericht-golf-sportsvan-1-5-tsi-130-ps` (accessed June 5, 2022).

[89] U. Huber, C. M. Schwarzer, "100 kilogramm kosten etwa 0,3 liter sprit." Interview. https://www.stern.de/auto/leichtbau--100-kilogramm-kosten-etwa-0-3-liter-sprit--3860240.html (accessed June 5, 2022).

[90] B. Huneke, J. Kleesattel, S. Löser, and M. Zundel, "Der neue Sechszylinder-Marinemotor von MAN für Yachten und Arbeitsboote," *MTZ - Motortechnische Zeitschrift*, vol. 77, no. 5, 2016. doi: 10.1007/s35146-016-0036-1.

[91] J. Liebl, *Ladungswechsel im Verbrennungsmotor 2016: Elektrifizierung - Potenziale für den Ladungswechsel - 9. MTZ-Fachtagung*. Wiesbaden: Springer Fachmedien Wiesbaden, 2017. doi: 10.1007/978-3-658-19198-6.

[92] MAN Truck and Bus SE, "On-road: Engines and components." https://www.engines.man.eu/man/media/content_medien/doc/global_engines/on_road/OnRoad_EN_160808_web.pdf (accessed June 5, 2022).

[93] K. Yang, M. Grill, and M. Bargende, "A simulation study of optimal integration of a rankine cycle based waste heat recovery system into the cooling system of a long-haul heavy duty truck," in *SAE Technical Paper Series*, 2018. doi: 10.4271/2018-01-1779.

[94] D. Rether, A. Schmid, M. Grill, and M. Barargende, "Quasidimensionale Simulation der Dieselverbrennung mit Vor- und Nacheinspritzungen," *MTZ - Motortechnische Zeitschrift*, vol. 71, no. 10, 2010. doi: 10.1007/BF03225618.

[95] L. Heber, J. Schwab, T. Knobelspies, M. Grill, and K. Yang, "Project report HD-TEG: Potential for improving the efficiency of heavy-duty vehicles by using a new type of waste heat recovery system." 2020. doi: 10.13140/RG.2.2.36723.66085.

[96] IVECO, "Natural Power; Geben Sie Gas mit Iveco." https://www.iveco.com/Germany/collections/catalogues/Documents/1960_IVECO_CNG-Range-Broschuere_online_Version.pdf (accessed June 5, 2022).

[97] L. Urban, M. Grill, S. Hann, and M. Bargende, "Simulation of autoignition, knock and combustion for methane-based fuels," in *SAE Technical Paper Series*, 2017. doi: 10.4271/2017-01-2186.

[98] M.-T. Keskin, M. Grill, G. Sgroi, G. Cornetti, and D. Naber, "Usercylinder: Usercylinder: Wasserstoff-Brennverfahren," 2021. https://www.fkfs.de/fileadmin/FKFS/2_Kompetenzen/2.2_Virtuelle_Entwicklung/2.2.3_Virtuelle_Motorenentwicklung/Simulation_H2_Brennverfahren.pdf (accessed June 5, 2022).

[99] R. Sierens and S. Verhelst, "Load control strategies for hydrogen fuelled IC engines," in *World Hydrogen Technologies Convention, Proceedings*. 2009.

[100] A. Boretti, "Stoichiometric h2ices with water injection," in *International Journal of Hydrogen Energy*, 2011. doi: 10.1016/j.ijhydene.2010.11.117.

[101] A. M. Nande, S. Szwaja and J. D. Naber, "Impact of EGR on combustion processes in a hydrogen fuelled SI engine," in *SAE World Congress & Exhibition*. 2008. doi: 10.4271/2008-01-1039.

[102] H. Jaaskelainen, "Heavy-duty natural gas engines," Dieselnet, 2019. https://dieselnet.com/tech/engine_natural-gas_heavy-duty.php (accessed June 5, 2022).

[103] K. K. Srinivasan, A. K. Agarwal, S. R. Krishnan, and V. Mulone, *Natural gas engines: For transportation and power generation*. Energy, environment, and sustainability, Springer, 2019. ISBN: 9789811333064.

[104] J. Czerwinski and P. Comte, "Influences of gas quality on a natural gas engine," in *SAE Technical Paper Series*, 2001. doi: 10.4271/2001-01-1194.

[105] F. Zeiten, "Neue Teststrecke nach fast 45 Jahren - Lastauto Omnibus testet im Südwesten," TEST, 2010. https://www.eurotransport.de/artikel/neue-teststrecke-lastauto-omnibus-testet-im-suedwesten-8951306.html (accessed June 5, 2022).

[106] F. Zeiten, "Typisch MAN: Man TGX 18.440 XLX," 2013. https://www.eurotransport.de/test/test-man-tgx-18440-scania-vw-d20-d26-evvicient-line-6508064.html (accessed June 5, 2022).

[107] T. Leroy, L. Nowak, L. Odillard, and D. François, "Neues Verbrennungsverfahren für mehr Effizienz von Ottomotoren," *MTZ - Motortechnische Zeitschrift*, no. 12, 2021. doi: 10.1007/s35146-021-0739-9.